

# **Optimizing electromagnetic vibration energy harvester for wireless sensor node**

**Tero Kapanen**

**School of Electrical Engineering**

Thesis submitted for examination for the degree of Master of  
Science in Technology.

Espoo 7.10.2016

**Thesis supervisor:**

D.Sc. (Tech.) Raimo Sepponen

**Thesis advisor:**

D.Sc. (Tech.) Floran Martin

Author: Tero Kapanen

Title: Optimizing electromagnetic vibration energy harvester for wireless sensor node

Date: 7.10.2016

Language: English

Number of pages: 8+102

Department of electrical engineering and automation

Professorship: Applied electronics

Supervisor: D.Sc. (Tech.) Raimo Sepponen

Advisor: D.Sc. (Tech.) Florian Martin

This Master's Thesis constructs a mathematical model for single degree of freedom spring-mass-damper vibration energy harvester which can predict the resonance frequency and the maximum output power. The main focus is on the moving magnet and coil dimension optimization for maximum output power generation to the resistive load.

Mathematical model for magnet springs were defined and validated against measurement which lead to accurate resonance frequency predictions using linearized spring constant near the magnet resting position.

Four different algorithms for magnetic flux density were bench-marked and used to calculate flux linkage to the coil. Flux linkage calculation had a good agreement with measurements.

Parameter optimization revealed that the most dominant factor affecting to the maximum output power of the harvester is the size of the moving magnet. While dimensioning and positioning of the coil is important their effects are not that significant.

Other optimization result is that the coil wire diameter does not affect to the maximum output power but it defines the output voltage and output impedance.

Two coil configuration is significantly better with small constrained construction sizes but the benefit diminishes with increasing construction size. Similarly the output power can be increased if the same magnet is used but the restriction of coil size is relaxed but the effect reduces with increased magnet size.

Keywords: Electromagnetic Vibration Energy Harvesting

Tekijä: Tero Kapanen		
Työn nimi: Sähkömagneettisen värähtelyenergiatouhimen optimointi langattomalle anturisolmulle		
Päivämäärä: 7.10.2016	Kieli: Englanti	Sivumäärä: 8+102
Elektroniikan ja automaation laitos		
Professuuri: Sovellettu elektroniikka		
Työn valvoja: TkT Raimo Sepponen		
Työn ohjaaja: TkT Floran Martin		
<p>Tämä diplomityö luo matemaattisen mallin yhden vapausasteen jousi-massa-vaimennin periaatteeseen perustuvalla värinäenergiankeräimelle. Malli ennustaa energiankeräimen resonanssitaajuuden ja lähtötehon. Pääpaino työssä on energiankeräimen lähtötehon maksimointi resistiiviseen kuormaan optimoimalla liikkuvan magneetin ja kelan mittoja.</p> <p>Työssä määritettiin matemaattinen malli magnettijouselle ja sen toiminta vahvistettiin mittauksin. Lisäksi mallista linearisoitu jousivakio magneetin lepotilan ympäristössä mahdollisti tarkan arvion energiankeräimen resonanssitaajuudesta.</p> <p>Neljää eri algoritmia magnettivuontiheyden laskentaan vertailtiin ja niitä käytettiin kelaan kytkeytyvän magnettivuon ennustamiseen. Kelaan kytkeytyvä magneettivuovo vastasi hyvin ennustettua.</p> <p>Parametrioptimointi paljasti, että liikkuvan magneetin koko vaikuttaa kaikista eniten energiankeräimen lähtötehoon ja vaikka kelan mitoitus on tärkeää sen vaikutus lopputulokseen on huomattavasti pienempi.</p> <p>Toinen optimointituloks oli, että kelassa käytetyn johtimen halkaisijalla ei ole vaikutusta lähtötehoon, mutta sitä voidaan käyttää lähtöjännitteen ja lähtöimpedanssin sovittamiseen.</p> <p>Kahden kelan kokoonpano on merkittävästi parempi kuin yhden kelan kokoonpano, kun käytettävissä oleva tilavuus on pieni, mutta tämä hyöty pienenee käytettävissä olevan koon kasvaessa. Myös kokorajoitteen poistaminen kelalta parantaa lähtötehoa ja tämän vaikutus on kaikista merkittäväintä pienillä magneeteilla.</p>		
Avainsanat: Sähkömagneettinen Energiankeräin		

## Preface

I am deeply grateful for my thesis supervisor Raimo Sepponen and my thesis advisor Floran Martin for all the support, insight and feedback I got from both of You during this project.

I am thankful for my employer who allowed flexible working hours and all the co-workers who were so understanding and expressed interest in my project. I also want to express my gratitude towards Otso Jousimaa who read my thesis and gave me much needed feedback.

Last but not least, I got enormous amount of support from my mother and father who expected me to visit them more often than what was possible, my mother-in-law who helped with childcare, my wonderful wife Paula who handled more than her fare share of our the household chores and my daughter Heidi who brightened my day when I needed it.

Klaukkala, 9.10.2016

Tero Kapanen

# Contents

<b>Abstract</b>	<b>ii</b>
<b>Abstract (in Finnish)</b>	<b>iii</b>
<b>Preface</b>	<b>iv</b>
<b>Contents</b>	<b>v</b>
<b>Symbols and abbreviations</b>	<b>vii</b>
<b>1 Introduction</b>	<b>1</b>
<b>2 Background</b>	<b>3</b>
2.1 Growing interest in energy harvesting . . . . .	3
2.2 Energy harvesting technologies . . . . .	4
2.3 Applications . . . . .	6
2.4 Frequency and amplitude of available ambient vibration . . . . .	8
<b>3 Electromechanical Analysis</b>	<b>11</b>
3.1 Mechanical model . . . . .	11
3.1.1 Single Degree of Freedom spring-mass-damper . . . . .	11
3.1.2 Viscous Damping . . . . .	15
3.1.3 Magnetic spring . . . . .	16
3.2 Power calculation . . . . .	20
3.2.1 Constraints and geometry parameters . . . . .	21
3.2.2 Coil . . . . .	22
3.2.3 Magnetic flux density . . . . .	25
3.2.4 Magnetic flux linkage . . . . .	31
3.2.5 Transconductance factor . . . . .	32
3.2.6 Electrical Domain Analog Matching . . . . .	33
3.2.7 Output voltage and power . . . . .	35
<b>4 Model validation</b>	<b>36</b>
4.1 Design of the Prototypes . . . . .	36
4.2 Viscous damping measurements . . . . .	38
4.3 Restoration force calculation validation . . . . .	42
4.4 Coil resistance validation . . . . .	46
4.5 Flux linkage computational model validation . . . . .	46
4.6 Power calculation validation . . . . .	53
4.7 Testing prototypes with a shaker . . . . .	55
<b>5 Parameter optimization</b>	<b>62</b>
5.1 Constrained construction volume and fixed aspect ratio . . . . .	62
5.2 Effects of fill factor to parameter optimization . . . . .	67
5.3 Effects of wire diameter to parameter optimization . . . . .	68

5.4	Construction volume size . . . . .	71
5.5	Shape of the construction volume . . . . .	74
5.6	Residual flux density of the permanent magnet . . . . .	78
5.7	Fixed magnet . . . . .	79
<b>6</b>	<b>Conclusions</b>	<b>83</b>
<b>A</b>	<b>Repulsion force calculation</b>	<b>89</b>
<b>B</b>	<b>Magnetic flux linkage calculation</b>	<b>90</b>

# Symbols and abbreviations

## Symbols

$h$	maximum construction height
$r_{\text{mag}}$	magnet radius
$h_{\text{mag}}$	magnet height
$h_{\text{coil}}$	coil height
$r_{\text{i}}$	coil inner radius
$r_{\text{o}}$	coil outer radius
$G_{\text{w}}$	gap between the magnet and the wall
$G_{\text{c}}$	gap between the magnet and the coil
$k_{\text{co}}$	copper fill factor
$d_{\text{co}}$	wire diameter
$F_{\text{k}}$	spring force
$k$	spring constant
$F_{\text{d}}$	viscous damping force
$d$	damping coefficient $d = d_{\text{e}} + d_{\text{m}}$
$d_{\text{e}}$	electrical damping coefficient
$d_{\text{m}}$	mechanmical damping coefficient
$x, y, z$	displacements
$\dot{x}, \dot{y}, \dot{z}$	velocities
$\ddot{x}, \ddot{y}, \ddot{z}$	accelerations
$Y, \ddot{Y}$	amplitude and acceleration of base excitation
$\omega_n$	natural frequency
$d_{\text{cr}}$	critical damping
$\zeta$	damping ratio
$N, N_{\text{r}}, N_{\text{z}}$	number of turns, turn in radial and axial directions
$\mathbf{B}$	magnetic flux density
$B_{\text{z}}$	axial component of magnetic flux density
$B_{\text{r}}$	residual flux density
$\mu_0$	permeability of free space
$M$	magnetization
$d_{\text{sep}}$	separation between two magnets
$h_{\text{mm}}$	distance from magnet 2 to magnet 3
$\varphi_{\text{m}}$	magnetic flux linkage
$k_{\text{t}}$	transconductance factor
$emf$	electromotive force
$V_{\text{max}}$	maximum construction volume
$R_{\text{coil}}$	coil resistance
$t_0$	magnet resting position
$R_{\text{ratio}}$	ratio between $r_{\text{o}}$ and $r_{\text{i}}$
$H_{\text{ratio}}$	ratio between $h_{\text{coil}}$ and $h$
$T_{\text{ratio}}$	ratio between $h_{\text{coil}}$ and $t_0$
$HR$	aspect ratio, ratio between $h$ and $r_{\text{o}}$

## Abbreviations

CPU	Central Processing Unit, processor
EH	Energy Harvester
RoHS	The Restriction of the use of certain Hazardous Substances in Electrical and Electronic Equipment
SDOF	Single Degree of Freedom
WEEE	directive on waste electrical and electronic equipment
WSN	Wireless Sensor Node



# 1 Introduction

Energy harvesters (EH) convert energy from ambient energy sources to electricity. These devices enable measuring and monitoring physical quantities, such as temperature or acceleration, that were previously unavailable for applications which could not employ batteries or wires. These measurements provide a feedback loop to the process and allow replacing manual or open loop controls with automated closed loop controls. Usually only the locomotive is powered by electricity and freight cars are unpowered hence the freight cars cannot provide power to any electronics. One monitoring application in freight train would be wheel/axle condition monitoring where a wireless sensor node (WSN) measures the temperature and vibration of the axle and transmits the results to the locomotive. While it is possible to power the WSN using batteries the batteries suffer from limited lifetime which could increase the maintenance cost. Also railway standard EN 50155 [1] defines useful life of the electronic equipment as 20 years if not agreed otherwise and that it is not allowed to use any component whose known useful life is less than that without agreement with the user at the time of tendering.

There are many reasons to eliminate batteries from electronic devices. Firstly, batteries have a very limited life span. This means that the user has recurring expenses from procurement, installation and disposal of batteries. Secondly, the depleted batteries are hazardous materials that contain heavy metals and toxic chemicals that are carcinogenic and can cause soil contamination and water pollution if not recycled properly. Furthermore, some battery technologies have a risk of catching fire or exploding in certain conditions. Wires also have their problems. The wires themselves are expensive and it is costly to install them especially if the amount of sensors is large or in a retrofit project. Sometimes there are no permanent energy sources available for wiring or it is not permitted to drill holes into structures for cables. In other cases the sensor needs to be far away or in a moving vehicle.

Usually there are ambient vibrations present in moving vehicles and therefore using it as an energy source is one appropriate method of generating energy in a moving train. If viewing vibration energy generator technologies as a whole the biggest vibration energy generators that convert sea waves to electricity can have a maximum continuous electric output power of 10 MW and on the other end of the spectrum are wafer level vibration energy harvesters able to produce mere 1  $\mu$ W. Large-scale generators are usually called renewable energy generators while small-scale generators are called energy harvesters. This can be seen as a continuum which does not have clearly defined boundaries. Usually energy harvesters refer to devices that generate less than 1 W of output power. The size of the harvester determines the amount of output power available and since the size is restricted to what can be installed between the bogie and the coach the expected output power from a practical railway WSN would be from 1 mW to 10 mW. This amount of power exceeds the amount of power needed for basic operations of the WSNs and the spare energy can be stored to energy storage that can provide power while there are no vibrations available like in case of stopping at a station. Similar applications could use solar power or harvesters using temperature difference to generate electricity but this

thesis concentrates to only vibration energy harvesters.

Purpose of the thesis is to construct a mathematical single degree of freedom spring-mass-damper vibration energy harvester model that predicts the resonance frequency and output power of the vibration energy harvester. In addition to the analytical modeling, the model needs to be validated. Further purpose of the thesis is to find optimal design parameters for the energy harvester given the installation location specifications and requirements for the harvester. Outcomes of this thesis constitute a framework to design the electromechanical structure of the vibration energy harvester in real life application and reduce the number of prototypes needed to implement commercial product. The simulation and optimization method can be extended to include different types of the harvester configurations in the future.

This thesis is divided into five chapters. This chapter gives introduction to the thesis. Chapter 2 details the previous research on energy harvesting and vibration energy harvesting elaborating this introduction and presenting the current state-of-the-art. Chapter 3 formulates the computational model for the vibration energy harvester which allows analyzing and optimizing design to the type of vibration present in the installation location of the harvester. Chapter 4 describes the experimentation setup and results of the experimentation that were done to validate the model. Chapter 5 presents the different optimization approaches and the optimization results. Finally, Chapter 6 summarizes the outcomes of this thesis, discusses issues that rose during the model development, and experimentation and proposes future research areas. The Python scripts created for this thesis can be found from GitHub [2].

## 2 Background

Energy harvesters (EH) are devices that convert energy from ambient energy sources to electricity. The main difference to large scale renewable energy generators is that while they can produce megawatts of power, harvesters usually produce in microwatt or milliwatt range. Energy harvesting technologies have become increasingly important building blocks for wireless sensor nodes (WSN) which form wireless sensor networks. These WSNs usually consist of sensors, microprocessor, wireless radio and power source. Previously these WSNs were powered from batteries but the limited lifespan and environmental impact have increased the interest in energy harvesting technologies. [3].

This chapter presents ambient energy sources, principles of energy harvesting, reviews previous studies on vibration energy harvesting. Section 2.1 explains the growing interest in energy harvesters and what benefits they introduce. Section 2.2 describes different technologies, their operating principles and how they compare to each other. Section 2.3 provides examples of applications where energy harvesting technologies could be used and finally Section 2.4 describes expected available vibration.

### 2.1 Growing interest in energy harvesting

In recent years, much research has been devoted to energy harvesting. Searching research articles from one of the largest abstract and citation databases [4] of peer-reviewed literature with the term “energy harvesting” resulted in 13 387 documents. The results of the search are shown as a function of publishing year in Figure 1. It can be seen that there were relatively few publications around 2000 and that the number of publications has increased significantly during the last ten years, reaching a level of almost 3 000 publications a year in 2014.

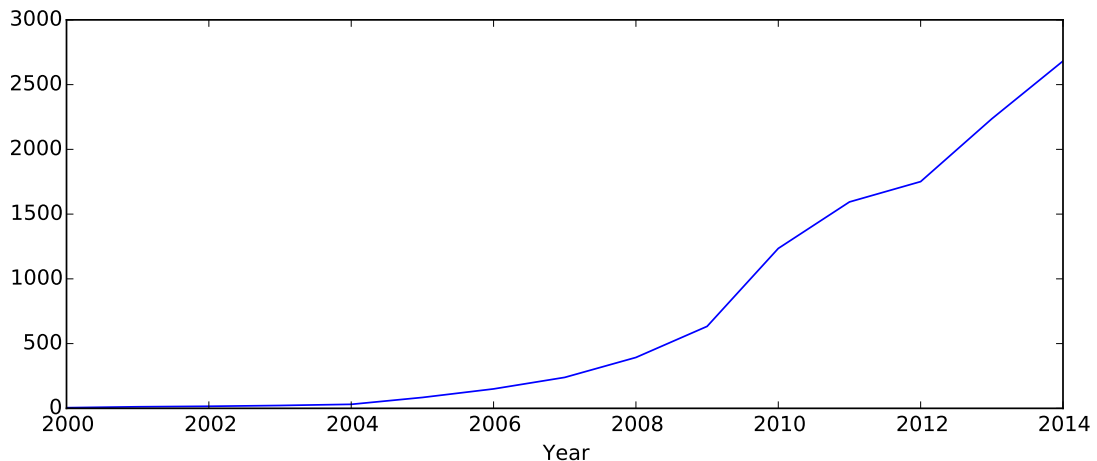


Figure 1: Published peer-reviewed literature as a function of time.

Commercial potential for energy harvesting technologies have been prime reason

for growing interest in energy harvesting. One of the world's leading information technology research and advisory companies, Gartner, forecasted at Gartner Symposium/ITxpro 2015 that there will be 6.4 billion connected "Things" in use 2016 and that this will grow to more than 20 billion in 2020 [5].

## 2.2 Energy harvesting technologies

WSNs, wearables and also many Internet-of-Things (IoT) devices are off the power grid and thus they need to be powered locally. These devices can be powered by primary batteries, which means that they are designed for since discharge cycle, or by rechargeable secondary batteries [6, p. 686].

There are different ambient energy sources available depending on the installation location and the type of the application and the size restrictions. The size or the maximum output power is sometimes used for classifications. Beeby et. al [7] defines large-scale vibration energy harvesters as those which produces more than 1 W or more output power, all the way up to megawatts.

Commercially available solar cells have typical efficiency of 14–19% and the available input power is from less than  $10 \text{ W/m}^2$  in dimly lit warehouses to over  $1000 \text{ W/m}^2$  in direct sunlight. Temperature gradients can also be used as a source and they produce  $15 \mu\text{W/cm}^3$  at  $10^\circ\text{C}$  temperature difference. Vibration energy harvesters are divided in three main category; piezoelectric, electrostatic and electromagnetic harvesters. The biggest vibration energy harvesters that convert sea waves to electricity can have maximum continuous electric output power of 10 MW and on the other end of the spectrum are wafer level vibration energy harvesters able to produce mere  $1 \mu\text{W}$ . This thesis will concentrate on space restricted macro scale electromagnetic harvesters that can provide sufficient power (1 mW to 10 mW) to WSNs. These electromagnetic harvesters have several different configurations and the focus is on those which have magnet as a proof mass that moves through a coil. Table 4 shows power densities of different energy harvesting technologies While Table 2 summarizes the differences between three main vibration energy harvesting technologies.

The theoretical maximum efficiency for linear (not rotational) electromagnetic energy harvester is less than 50 % and the maximum output power cannot be achieved simultaneously with the maximum efficiency [8]. The efficiency can be even lower in real applications because the power in ( $P_{\text{in}} = F \cdot v = m \cdot a \cdot v$ ) to the system is dependent on the mass of the complete harvester instead of the mass of the moving magnet. This does not pose serious problem in the applications where the vibrating body is several orders of magnitude greater than the size or mass of the energy harvester. Mitcheson have compared [9] reported of published electromagnetic harvesters and the best have efficiency of 6.92 % while most research articles does not report any efficiency figures.

Table 1: Power densities of different energy harvesting technologies.

Technology	Power density
Indoor light (500 lux) [10]	$300 \mu\text{W}/\text{cm}^2$
Indoor light, direct sun [11]	$10 \mu\text{W}/\text{cm}^2$
Outdoor light [10]	$100 \text{mW}/\text{cm}^2$
Outdoor light, direct sun [11]	$15 \text{mW}/\text{cm}^2$
Outdoor light, cloudy day [11]	$150 \mu\text{W}/\text{cm}^2$
Acoustic noise [11]	$0.96 \mu\text{W}/\text{cm}^2$ 100 Db
Temperature gradient, $\Delta T = 10^\circ\text{C}$ [11]	$15 \mu\text{W}/\text{cm}^2$
Vibration energy, Piezoelectric [9]	$2.47 \mu\text{W}/\text{cm}^3 - 15 \text{mW}/\text{cm}^3$
Vibration energy, Electromagnetic [12]	$10 \mu\text{W}/\text{cm}^3 - 260 \text{mW}/\text{cm}^3$
Vibration energy, Electrostatic [9]	$2.42 \mu\text{W}/\text{cm}^3 - 56 \mu\text{W}/\text{cm}^3$

Table 2: Summary of different vibration harvesting technologies [13]

Property	Piezoelectric	Electromagnetic	Electrostatic
Output impedance	high, capacitive	low, resistive	very high
Output voltage	high	low	very high
Maturity	commercial	commercial	research projects
Other	simplest		need initial charge

## 2.3 Applications

Wireless sensor nodes (WSN) are becoming to replace wired sensor nodes since they eliminate the need to install cables which could be both cumbersome and expensive especially in retrofit projects. The biggest obstacle for the adoption of WSNs have been the high power consumption of the radio link but the power consumption of the radio chips continually decreases and currently some WSNs can operate several years with a coin cell battery. However, some applications require more than several years of run time or they require high sample rate and therefore need to communicate the measurement result often over the radio and thus deplete the battery much sooner. Large installations with thousands of nodes could require dedicated maintenance staff who changes batteries as their full time job. Some nodes may be installed in locations where the battery replacement is either extremely difficult or dangerous and thus inconceivable.

Figure 2 present the block diagram of a typical WSN. It can be divided into two parts one that generates, stores and regulates electricity and the other part that consumes it. Energy generator part contains the actual energy harvester that converts the available ambient power to electricity. If this electricity is AC like in the case of electromagnetic energy harvesters it needs to be rectified to get DC voltage. This rectification could reduce the efficiency of the energy harvesting system significantly if the output voltage from the harvester is low. This problem can be mitigated by using rectifying diodes with lower forward threshold voltage, using different rectifier-multipliers configurations [14] or using the coil inductance as a part of switching regulator [15], [16].

Since the vibration can stop for a extended periods of time there needs to be a storage element that stores excess energy in normal operation in order to supply it when there is no energy to be harvested. Other function of the storage element is that it can supply the temporary high current needed for the radio during communication while the average current consumption may be moderate. Usually the level of electricity in the storage element is not at the right level for the processor, sensors and radio and it therefore have to be regulated to the appropriate level. The part that consumes the energy poses requirements to the part that generates electricity. One example power consumption case is presented in Table 3.

Texas Instruments have CC3100 WiFi Internet-on-a-chip that is very low power WiFi radio [17]. While the input current during transmission is as high as 250 mA and receive current 53 mA, if the module is active shortly only once in every two minutes the average current consumption would be 111  $\mu$ A. This would mean average input power of 0.366 mW at 3 V input voltage. If the energy harvester could produce at least 1 mW output power on average then there would be enough surplus energy to be stored to the capacitor between the active periods but if the frequency of the vibration changes significantly from the resonance frequency of the harvester it would be better to select 10 mW as a target figure for optimization. Since the module consumes only 4  $\mu$ A at hibernate state the average current consumption is determined by the activity period. Table 3 describes the energy consumption of the CC3100 during 2 minute activity period. If this is to be powered by two alkaline AA

batteries the batteries would last only 681 days which is less than two years [17].

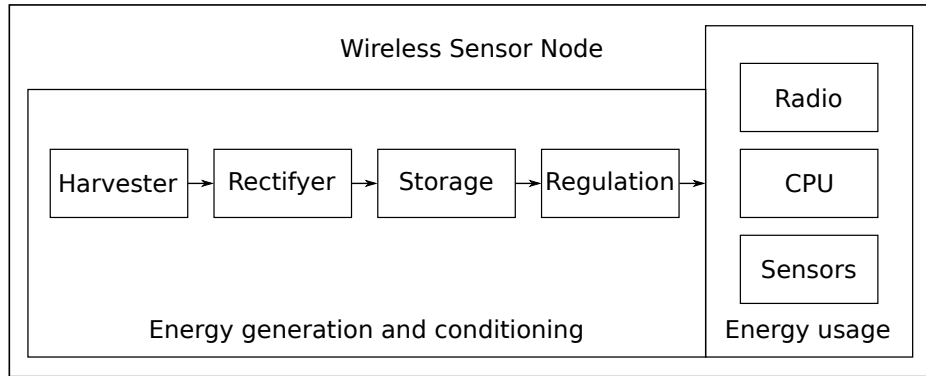


Figure 2: Wireless Sensor Node block diagram.

Table 3: CC3100 energy consumption for 2 minute activity period [17]

Description	Energy
Energy spent during system initialization	5.6 mJ
Energy spent during re-connecting to the AP	6.6 mJ
Energy spent while re-connecting to the server	13.2 mJ
Energy spent during application traffic	16.5 mJ
Energy spent in hibernate mode	2 mJ
Total	44 mJ

## 2.4 Frequency and amplitude of available ambient vibration

Since most vibration energy harvesters are resonators they work with high efficiency only at the resonance frequency or very near it. Therefore it is indispensable to know the spectral density of the available vibration in the specific application.

Human perception of the vibration have following statistical threshold levels. the level of perception is 0.001 g to 0.01 g, the vibration is considered unpleasant when the level of vibration is 0.1 g and intolerable at the level of 0.5 g by most people. It is also noted that the vibration problems and the humans sensitivity is highly correlated when the amount of background vibration is low. Wowk even proposes that “if vibration is uncomfortable to people, then it is probably causing serious damage to the machine” [18, p. 62].

DLI engineering developed machinery vibration severity chart in 1988 which classifies vibration severity based on its frequency, amplitude and velocity [19]. This chart re-produced in Figure 3. This chart is called nomogram because it shows how frequency, amplitude, velocity and acceleration depends on each other in harmonic oscillation.

IEC 61373 [20] is a international standard for shock and vibration tests for rolling stock equipment and it defines its test limits using the data gathered from data acquired from train operators. Figure 4 describes the three standard measuring positions (Axle, Bogie and Body) as well as the three directions of vibration (Longitudinal, Transverse and Vertical).

The summary of data acquired by the IEC 61373 standard working group is shown in Table 4. This data suggest that the dominant direction of the vibration is vertical in all three standard measurement positions. Moreover, the vibration at the axle is higher than in bogie because the axle is directly coupled to the rail and the vibrations are dampened even more at the body because of the second set of springs and dampers. Most suitable position for vertical vibration energy harvesting is axle where the average amplitude of the acceleration is 3.46 g and the second most suitable is bogie where it is 0.45 g. Average amplitude is get from the average r.m.s. value by multiplying it by  $\sqrt{2}$  and dividing by  $9.81 \text{ m/s}^2$ .

IEC 61373 standard does not define at which frequencies the acquired acceleration values were measured but it defines the bandwidth over which all equipment is to be tested. This bandwidth depends on the mass of the tested device as well as the mounting position but if the mass of the tested equipment is ignored then the bandwidth for body mounted equipment is from 2 Hz to 150 Hz, for bogie mounted equipment from 2 Hz to 250 Hz and for axle mounted equipment from 10 Hz to 500 Hz



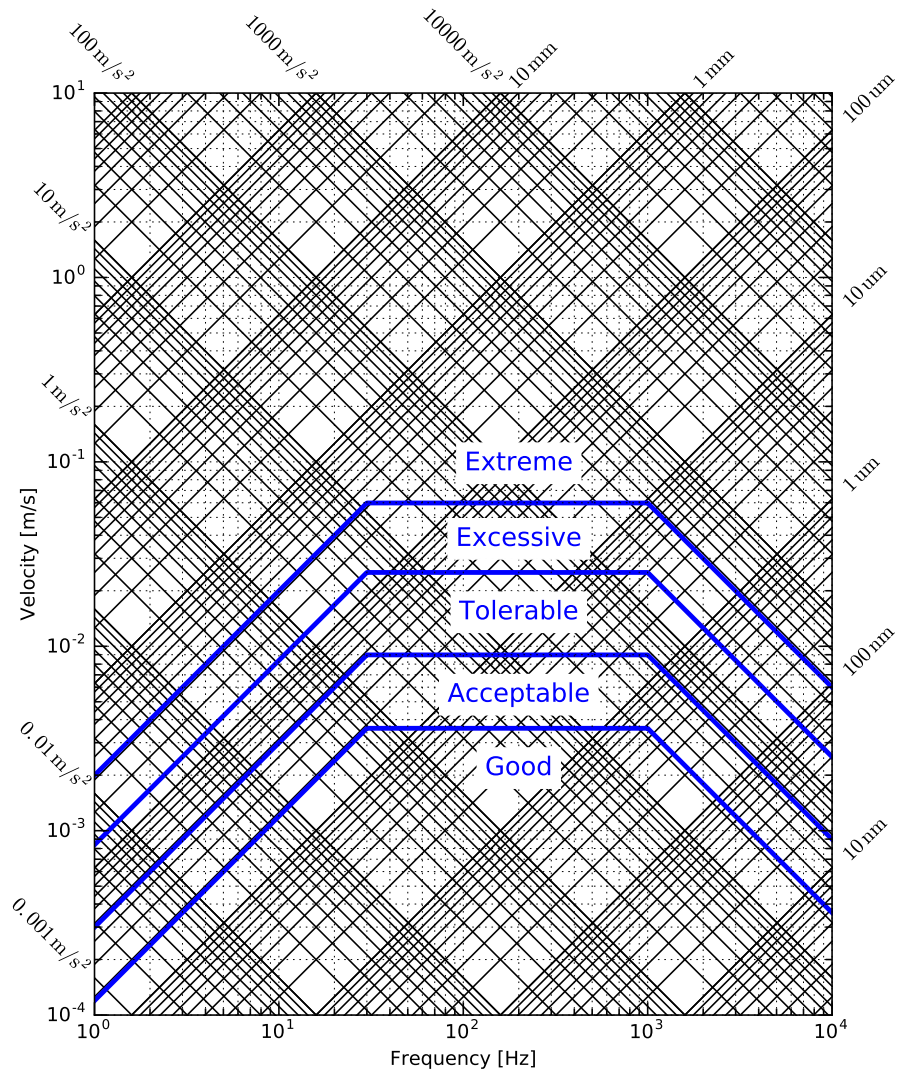


Figure 3: Vibration nomogram with severity levels for large high speed machinery

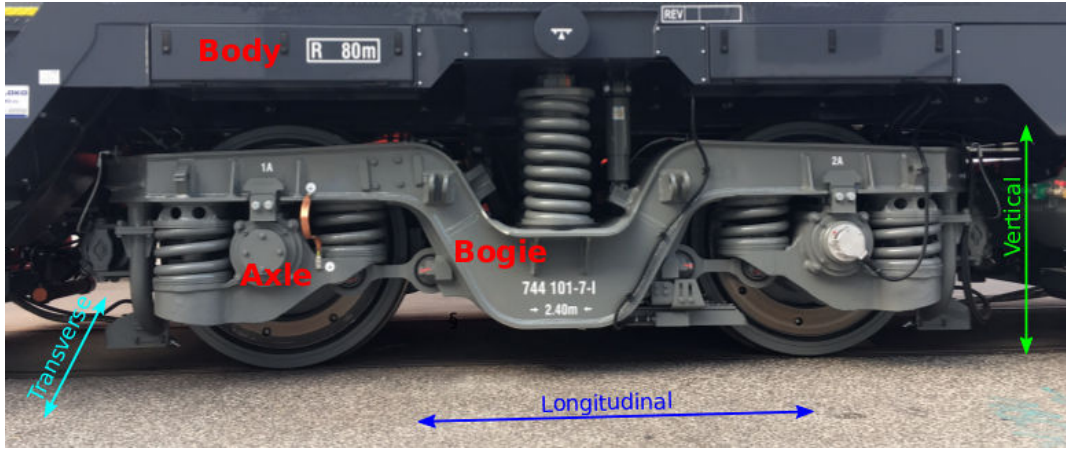


Figure 4: Axle, bogie and body mounted categories measuring positions

Table 4: IEC 61373 vibration levels acquired from rail operators [20].

Direction	Category	max. level $\text{m/s}^2$ r.m.s.	avg. level $\text{m/s}^2$ r.m.s.	avg. level g	std. dev. $\text{m/s}^2$
Vertical	Body	1.24	0.49	0.07	0.26
Vertical	Bogie	7.0	3.1	0.45	2.3
Vertical	Axle	43	24	3.46	14
Transverse	Body	0.43	0.29	0.04	0.08
Transverse	Bogie	7.0	3.0	0.43	1.7
Transverse	Axle	39	20	2.88	14
Longitudinal	Body	0.82	0.30	0.04	0.20
Longitudinal	Bogie	4.1	1.2	0.17	1.3
Longitudinal	Axle	20	11	1.59	6

### 3 Electromechanical Analysis

The previous chapter introduced various energy harvesting technologies in general and specifically outlined previous studies on vibration energy harvesters. This chapter formulates semi-analytical model for the selected type of vibration energy harvester. This computational model allows harvester optimization to ambient vibration present in the installation location. Section 3.1 defines the mechanical model of the spring-mass-damper system, the type of ambient frequencies available for the harvester, theoretical estimation of viscous damping and magnetic spring. The purpose of this section is to give basic understanding of the mechanical system and assist tuning energy harvester resonance frequency to the dominant ambient frequency. Section 3.2 creates computational model to calculate magnetic flux density caused by the permanent magnet, the magnetic flux linkage to the coil and eventually the output voltage and power to the load. Even though nonlinear magnetic spring is used to tune the resonance frequency, linear spring is assumed in the power calculation since the additional accuracy of the model does not warrant the increased complexity of nonlinear analysis.

#### 3.1 Mechanical model

This section is divided in three subsections. Section 3.1.1 defines the single degree of freedom spring-mass-damper systems. Section 3.1.2 defines the theoretical model for viscous damping. Section 3.1.3 defines the model for magnetic spring.

##### 3.1.1 Single Degree of Freedom spring-mass-damper

Most vibration energy harvesters are inertial spring-mass systems. These harvesters are resonators which produce maximum power at their resonance frequency and very little elsewhere. Therefore it is essential to match the resonance frequency to the frequency of the dominant vibration in the environment. [3]

Most simple mechanical model for vibration energy harvester is a Single degree of freedom (SDOF) spring-mass-damper system. These are systems where movement occurs along single axis and the system consists of moving mass which is suspended with a linear mass-less spring having stiffness  $k$  and viscous damper with a damping coefficient  $d$  [21]. If the force is applied to the proof mass  $m$  directly the the system is called direct excitation SDOF spring-mass-damper system. Such a system is illustrated in Figure 5.

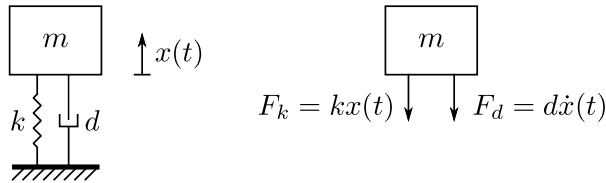


Figure 5: Direct excitation SDOF spring-mass-damper system.

Direct excitation systems are useful to analyze because they are simpler and they reveal the natural frequency  $\omega_n$  of the system. Spring force applied to the mass is

$$F_k = kx(t) \quad (1)$$

and consequently the total force applied to the mass in undamped system where  $d = 0$  is

$$F = F_g - F_k = mg - kx \quad (2)$$

Newton's second law states that the vector sum of the external forces is the product of the mass and acceleration, where acceleration is the second derivative of displacement  $x$ . Assuming the displacement relatively small the spring can be assumed linear and thus the gravitation force only alters the initial position of the mass and the gravitational term can be eliminated [21]

$$\begin{aligned} F &= ma = m\ddot{x}(t) = -kx(t) \\ m\ddot{x}(t) + kx(t) &= 0 \end{aligned} \quad (3)$$

where  $\ddot{x}$  is second time derivative of displacement  $x$ . This second order linear differential equation can be solved by knowing the form of the solution [21]

$$x(t) = A \sin(\omega_n t + \phi), \quad (4)$$

where  $\omega_n$  is the angular natural frequency and  $\phi$  is phase. Since velocity is the first time derivative of the displacement

$$\dot{x}(t) = \omega_n A \cos(\omega_n t + \phi) \quad (5)$$

and acceleration can be written

$$\ddot{x}(t) = -\omega_n^2 A \sin(\omega_n t + \phi) \quad (6)$$

Substituting (4) and (6) to (3)

$$\begin{aligned} -m\omega_n^2 A \sin(\omega_n t + \phi) &= -kA \sin(\omega_n t + \phi) \\ \omega_n^2 &= \frac{k}{m} \implies \omega_n = \sqrt{\frac{k}{m}} \end{aligned} \quad (7)$$

Only ideal system can oscillate indefinitely and practical systems have damping which causes oscillations to diminish and eventually to stop altogether. Usually the damping is introduced to the equation by adding term  $d\dot{x}(t)$ , where  $d$  is a damping coefficient and the  $\dot{x}$  is the velocity. This kind of damping is called viscous damping and the damping force is

$$F_d = d\dot{x}(t) \quad (8)$$

The equation of motion for unforced oscillation becomes

$$m\ddot{x}(t) + d\dot{x}(t) + kx(t) = 0 \quad (9)$$

Damped equation can be solved letting  $x(t)$  to have a form  $x(t) = ae^{\lambda t}$  which yields

$$\begin{aligned} (m\lambda^2 + d\lambda + k)ae^{\lambda t} &= 0 \\ m\lambda^2 + d\lambda + k &= 0 \end{aligned} \quad (10)$$

which have the following solutions

$$\lambda_{1,2} = -\frac{d}{2m} \pm \frac{1}{2m}\sqrt{d^2 - 4km} \quad (11)$$

Damping is said to be critical when the discriminant is zero hence critical damping coefficient is

$$d_{cr} = 2m\omega_n = 2\sqrt{km} \quad (12)$$

and the damping ratio is

$$\zeta = \frac{d}{d_{cr}} = \frac{d}{2m\omega_n} = \frac{d}{2\sqrt{km}} \quad (13)$$

The damping ration is  $0 < \zeta < 1$  for underdamped systems.

If the force is applied to base of the system instead of the proof mass  $m$  then the system is called a base excitation SDOF spring-mass-damper system [21]. Such a system is illustrated in Figure 6.

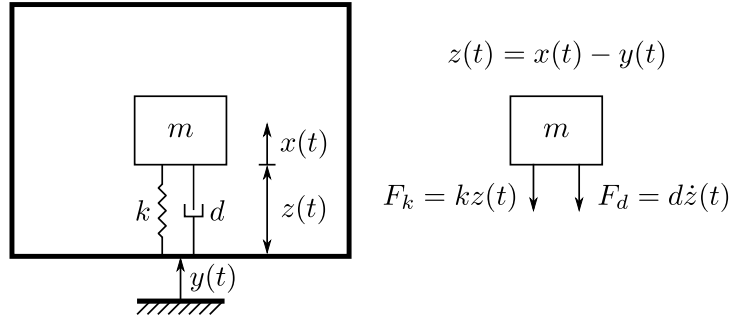


Figure 6: Base excitation SDOF spring-mass-damper system.

The sum of all forces becomes

$$m\ddot{x} + d(\dot{x} - \dot{y}) + k(x - y) = 0 \quad (14)$$

$$m\ddot{x} + d\dot{z} + kz = 0 \quad (15)$$

Since the base is excited harmonically the amplitude of the excitation is

$$y(t) = Y \sin \omega_b t \quad (16)$$

where  $Y$  is the amplitude of the excitation and  $\omega_b$  is the frequency of base excitation. Harmonic excitation of the base damped system becomes

$$m\ddot{x} + d\dot{x} + kx = dY\omega_b \cos \omega_b t + kY \sin \omega_b t \quad (17)$$

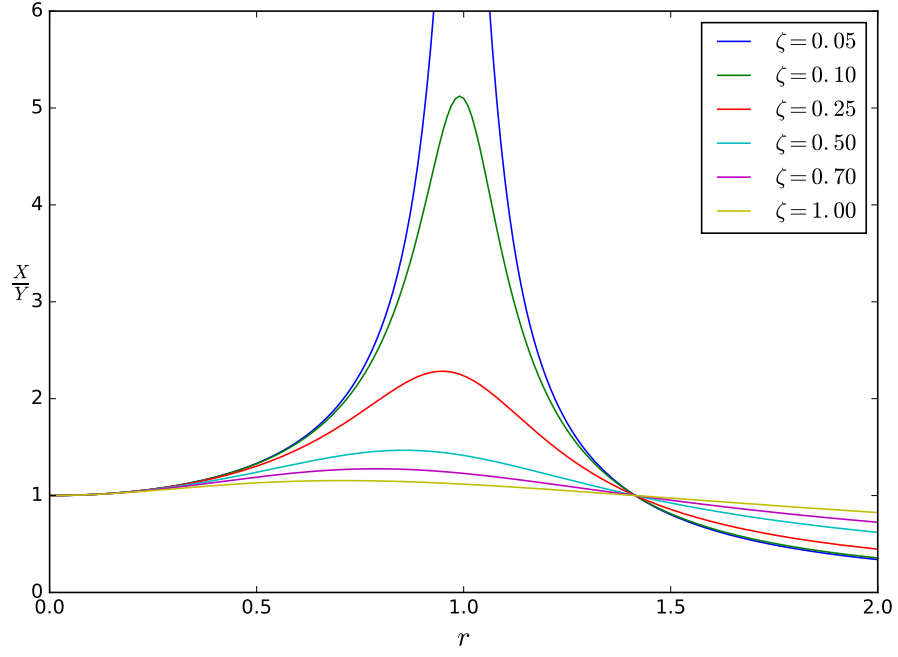


Figure 7: Displacement transmissibility in base excited system.

which can be expressed using natural frequencies and damping ratios [21]

$$\ddot{x} + 2\zeta\omega_n\dot{x} + \omega_n^2x = 2\zeta\omega_n\omega_bY \cos \omega_bt + \omega_n^2Y \sin \omega_bt \quad (18)$$

The amplitude of the moving mass can be solved [21]

$$X = Y \sqrt{\frac{1 + (2\zeta r)^2}{(1 - r^2)^2 + (2\zeta r)^2}} \quad (19)$$

where  $\theta$  is the damping ratio and  $r = \omega_b/\omega_n$  is the frequency ratio. Displacement transmissibility in base excited system is illustrated in Figure 7.

### 3.1.2 Viscous Damping

SDOF spring-mass model does not represent accurately the real world without damping since without it the system would oscillate indefinitely. The choice of model depends on the physical observations and the mathematical convenience. Viscous damping is a type of damping where the damping force,  $F_d = d\dot{x}(t)$ , is directly proportional to the velocity and where the damping coefficient  $d$  is constant. [21, pp. 19–20]

Moving magnet inside the tube can be modelled as a viscous damper using the formula which is derived for piston moving in a cylinder [22]

$$d_m = \frac{6\pi\mu h_{\text{mag}}}{G_w^3} \left( \left( r_{\text{mag}} - \frac{G_w}{2} \right)^2 - r_{\text{rod}}^2 \right) \left( \frac{r_{\text{mag}}^2 - r_{\text{rod}}^2}{r_{\text{mag}} - \frac{G_w}{2}} - G_w \right), \quad (20)$$

where  $G_w$  is the air gap between the magnet and the tube wall (it shall not be confused with  $G_c$  which is the gap between the magnet and the coil),  $\mu$  is the dynamic viscosity of the air,  $h_{\text{mag}}$  is the height of the magnet and  $r_{\text{mag}}$  is the radius of the moving magnet. Now when there is no rod in the harvester design, i.e.  $r_{\text{rod}} = 0$ , the formula simplifies to

$$d_m = \frac{6\pi\mu h_{\text{mag}}}{G_w^3} \left( r_{\text{mag}} - \frac{G_w}{2} \right)^2 \left( \frac{r_{\text{mag}}^2}{r_{\text{mag}} - \frac{G_w}{2}} - G_w \right), \quad (21)$$

The limit value of the damping as air gap approaches zero is calculated below

$$\lim_{G_w \rightarrow 0} d_m = \lim_{G_w \rightarrow 0} \frac{6\pi\mu r_{\text{mag}}^3 h_{\text{mag}}}{G_w^3} = +\infty \quad (22)$$

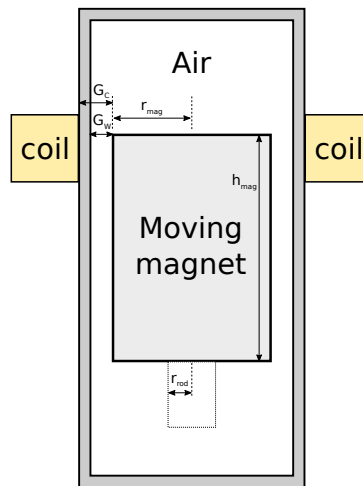


Figure 8: Dimensions used in viscous damping

### 3.1.3 Magnetic spring

Energy harvester is composed of three magnets put inside a tube with same poles opposing each other. The bottom and top magnets, which are identical, are fixed to the end of the tube so that they cannot move while the magnet in the middle can move freely. For the sake of convenience the magnets are numbered so that the moving magnet is called magnet 1, bottom magnet is called magnet 2 and top magnet is called magnet 3. This construction is illustrated in the figure 9.

SDOF spring-mass-damper systems by definition contains a spring. The problem is that aforementioned construction does not have any conventional spring. Repulsion force of two permanent magnets depends on the shape of the magnets, the magnetization of the magnets and the relative position to each other [23]. Therefore the magnetic manufacturer cannot give unambiguous spring constant for magnets but it have to be calculated from the above mentioned parameters.

Furlani [23, p. 131] describes the Charge Model in which the problem is simplified by introducing a concept of “magnetic charge”. In this model, the magnetic charge distributions defines the permanent magnet and they can be used as a source term in magnetostatic field equations. The volume and surface charge densities are defined as

$$\begin{aligned}\rho_m &= -\nabla \cdot \mathbf{M} \quad (\text{A/m}^2) && \text{(volume charge density)} \\ \sigma_m &= \mathbf{M} \cdot \hat{\mathbf{n}} \quad (\text{A/m}) && \text{(surface charge density)}\end{aligned}\quad (23)$$

Where  $\mathbf{M}$  is the remanent magnetization of the permanent magnet and  $\hat{\mathbf{n}}$  is a unit vector perpendicular to the surface on which the equivalent magnetic charge is distributed. The magnetic flux produced by a permanent magnet in a free space ( $\mathbf{B} = \mu_0 \mathbf{H}$ ) is according to [23, p. 132]

$$\mathbf{B}(\mathbf{x}) = \frac{\mu_0}{4\pi} \int_V \frac{\rho_m(\mathbf{x}')(\mathbf{x} - \mathbf{x}')}{|\mathbf{x} - \mathbf{x}'|^3} dv' + \frac{\mu_0}{4\pi} \oint_S \frac{\sigma_m(\mathbf{x}')(\mathbf{x} - \mathbf{x}')}{|\mathbf{x} - \mathbf{x}'|^3} ds' \quad (24)$$

The Charge Model can be used to derive equation for a force exerted to a magnet

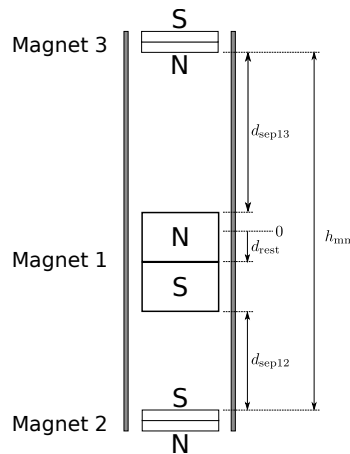


Figure 9: Harvester magnet construction.



by external field  $\mathbf{B}_{\text{ext}}$ . This equation is derived in [23, pp. 135–136].

$$\mathbf{F} = \int_V \rho_m \mathbf{B}_{\text{ext}} dv + \oint_S \sigma_m \mathbf{B}_{\text{ext}} ds \quad (25)$$

Force between two permanent magnet is get when equation (24) is substituted to equation (25). This is difficult to solve analytically but it is possible to solve it numerically. This can be done by discretizing the volume  $V$  and surface  $S$  of the magnet. The force between two permanent magnets can be written [23, p. 138]

$$\begin{aligned} \mathbf{F} = & \frac{\mu_0}{4\pi} \sum_n \left\{ \sum_j \left[ \frac{\rho_m(\mathbf{x}_n) \rho_m(\mathbf{x}_j) (\mathbf{x}_n - \mathbf{x}_j)}{|\mathbf{x}_n - \mathbf{x}_j|^3} \right] \Delta V_j \right\} \Delta V_n \\ & + \frac{\mu_0}{4\pi} \sum_n \left\{ \sum_k \left[ \frac{\rho_m(\mathbf{x}_n) \sigma_m(\mathbf{x}_k) (\mathbf{x}_n - \mathbf{x}_k)}{|\mathbf{x}_n - \mathbf{x}_k|^3} \right] \Delta A_k \right\} \Delta V_n \\ & + \frac{\mu_0}{4\pi} \sum_p \left\{ \sum_j \left[ \frac{\sigma_m(\mathbf{x}_p) \rho_m(\mathbf{x}_j) (\mathbf{x}_p - \mathbf{x}_j)}{|\mathbf{x}_p - \mathbf{x}_j|^3} \right] \Delta V_j \right\} \Delta A_p \\ & + \frac{\mu_0}{4\pi} \sum_p \left\{ \sum_k \left[ \frac{\sigma_m(\mathbf{x}_p) \sigma_m(\mathbf{x}_k) (\mathbf{x}_p - \mathbf{x}_k)}{|\mathbf{x}_p - \mathbf{x}_k|^3} \right] \Delta A_k \right\} \Delta A_p \end{aligned} \quad (26)$$

where

$$\begin{aligned} j &= \text{index of volume element of magnet 1} \\ k &= \text{index of surface element of magnet 1} \\ n &= \text{index of volume element of magnet 2} \\ p &= \text{index of surface element of magnet 2} \end{aligned}$$

Uniform axial magnetization is assumed and the axis of the cylindrical permanent magnet is positioned along the  $z$  axis. All magnetic charge is thought to reside on the top and bottom faces of the magnet. The volume and surface charge densities will then be

$$\begin{aligned} \rho_m &= -\nabla \cdot \mathbf{M} \\ &= -\nabla \cdot M_s \hat{\mathbf{z}} \quad \text{and} \quad \sigma_m = \mathbf{M} \cdot \hat{\mathbf{n}} \\ &= 0 \quad \quad \quad = \pm M_s \end{aligned}$$

Where the  $\pm$  sign of the scalar magnetization  $M_s$  takes into account the polarity of the opposing magnet faces. According to Sommerfeld convention [23, p. 4] the relationship between fields is

$$\mathbf{B} = \mu_0 (\mathbf{H} + \mathbf{M}), \quad (27)$$

where  $\mu_0 = 4\pi \cdot 10^{-7} \text{ T m/A}$  is the permeability of free space. The magnetization of the permanent magnet can be calculated from residual flux density in free air ( $\mathbf{H} = 0$ ) using equation (27)

$$\mathbf{M} = \frac{\mathbf{B}_{\text{Rmax}}}{\mu_0} \quad (28)$$

For both discretized magnets the volume charge density  $\rho_m = 0$  and therefore the equation (26) reduces to

$$\mathbf{F} = \frac{\mu_0}{4\pi} \sum_p \left\{ \sum_k \left[ \frac{\sigma_m(\mathbf{x}_p) \sigma_m(\mathbf{x}_k) (\mathbf{x}_p - \mathbf{x}_k)}{|\mathbf{x}_p - \mathbf{x}_k|^3} \right] \Delta A_k \right\} \Delta A_p \quad (29)$$

As suggested in [23, p. 277] it is easier to derive the force in three steps. First obtaining the force between two point sources, then deriving force between two surfaces and finally summing up the force between all surfaces.

Force for point sources in cylindrical coordinates is

$$F_{z,\text{point}} = \frac{\mu_0}{4\pi} \frac{Q_{m1}(r_1, \phi_1, 0) Q_{m2}(r_2, \phi_2, d_{\text{sep}}) d_{\text{sep}}}{[r_1^2 + r_2^2 - 2r_1 r_2 \cos(\phi_1 - \phi_2) + d_{\text{sep}}^2]^{3/2}} \quad (30)$$

where discretized surface point charge  $Q_m(\mathbf{x}) = \sigma_m(\mathbf{x}) \Delta A$  and where  $\Delta A$  is the area element containing  $\sigma_m(\mathbf{x})$ . More specifically,  $Q_{m1}(\mathbf{x}_1)$  represents the midpoint of one charge at coordinates  $(r_1, \phi_1, 0)$  and  $Q_{m2}(\mathbf{x}_2)$  represents another charge midpoint at coordinates  $(r_2, \phi_2, h)$ . Those coordinates define two planes that are distance  $d_{\text{sep}}$  apart from each other. Summing up the force between each individual surface element yields the total force exerted by two opposing surfaces.

First step is meshing the surface. This can be done by dividing the surface area to equal areas in order to have elements with equal surface charge. Two magnets can have different size hence only the elements on the surface of one magnet are may be the different size than the elements on another magnet but the elements within one magnet are the same size. In all the following equations subscript  $n$  is used to denote the general equation and when number 1 is substituted in place of  $n$  then it belongs to magnet 1. The size of each surface element is

$$\Delta A_n = \frac{\pi R_n^2}{N_r N_\phi}, \quad (31)$$

where  $N_r$  is the number of mesh points along radius and  $N_\phi$  is respectively the number of elements along azimuth. This meshing is illustrated in figure 10, where  $N_r = 3$  and  $N_\phi = 8$ . Midpoint of each surface element represents the charge of the surface. Parameters are collected to table 5. FEM repulsion force calculation algorithm is implemented in Python and the source code is shown in listing 2.

The restoration force of the energy harvester can be calculated as a vector sum of both the force between magnets 1 and 2 ( $F_b$ ) and between 1 and 3 ( $F_t$ ). Since there is only single degree of freedom it reduces to scalar difference between the forces,  $F(z) = F_b(z) - F_t(z)$ . Since top and bottom magnets are identical the force became

$$F(z) = F_s(d_0 + z) - F_s(d_0 - z), \quad (32)$$

where  $d_0$  is the separation between magnets when the moving magnet is precisely in the middle between the top and bottom magnets. If this restoring force is made equal to the gravitational force to the magnet the resting position  $d_{\text{rest}}$  can be solved. This can be solved numerically by interpolating between values that are smaller and greater than the gravity. Linearized spring constant at the resting position can be used to predict the resonance frequency using equation (7).

Table 5: Parameters for Finite Element Method

Parameter	equation
The step size along azimuth	$\Delta\phi = \frac{2\pi}{N_\phi}$
Azimuth towards element center	$\phi_j = (j - 1)\Delta\phi + \frac{\Delta\phi}{2}$
Lower radial boundary of element	$R(i)$
Higher radial boundary of element	$R(i + 1) = \sqrt{R(i)^2 + \frac{R_n^2}{N_r}}$
First radial boundary is zero	$R(1) = 0$
Midpoint along radius	$r_{m,i} = \frac{R(i+1)+R(i)}{2}$

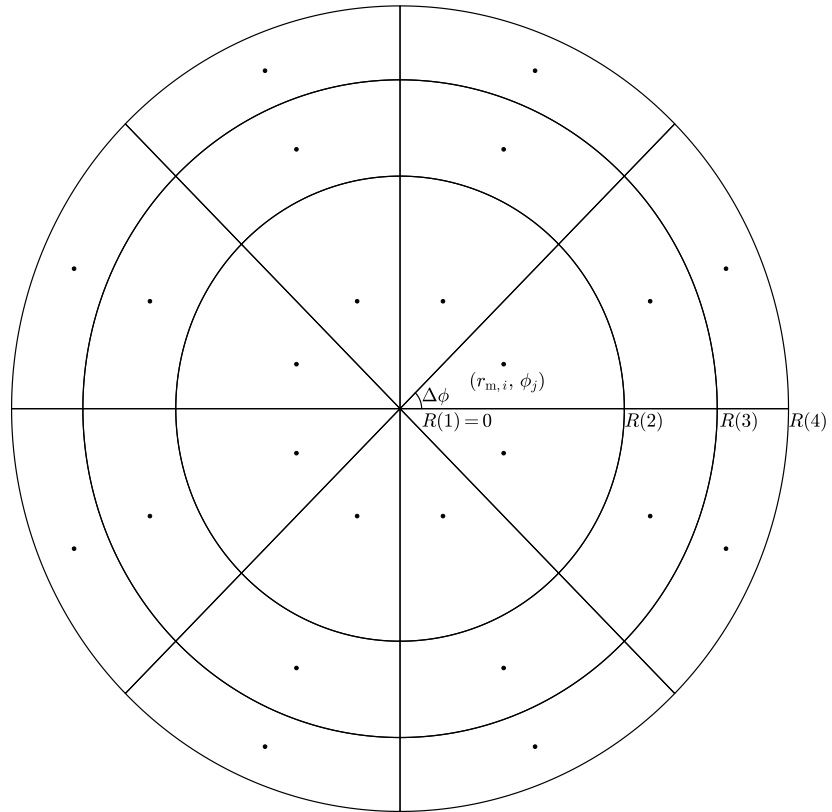


Figure 10: Meshing of the magnet surface.

### 3.2 Power calculation

This section describes the method for calculating output power and output voltage of the harvester. Figure 11 is a flowchart that names the steps and shows in which order they have to be performed and what are the relevant input outputs for each step. Subsections describes these steps in more detail.

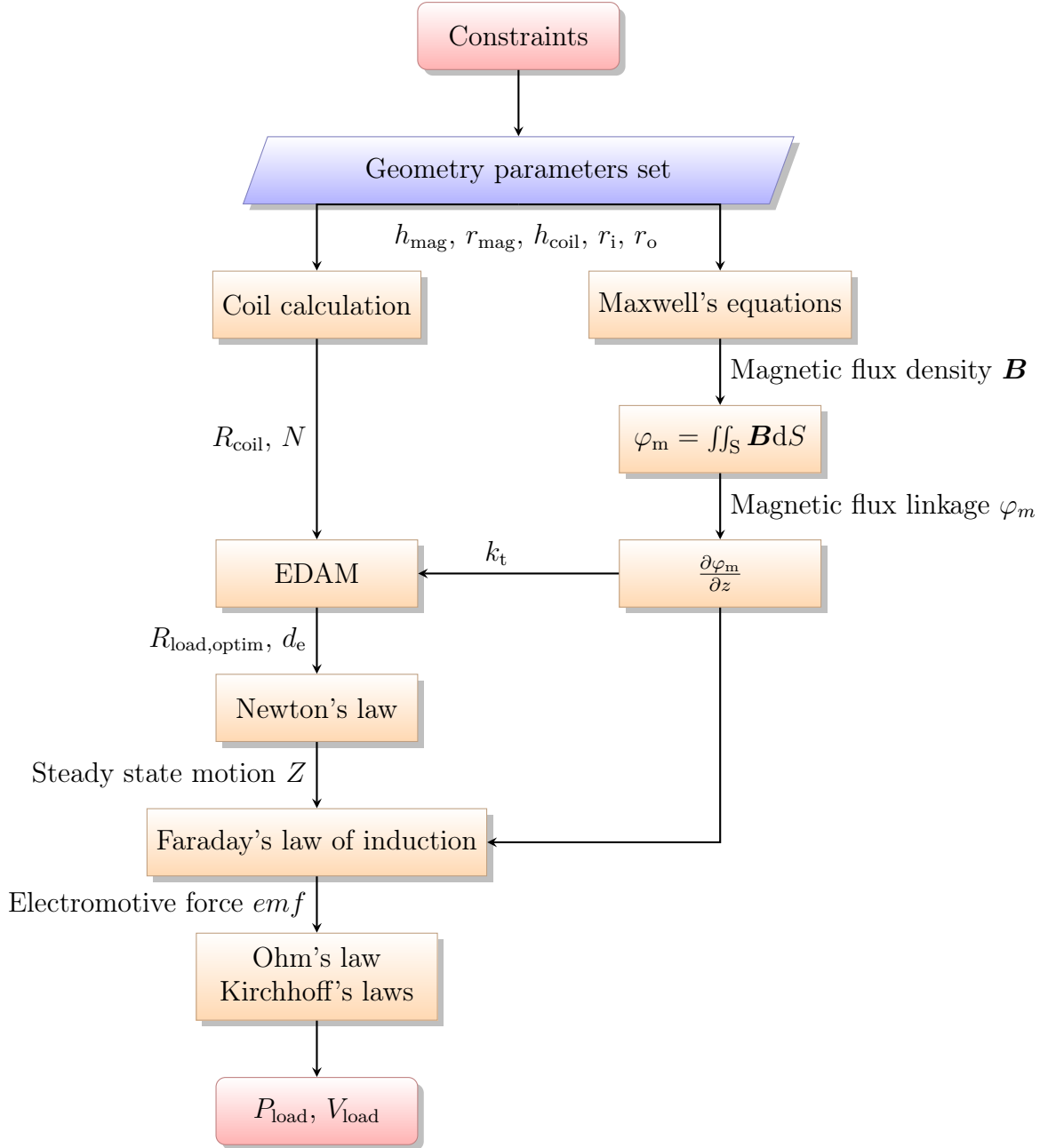


Figure 11: Power calculation flow chart

### 3.2.1 Constraints and geometry parameters

Optimization requires a set of constraints. Customer or end application may set the upper limit to the mass or to the volume of the energy harvester. Similarly the definition set of the optimization variables can come from available manufacturing capabilities like the minimum gap ( $G_c$ ) between the magnet and the coil or the coil fill ratio. In some application one might want to build one or two optimum coils around the pre-selected magnet or the volume of the magnet could be fixed instead of the volume of the entire harvester.

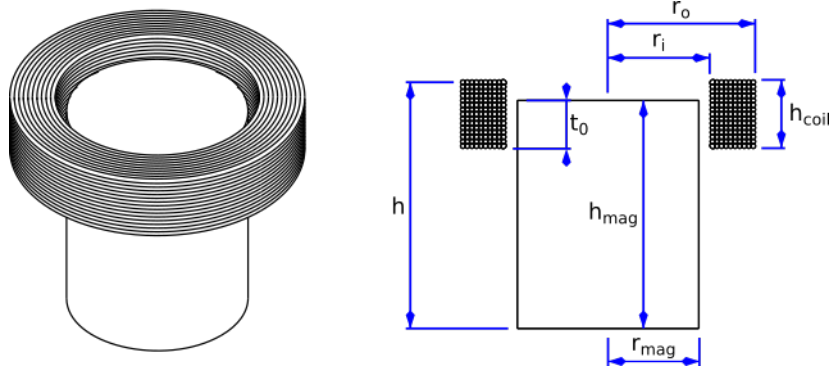


Figure 12: Mechanical dimensions of harvester with one coil.

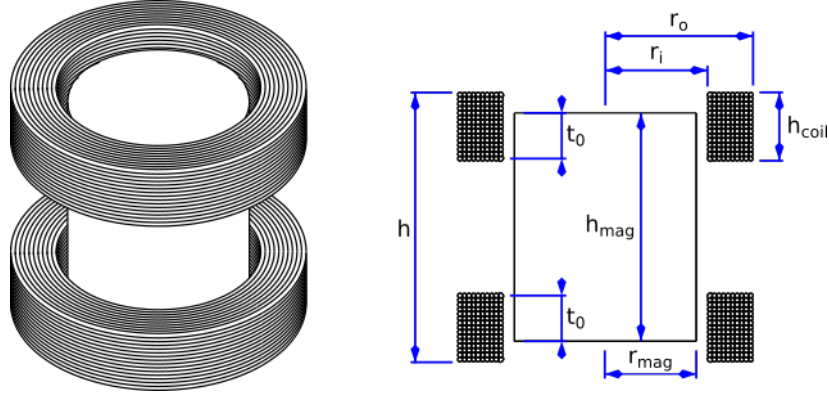


Figure 13: Mechanical dimensions of harvester with two coils.

If the maximum volume ( $V_{\max}$ ) of the harvester is fixed then coil outer radius ( $r_o$ ) can be selected and the construction height

$$h = \frac{V_{\max}}{\pi \cdot r_o^2} \quad (33)$$

can be calculated. Selecting inner radius ( $r_i$ ) allows calculation of magnet radius

$$r_{\text{mag}} = r_i - G_c \quad (34)$$

and finally the coil height ( $h_{\text{coil}}$ ) and magnet resting position ( $t_0$ ) can be used to calculate magnet height

$$h_{\text{mag}} = \begin{cases} h - h_{\text{coil}} + t_0 & (\text{for one coil configuration}) \\ h - 2h_{\text{coil}} + 2t_0 & (\text{for two coil configuration}) \end{cases} \quad (35)$$

### 3.2.2 Coil

Coils are usually made using enamelled wire which have very thin insulation over the conductor. Most common conductors in enamelled wires are copper and aluminum but here only enamelled copper wires are considered because their desirable properties over the alternatives such as high conductivity, good solderability and high ductility. High conductivity allows more turns in the same volume when the resistivity of the coil is held constant.

Enamelled wires are graded according to the thickness of the insulation over the conductor where Grade 1 (single coat) have the thinnest insulation and Grade 3 (triple coat) have the thickest insulation and thus higher breakdown voltage. Even though the absolute thickness of the insulator is thinner with thinner wires its relative thickness is highest with thinnest wires [24]. This relative thickness is illustrated in the Figure 14. Since Grade 1 enamelled wire has 150 V minimum breakdown voltage for 25  $\mu\text{m}$  wire there is no reason to use Grade 2 or Grade 3 wires for this application.

The insulation material determines the temperature class which is defined to be temperate at which it has 20 000 h service life according to IEC 60851. At lower temperatures the service life doubles with every 10  $^{\circ}\text{C}$  decrease in temperature. Only polyurethane have good solderability and it is available in 155  $^{\circ}\text{C}$  and 180  $^{\circ}\text{C}$  temperature classes [24]. If more chemical resistance is needed then Polyesteramide coated wires can be used but it requires high temperature to solder.

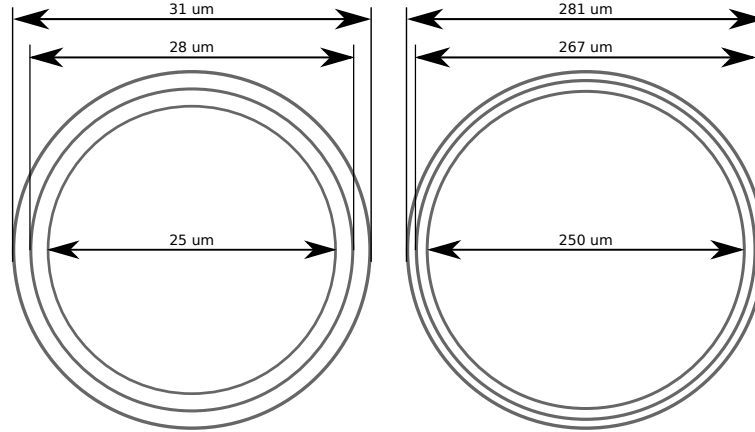


Figure 14: Enamelled wire diameters.

Winding fill factor for perfect square winding pattern is 0.785 while it is 0.907 for perfect hexagonal winding pattern. This hexagonal winding is sometimes referred as orthocyclic winding. Both of the perfect winding factors are illustrated in Figure 15. In practice however, hand-winding the hexagonal pattern starts to deviate from the

perfect pattern after couple of layers and usually starts to resemble random pattern. Therefore the fill factor usually is closer to 0.61 in both winding patterns when hand wound [25, p. 4-6]. Some authors like Spreemann in his book [26] states that it is not possible to calculate copper fill factor theoretically since in practice the layers are unsystematic and hence random winding occurs and it is therefore easier to assume some fill factor like 0.6 as a given. Moreover, this approach allows ignoring the thickness of the insulator around copper wire and using copper fill factor in place of an utilization factor. However, there are several companies for example [27] and [28] that are capable of producing orthocyclic winding down to wire thickness of 50  $\mu\text{m}$ .

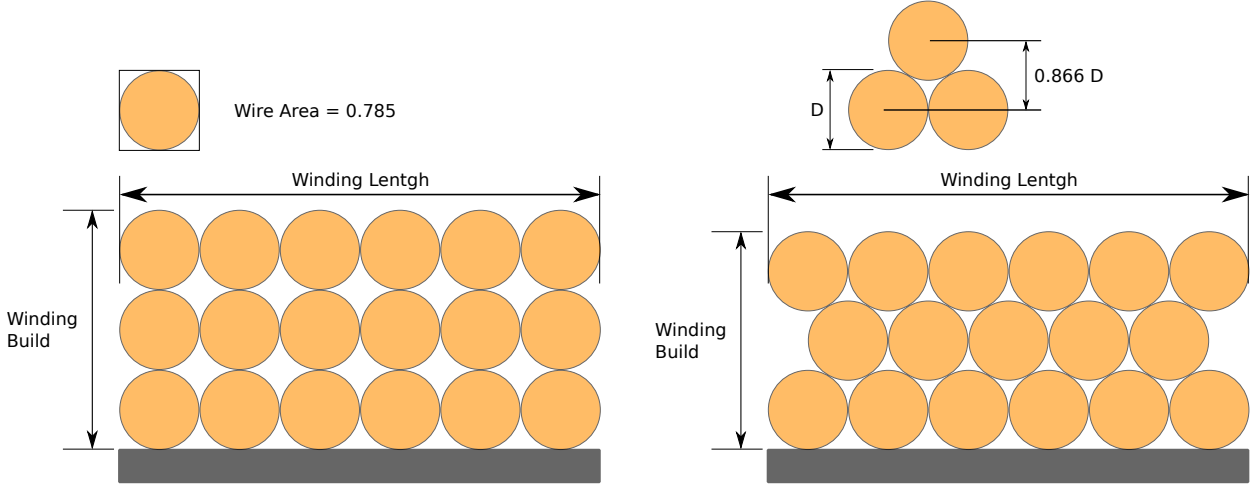


Figure 15: Square winding on left and hexagonal winding on right.

Table 7 illustrates key properties of some easily available sizes of Grade 1 enamelled copper wires. Nominal diameter is the nominal diameter of the conductor, whereas overall diameter is the diameter of the enamelled wire. These values are used in optimization to reduce the search space and to ease material sourcing for prototypes. It is however relatively trivial to add all standard sizes to more exhaustive optimization algorithm.

Table 6: Technical data for Grade 1 enamelled copper wire, based on IEC 60317

Nominal diameter	Overall diameter	$S_1$	Conductor cross section	Resistance at 20 °C	Fill factor wires/cm <sup>2</sup>	Length of 1 kg wire
$\mu\text{m}$	$\mu\text{m}$		$\mu\text{m}^2$	$\Omega/\text{m}$	n	km
25	28 – 31	0.650 – 0.797	491	34.82	132 686	215.1
50	55 – 60	0.694 – 0.826	1 963	8.706	34 925	54.42
100	108 – 117	0.730 – 0.857	7 854	2.176	9 124	13.72
150	162 – 171	0.769 – 0.857	17 671	0.967 3	4 165	6.125
200	214 – 226	0.783 – 0.873	31 416	0.544 1	2 386	3.456
250	267 – 281	0.792 – 0.877	49 087	0.348 2	1 538	2.215

Utilization factor is defined as a product of Insulation ( $S_1$ ) and Fill Factor ( $S_2$ )

$$k_{co} = S_1 S_2,$$

where

$$S_1 = \text{Insulation} = \text{conductor area} / \text{wire area}$$

$$S_2 = \text{Fill Factor} = \text{wound area} / \text{usable window area}$$

Table 7: Windows utilization

Nominal diameter $\mu\text{m}$	$S_1$	$K_u$ (Utilization factor)		
		Random winding $S_2 = 0.61$	Square winding $S_2 = 0.785$	Hexagonal winding $S_2 = 0.907$
25	0.650 – 0.797	0.397 – 0.486	0.510 – 0.626	0.590 – 0.723
50	0.694 – 0.826	0.424 – 0.504	0.545 – 0.649	0.630 – 0.750
100	0.730 – 0.857	0.446 – 0.523	0.573 – 0.673	0.663 – 0.778
150	0.769 – 0.857	0.469 – 0.523	0.604 – 0.673	0.698 – 0.778
200	0.783 – 0.873	0.478 – 0.533	0.615 – 0.686	0.710 – 0.792
250	0.792 – 0.877	0.483 – 0.535	0.621 – 0.688	0.718 – 0.795

and it can be understood as a cross-sectional area of the copper of all wires ( $A_{co}$ ) in the coil divided by the winding area ( $A_w$ ) of the coil [26]

$$k_{co} = \frac{A_{co}}{A_w} = \frac{N \cdot \frac{\pi \cdot d_{co}^2}{4}}{(r_o - r_i) \cdot h_{coil}}, \quad (36)$$

where  $d_{co}$  is the nominal wire diameter without insulation and  $N$  is number of turns in coil which. Equation (36) can be solved for  $N$  and divided to radial and axial components

$$N = \frac{4(r_o - r_i) \cdot h_{coil} \cdot k_{co}}{\pi \cdot d_{co}^2} \quad (37)$$

$$N_r = \frac{2 \cdot (r_o - r_i)}{d_{co} \sqrt{\pi/k_{co}}} \quad (38)$$

$$N_z = \frac{2 \cdot h_{coil}}{d_{co} \sqrt{\pi/k_{co}}} \quad (39)$$

The volume of the copper ( $V_{co}$ ) can be calculated using basic geometry

$$V_{co} = \pi \cdot (r_o^2 - r_i^2) \cdot h_{coil} \cdot k_{co}$$

when this is set equal to the volume of straight wire, the of length ( $l$ ) of the wire can be solved

$$l = N \cdot \pi \cdot (r_o + r_i) \quad (40)$$



Pouillet's law states that the resistance of the coil ( $R_{\text{coil}}$ ) can be calculated using formula

$$R_{\text{coil}} = \rho \cdot \frac{l}{A} = \rho \cdot \frac{4 \cdot N \cdot (r_o + r_i)}{d_{\text{co}}^2}, \quad (41)$$

where  $\rho$  is the resistivity of the enameled copper wire and its nominal value is  $1.709 \cdot 10^{-8} \Omega \text{ m}$  as specified by the wire manufacturer [24].

### 3.2.3 Magnetic flux density

First step in calculating electromagnetic coupling is to calculate magnetic flux density distribution of a permanent magnet. Permanent magnet can be represented using the current model in which magnet is composed from a distribution of equivalent current [23, p. 126]. This representation allows solving magnetostatic field equations using standard methods for steady current. In other words, the magnetic field generated by the permanent magnet is identical to that of a thin solenoid with the same dimensions. Surface current density of uniformly magnetized cylindrical magnet that is polarized along its axis is

$$\mathbf{j}_m = \mathbf{M} \times \hat{n} = M_s \hat{z}$$

Solving Biot-Savart law

$$\mathbf{B}(\mathbf{x}) = \frac{\mu_0}{4\pi} \oint_S \mathbf{j}_m(\mathbf{x}') \times \frac{(\mathbf{x} - \mathbf{x}')}{|\mathbf{x} - \mathbf{x}'|^3} ds'$$

over the magnet surface results for z-component (along the axis of the magnet)

$$B_z(z) = \frac{\mu_0 M_s}{2} \left( \frac{z + L}{\sqrt{(z + L)^2 + R^2}} - \frac{z}{\sqrt{z^2 + R^2}} \right)$$

This result and its derivation is shown in many textbooks like in [23, p. 129] but the B-field calculations for off-axis positions are usually missing. The reason for this is that there are no analytical solution available for off-axis positions. This field can be solved using numerical methods (FEM) or using semi-analytical methods like elliptical integrals. Solutions for elliptical integrals can be either tabulated or solved on-the-fly with modern computers. Foelsch is the first author who have published [29] off-axis magnetic field calculations for cylindrical solenoid. He published the equations in two forms and the first form is referred to as Foelsch1 from now on. Equations originally gave results in Oersted but they are adopted here in a form that uses SI-units

$$B_z(z, r) = \mu_0 \cdot \frac{NI}{2\pi h_{\text{mag}}} \cdot [A_2(n, \beta_2) \pm A_1(n, \beta_1)], \quad \text{for } r \leq r_{\text{mag}} \quad (42)$$

$$B_z(z, r) = \mu_0 \cdot \frac{NI}{2\pi h_{\text{mag}}} \cdot [B_2(n, \beta_2) \pm B_1(n, \beta_1)], \quad \text{for } r > r_{\text{mag}} \quad (43)$$

where plus sign is used inside magnet ( $0 < z < h_{\text{mag}}$ ) and minus sign otherwise. The numerator contains terms  $N$  (number of turns) and  $I$  (current in the winding)

which can be replaced with the following identity when the area  $A$  is assumed to be orthogonal to coil winding [26, p. 45]

$$NI = \int \int_A \mathbf{S} \cdot \mathbf{n} \, d\mathbf{A} = \oint_C \mathbf{M}_r \cdot d\mathbf{s} = M \cdot h_{mag} = \left( \frac{B_r}{\mu_0} \right) \cdot h_{mag} \quad (44)$$

Substituting this to the equations (42) and (43)

$$B_z(z, r) = \frac{B_r}{2\pi} \cdot [A_2(n, \beta_2) \pm A_1(n, \beta_1)], \quad \text{for } r \leq r_{mag} \quad (45)$$

$$B_z(z, r) = \frac{B_r}{2\pi} \cdot [B_2(n, \beta_2) \pm B_1(n, \beta_1)], \quad \text{for } r > r_{mag} \quad (46)$$

The in (45) and (46) terms are defined as

$$A_2(n, \beta_2) = (E_2 + \Pi_2 \sqrt{1-n}) \sqrt{1-\beta_2} \quad (47)$$

$$A_1(n, \beta_1) = (E_1 + \Pi_1 \sqrt{1-n}) \sqrt{1-\beta_1} \quad (48)$$

$$B_2(n, \beta_2) = (E_2 - \Pi_2 \sqrt{1-n}) \sqrt{1-\beta_2} \quad (49)$$

$$B_1(n, \beta_1) = (E_1 - \Pi_1 \sqrt{1-n}) \sqrt{1-\beta_1} \quad (50)$$

$$(51)$$

where the complete elliptical integral of the second kind is defined as [30, p. 10]

$$E_k = E(\pi/2, k) = \int_0^{\pi/2} \sqrt{1 - k^2 \sin^2 \varphi} \, d\varphi \quad (52)$$

and the complete elliptical integral of the third kind is defined as [30, p. 10]

$$\Pi_k = \Pi(\pi/2, n, k) = \int_0^{\pi/2} \frac{d\varphi}{(1 - n \sin^2 \varphi) \sqrt{1 - k^2 \sin^2 \varphi}} \quad (53)$$

where

$$k_2^2 = \beta_2 \cdot n = \frac{4r_{mag}r}{(r_{mag} + r)^2 + z_2^2} \quad (54)$$

$$k_1^2 = \beta_1 \cdot n = \frac{4r_{mag}r}{(r_{mag} + r)^2 + z_1^2} \quad (55)$$

Since the elliptic integral of the third integral is computationally more intensive to calculate and it is not normally tabulated it is possible to solve  $A$  and  $B$  using only first and second kind of complete and incomplete elliptical integrals [29]. This method is called as Foelch2 from now on

$$A(n, \beta) = \frac{\pi}{2} + K \cdot \sqrt{1-\beta}(1 + \sqrt{1-n}) + F(b, \varphi) \cdot (K - E) - K \cdot E(b, \varphi) \quad (56)$$

$$B(n, \beta) = 2 \cdot K \cdot \sqrt{1-\beta} - A(n, \beta) \quad (57)$$

$$\sin^2 \varphi = \frac{1-n}{1-k^2} \quad (58)$$

where the incomplete and complete integral of the first kind are in the same order [30, p. 9]

$$F = F(\varphi, k) = \int_0^\varphi \frac{d\varphi}{\sqrt{1 - k^2 \sin^2 \varphi}} \quad (59)$$

$$K = F(\pi/2, k) \quad (60)$$

Similarly incomplete integrals of second kind are only integrated up to  $\varphi$  instead of  $\pi/2$

$$E(\varphi, k) = \int_0^\varphi \sqrt{1 - k^2 \sin^2 \varphi} d\varphi \quad (61)$$

The literature presents alternative algorithms for calculating magnetic flux density. NASA have made a technical note [31] where they derived alternative algorithm for axial component of the magnetic flux density

$$B_z = \frac{B_r}{4} \cdot \left[ \frac{\xi k}{\pi \sqrt{ar}} K + \frac{(a-r)\xi}{|(a-r)\xi|} \lambda_0(\varphi, k) \right]_{\xi_-}^{\xi_+} \quad (62)$$

where  $a$  is the radius of the solenoid,  $\xi_{\pm} = z \pm \frac{L}{2}$  is the z-distance from the both ends of the solenoid and

$$\varphi = \tan^{-1} \left| \frac{\xi}{a-r} \right| \quad (63)$$

$$k^2 = \frac{4ar}{\xi^2 + (a+r)^2} \quad (64)$$

The  $\lambda_0(\varphi, k)$  is a lambda function which is defined as [30, p. 36]

$$\lambda_0(\varphi, k) = \frac{2}{\pi} [EF(\varphi, k') + KE(\varphi, k') - KF(\varphi, k')] \quad , \text{ where } k' = \sqrt{1 - k^2} \quad (65)$$

Another alternative algorithm that uses generalized elliptical integrals  $C(k_c, p, c, s)$  [32]. This algorithm is called Derby from now on.

$$B_z = \frac{B_0 a}{a+r} [\beta_+ C(k_+, \lambda^2, 1, \lambda) - \beta_- C(k_-, \lambda^2, 1, \lambda)] \quad (66)$$

$$z_{\pm} = z \pm b = z \pm \frac{L}{2} \quad (67)$$

$$B_0 = \frac{\mu_0 N I}{\pi h_{mag}} \quad (68)$$

$$\beta_{\pm} = \frac{z_{\pm}}{\sqrt{z_{\pm}^2 + (r+a)^2}} \quad (69)$$

$$\lambda = \frac{a-r}{a+r} \quad (70)$$

$$k_{\pm} = \sqrt{\frac{z_{\pm}^2 + (a-r)^2}{z_{\pm}^2 + (a+r)^2}} \quad (71)$$

$$C(k_c, p, c, s) = \int_0^{\pi/2} \frac{c \cos^2 \varphi + s \sin^2 \varphi}{(\cos^2 \varphi + p \sin^2 \varphi) \sqrt{\cos^2 \varphi + k_c^2 \sin^2 \varphi}} d\varphi \quad (72)$$

Implementing magnetic flux calculation using several different algorithms made it possible to verify the correctness of the algorithm implementation. Figure 16 presents the results along the axis of the cylindrical magnet from the four different algorithms and compare them to the analytical formula (3.2.3). The relative errors are less than  $4 \cdot 10^{-13}$  for all algorithms, less than  $3 \cdot 10^{-14}$  for Nasa and less than  $1 \cdot 10^{-14}$  for Derby. Only Foelsch1 and Foelsch2 results noticeable peak at the magnet surface. Figure 17 presents results along the radius of the magnet. Since there are no analytical equation for reference for radial direction Derby is used as a reference. Again the Foelsch1 and Foelsch2 behave differently near the magnet wall. Relative difference between Nasa and Derby is less than  $5 \cdot 10^{-13}$ . The axial component of the magnetic flux density is illustrated in Figure 18 as a contour map. In this case there is no analytical equation to be compared with. Additional benefit from algorithm diversity is the possibility to compare the execution speed of the algorithms. Figure 19 shows that the Derby is the fastest of all algorithms by a significant margin.

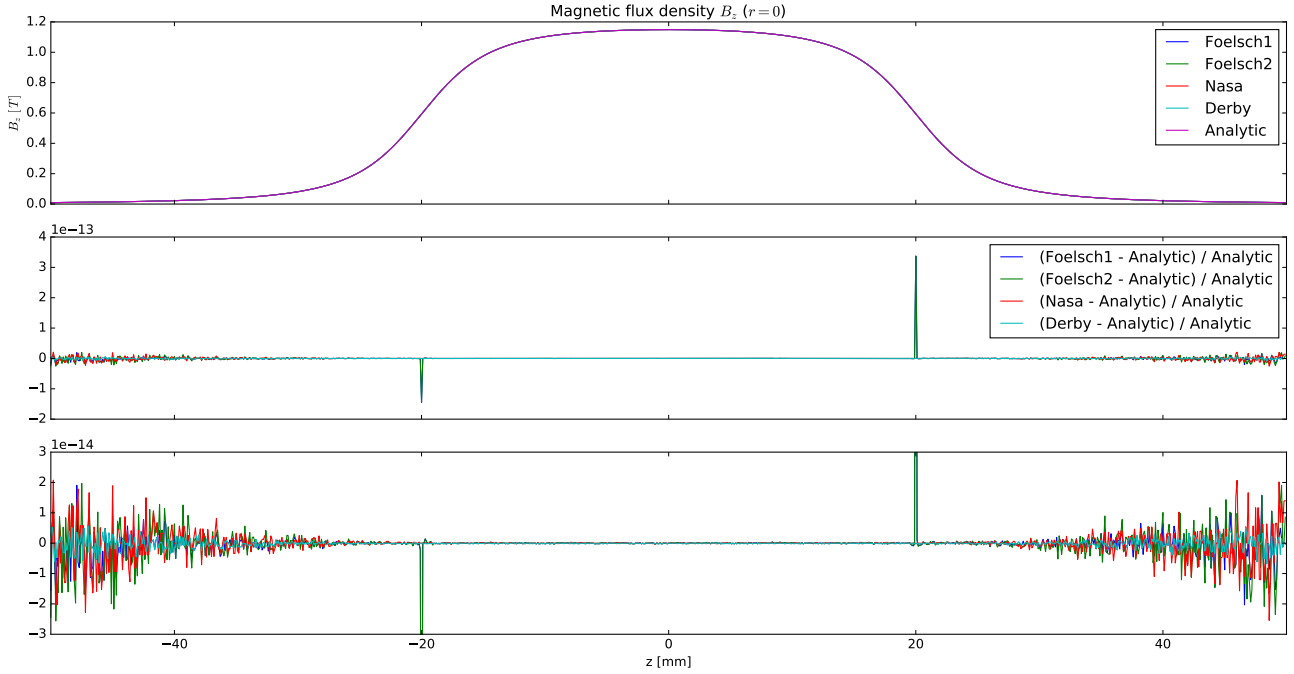


Figure 16: Axial component of magnetic flux density of a permanent magnet ( $h_{\text{mag}} = 40$  mm) along the axis.

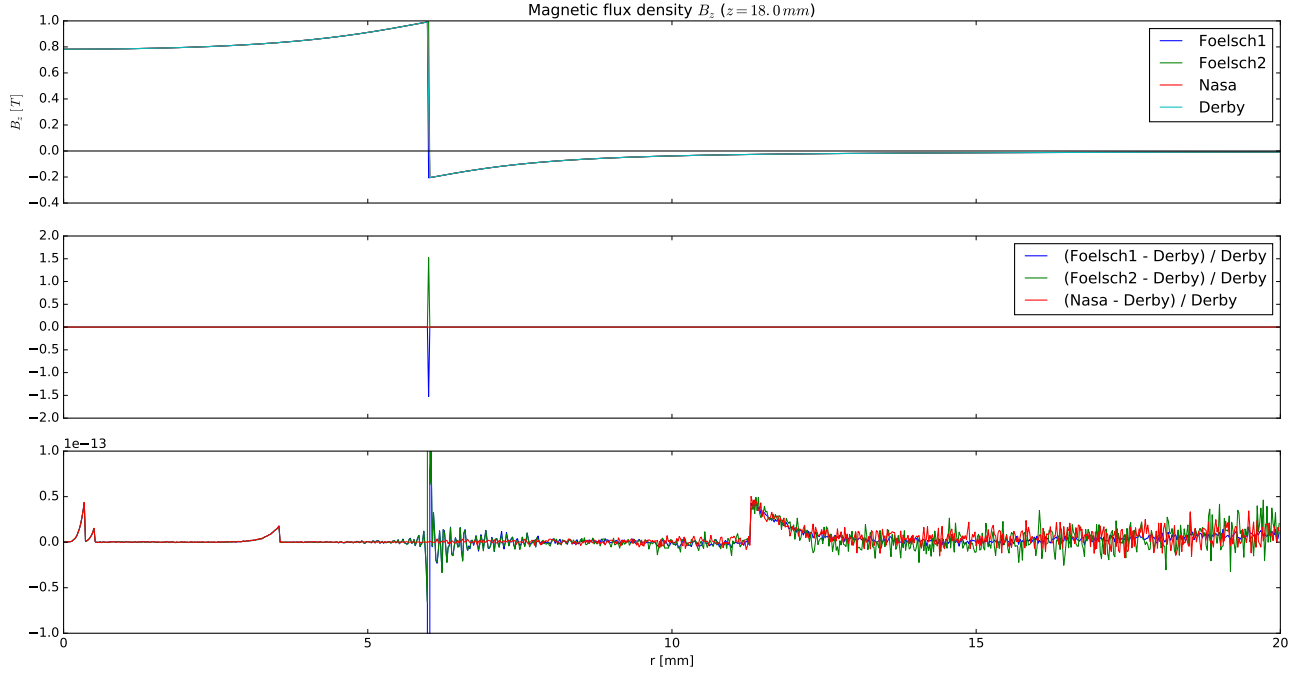


Figure 17: Axial component of magnetic flux density of a permanent magnet ( $r_{\text{mag}} = 6$  mm) along the radius.

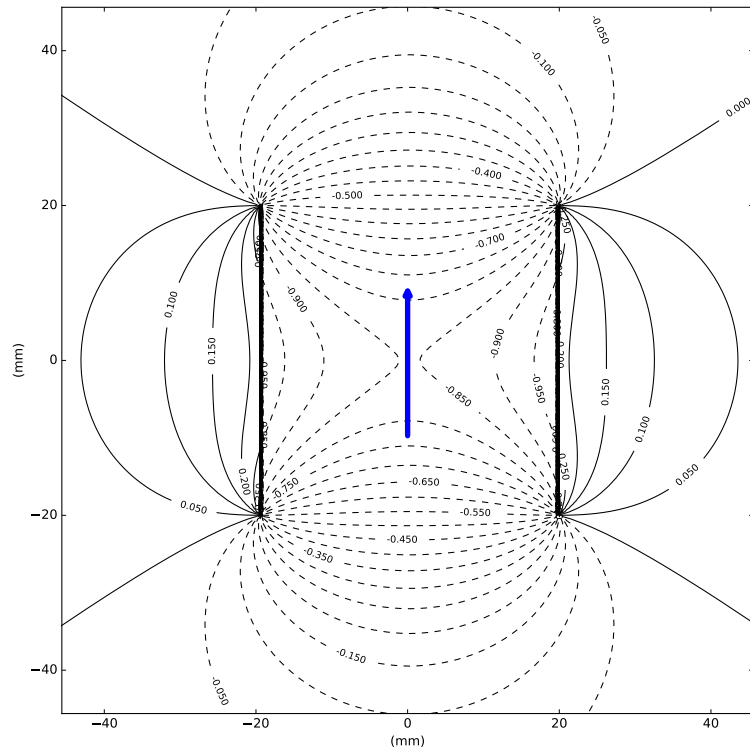


Figure 18: Contour map of the axial component of the magnetic flux density

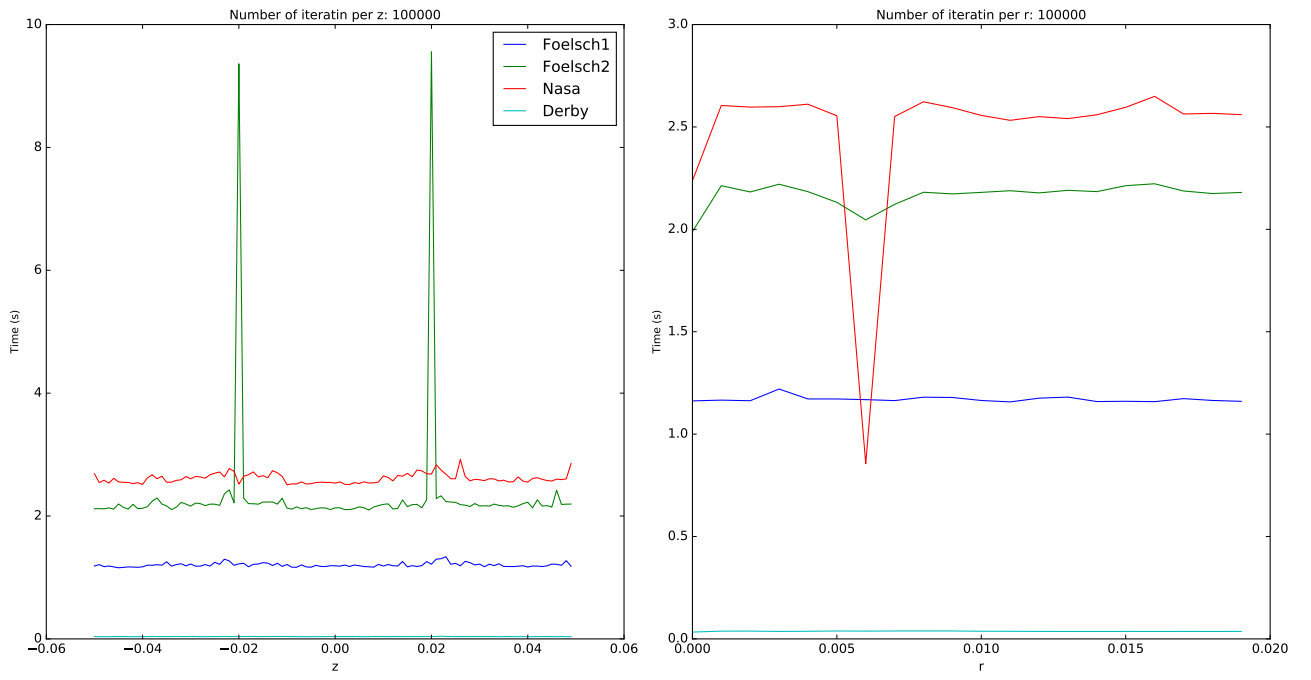


Figure 19: Execution speed of different flux density algorithms.

### 3.2.4 Magnetic flux linkage

Previous section described how to calculate magnetic flux density for cylindrical permanent magnet. This section consider the previous calculation to predict flux linkage in a coil.

Flux linkage for single coil turn is defined as total magnetic field ( $\mathbf{B}$ ) passing through a surface ( $S$ ) which can be presented as a single integral along radius  $r$

$$\varphi_m = \iint_S \mathbf{B} \cdot d\mathbf{S} = \int_0^r \mathbf{B} \cdot 2 \cdot \pi \cdot r \cdot dr,$$

where  $\mathbf{B}$  is magnetic flux density and  $d\mathbf{S}$  is surface element. To calculate the flux linkage for the whole coil can be achieved by summing the flux linkage of each turn. The flux linkage for the coil becomes

$$\varphi_m = \sum_{i=1}^n \iint_{S_i} \mathbf{B}(r, z_i) \cdot d\mathbf{S} = \sum_{i=1}^n \int_0^{r_i} \mathbf{B}(r, z_i) \cdot 2 \cdot \pi \cdot r \cdot dr \quad (73)$$

It is important to note that here the coil is three-dimensional object and that the  $r$  is distance from z-axis rather than distance from origin. To make it more explicit the flux linkage equation could be written in a form

$$\varphi_m = \sum_{j=1}^{N_z} \sum_{d=0}^{N_r} \int_0^{r_{j,d}} \mathbf{B}(r, z_j) \cdot 2 \cdot \pi \cdot r \cdot dr \quad (74)$$

Before performing the numerical computation, special attention should be given. First the magnetic flux density shall not be calculated at the magnet cylinder walls because the function is not defined there. Secondly, to gain maximum accuracy with the smallest number of calculation steps the discretization step  $dr$  shall not cross the discontinuation. Both of these requirements can be satisfied by dividing the integration to three phases, from zero to  $r_{\text{mag}}$ , from  $r_{\text{mag}}$  to  $r_i$  and from  $r_o$ . Discretization steps become

$$\Delta z = \frac{h_{\text{coil}}}{\text{round}(N_z)}, \quad \Delta r_a = \frac{r_{\text{mag}}}{\text{parts}}, \quad \Delta r_b = \frac{r_i - r_{\text{mag}}}{\text{parts}}, \quad \Delta r_c = \frac{r_o - r_i}{\text{round}(N_r)} \quad (75)$$

where *parts* is the number of parts the discretization region is divided. Thirdly, the number of radial ( $N_r$ ) or axial turns ( $N_z$ ) may not be integer. It is easier to round  $N_r$  and  $N_z$  to the closest integer and then compensate it by multiplying the result with  $\Delta N$

$$\Delta N = \frac{N_z}{\text{round}(N_z)} \cdot \frac{N_r}{\text{round}(N_r)} \quad (76)$$

Numerical calculation of magnetic flux linkage becomes

$$\varphi_m(z_{\text{dist}}) = \Delta N \cdot \sum_{j=0}^{N_z} \sum_{d=0}^{N_r} (\varphi_{m,a} + \varphi_{m,b} + \varphi_{m,c}) \quad (77)$$

where

$z_{\text{dist}} = \text{distance from magnet center to coil center}$

$$z_j = j \cdot \Delta z + \frac{\Delta z}{2} + z_{\text{dist}} - \frac{h_{\text{coil}}}{2}$$

$$r_a = a \cdot \Delta r_a + \frac{\Delta r_a}{2}$$

$$r_b = b \cdot \Delta r_b + \frac{\Delta r_b}{2} + r_{\text{mag}}$$

$$r_c = c \cdot \Delta r_c + \frac{\Delta r_c}{2} + r_i$$

$$\varphi_{\text{m,a}} = \sum_{a=0}^{\text{parts}} B_z(r_a, z_j) \cdot 2 \cdot \pi \cdot r_a \cdot \Delta r_a$$

$$\varphi_{\text{m,b}} = \sum_{b=0}^{\text{parts}} B_z(r_b, z_j) \cdot 2 \cdot \pi \cdot r_b \cdot \Delta r_b$$

$$\varphi_{\text{m,c}} = \sum_{c=0}^d B_z(r_c, z_j) \cdot 2 \cdot \pi \cdot r_c \cdot \Delta r_c$$

It can be seen from Figure 20 that the axial component of the flux linkage approaches asymptotically the final value and that there will be diminishing returns with increase in the number parts.

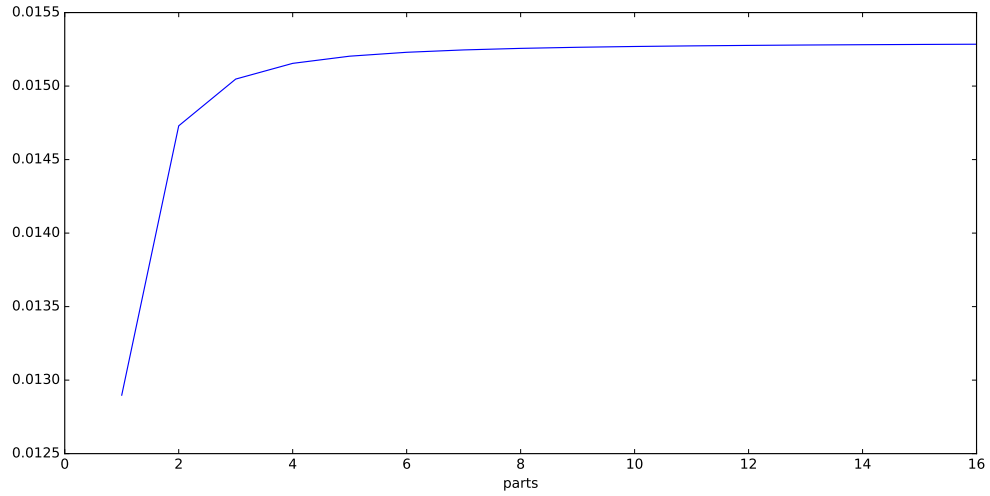


Figure 20: Flux linkage as a function of parts.

Program listing can be found from Appendix B.

### 3.2.5 Transconductance factor

Transconductance factor is partial derivative of magnetic flux linkage with respect to distance and it is assumed to be constant [26, p. 21]. This assumption can be taken



if the amplitude of the magnet movement is assumed to be small. Transduction factor can be expressed as

$$k_t = \frac{\partial \varphi_m}{\partial z} \quad (78)$$

This can be discretized as

$$k_t(z) = \frac{\varphi_m(z + \Delta z) - \varphi_m(z - \Delta z)}{2 \cdot \Delta z} \quad (79)$$

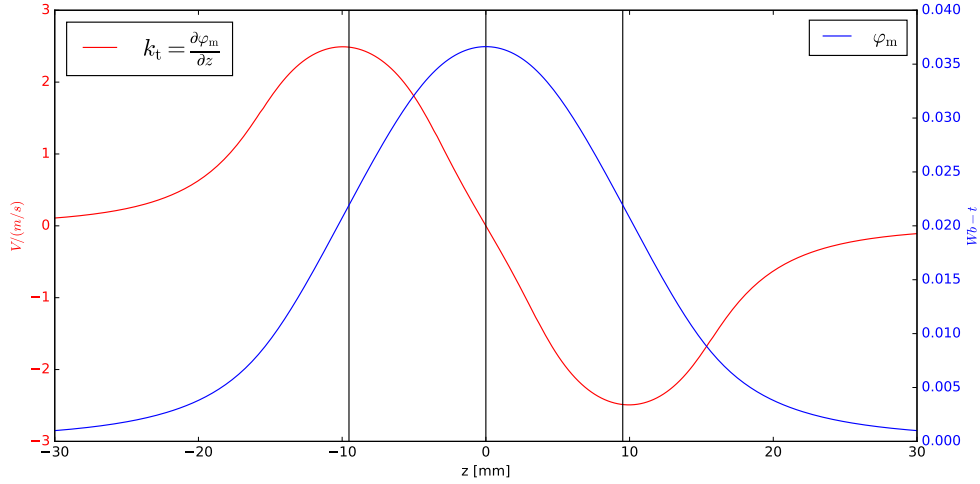


Figure 21: Flux linkage and transconductance factor as a function of  $z$ .

### 3.2.6 Electrical Domain Analog Matching

In a spring-mass-damper energy harvesting systems the force is proportional to the current and the voltage is proportional to the velocity of the magnet [33].

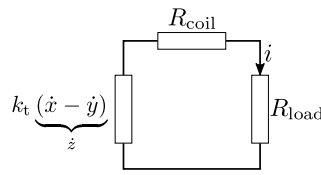


Figure 22: Electrical matching.

Electromagnetical system represented for circuit analysis is shown in Figure 22. Kirchhoff's voltage law and Newton's second law [33]

$$\begin{cases} i(R_{\text{coil}} + R_{\text{load}}) - k_t \dot{z} &= 0 \\ -kz - d_m \dot{z} - k_t i &= m\ddot{x} \end{cases} \implies m\ddot{x} + d_m \dot{z} + kz = 0 \quad (80)$$

where  $y$  and  $\dot{y}$  are the amplitude and velocity of the base excitation respectively,  $x$  and  $\dot{x}$  are the position and velocity of the moving magnet relative to the harvester

frame,  $z$  and  $\dot{z}$  are position and velocity of the moving magnet relative to base,  $k$  is the spring constant,  $m$  is the mass of the magnet,  $d_m$  is mechanical damping coefficient sometimes called parasitic viscous damping and  $d$  is the total damping coefficient

$$d = d_m + d_e = d_m + \frac{k_t^2}{R_{\text{coil}} + R_{\text{load}}} \quad (81)$$

Electrical damping can be divided to electrical damping in duo to load  $c_{e,\text{load}}$  and coil internal resistance  $c_{e,\text{loss}}$  [33]

$$d_{e,\text{loss}} = \frac{k_t R_{\text{coil}}}{(R_{\text{coil}} + R_{\text{load}})^2} \quad (82)$$

$$d_{e,\text{load}} = \frac{k_t R_{\text{load}}}{(R_{\text{coil}} + R_{\text{load}})^2} \quad (83)$$

$$d_e = d_{e,\text{loss}} + d_{e,\text{load}} = \frac{k_t^2}{R_{\text{coil}} + R_{\text{load}}} \quad (84)$$

Electrical Domain Analog Matching (EDAM) results the optimum load resistance  $R_{\text{load,optim}}$  [33]

$$R_{\text{load,optim}} = R_{\text{coil}} + \frac{k_t^2}{d_m} \quad (85)$$

Research article [33] presents comprehensive analysis of all previous attempts to find optimal load impedance for electromagnetical energy harvester. The validation of EDAM was excluded from this thesis due to limitation of time and resources but it is believed to be sound since it is used widely on other research articles and Scopus reports that it have been cited 404 times.

The steady state amplitude is  $Z$  which simplifies when the oscillation is at the resonant frequency [34]

$$Z = \frac{\overbrace{m \omega^2 Y}^a}{\sqrt{\underbrace{(k - m \omega^2)}_0 + ((d_e + d_m) \omega)^2}} = \frac{ma}{(d_e + d_m) \omega} \quad (86)$$

where  $\omega = 2\pi f$

Faraday's law of induction gives

$$emf = -\frac{d\varphi_m}{dt} = -\frac{d\varphi_m}{dz} \cdot \frac{dz}{dt} = k_t \dot{z} \quad (87)$$

where  $\dot{z} = \omega Z$

### 3.2.7 Output voltage and power

The voltage over the load resistor and the output power to the load can be calculated when Kirchhoff's and Ohm's laws are applied

$$V_{\text{load,optim}} = emf \cdot \frac{R_{\text{load,optim}}}{R_{\text{load,optim}} + R_{\text{coil}}} \quad (88)$$

$$P_{\text{load,optim}} = \frac{V_{\text{load,optim}}^2}{R_{\text{load,optim}}} \quad (89)$$

## 4 Model validation

Where the previous chapter derived computational model for energy harvesters this chapter measures prototypes and validates the model. Section 4.1 describes the prototypes created. 4.2 measures the viscous damping and compares it to the calculated values. Section 4.3 validates the magnetic spring restoration force calculation. Section 4.4 validates the equation used to predict the coil resistance. Section 4.5 validates the flux linkage calculation. Section 4.6 validates the power calculation algorithm against values found from the literature. Section Finally, Section 4.7 measures the prototypes using vibration generator.

### 4.1 Design of the Prototypes

First three prototypes were made to be compared with the analytical model. These were not optimized but just a three different constructions. The main difference between prototypes 1 and 2 is that the coil is positioned differently. Prototype 1 have one magnet end at the middle of the coil when the magnet is in its resting position, in other words  $t_0 = 0.85 \cdot h_{\text{coil}}$ . Prototypes 2 and 3 have the coil approximately in the middle of the magnet when the magnet is in its resting position.

Table 8: Prototype parameters for first three prototypes

Parameter	Prototype 1	Prototype 2	Prototype 3
$N$	3046	3000	1600
$d_{\text{co}}$	100 $\mu\text{m}$	100 $\mu\text{m}$	150 $\mu\text{m}$
$m_{\text{mag1}}$ (meas)	10.25 g	10.25 g	28.49 g
$m_{\text{mag1}}$ (calc)	10.32 g	10.32 g	28.66 g
$h_{\text{mag1}}$	19.05 mm	19.05 mm	19.05 mm
$r_{\text{mag1}}$	4.762 5 mm	4.762 5 mm	7.937 5 mm
$B_{\text{r,mag1}}$	1.31 T	1.31 T	1.32 T
$h_{\text{mag2}}$	3.175 mm	3.175 mm	3.0 mm
$r_{\text{mag2}}$	4.762 5 mm	4.762 5 mm	7.5 mm
$B_{\text{r,mag2}}$	1.31 T	1.31 T	1.37 T
$h_{\text{coil}}$	6.2 mm	7.0 mm	6.1 mm
$r_{\text{i}}$	6.025 mm	6.025 mm	9.9 mm
$r_{\text{o}}$	12.1 mm	12.65 mm	17.5 mm
$h_{\text{mm}}$	85.5 mm	85.5 mm	77.5 mm
$d_{\text{rest}}$	-7.73 mm	-7.73 mm	-2.2 mm

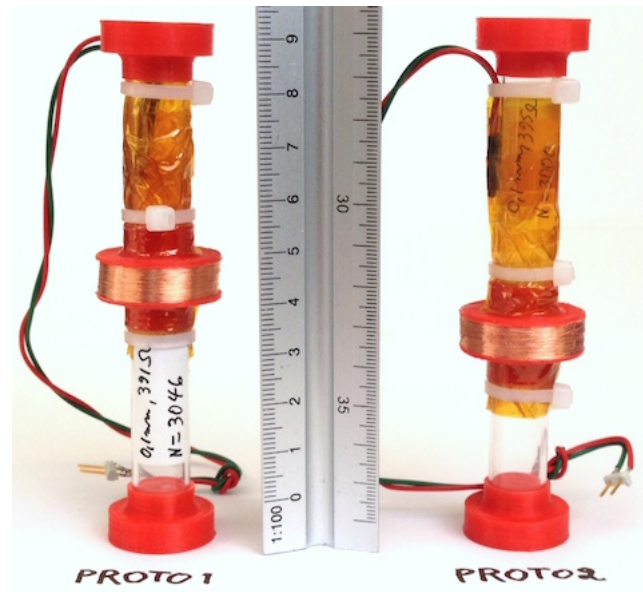


Figure 23: Prototype 1 on the left and Prototype 2 on the right.



Figure 24: Prototype 3.

## 4.2 Viscous damping measurements

This section calculates theoretical values for viscous damping using (21) and compares them with measurements. Dynamic viscosity of the air at room temperature is  $\mu_{275K} = 1.725 \times 10^{-5} \text{ kg/(ms)}$ , moving magnet height  $h_{\text{mag}} = 19.05 \text{ mm}$ , moving magnet radius  $r_{\text{mag}} = 4.7625 \text{ mm}$  and air gap between magnet and the wall  $G_w = 0.2375 \text{ mm}$ . The measured inner diameter of the tube and the nominal diameter of the magnet  $2r_{\text{mag}}$  was used to calculate the gap  $G_w$ . The measured magnet radius was  $4.76 \text{ mm} \pm 0.01 \text{ mm}$ . Since the coil not connected to the load the electrical damping  $d_e = 0$  and hence  $d = d_m$ . Table 9 shows theoretical damping coefficients with  $G_w$  variations. Figure 25 shows the damping coefficients as a function of a gap  $G_w$ . It is easy to see that damping increases as the air gap decreases.

Table 9: Viscous damping coefficients for prototypes 1 and 2

$G_w$		$d_m$
%	mm	N s/m
-55	0.107	0.530
-50	0.119	0.385
-40	0.143	0.221
-20	0.190	0.092
0	0.237	0.046
+20	0.285	0.026

Measuring the damping ratio of the system requires the measurement of the dynamic response of the system. It is also difficult to measure the displacement or velocity of the moving mass inside the closed system. However, the open circuit voltage of the harvester is directly related to the speed of the magnet which means that the waveform is the same only the scaling and the units are different. Initial speed was given to a moving magnet and the coil voltage response was measured. Figure 26 shown the results of one such measurement.

Voltage peaks are used to calculate the damping logarithmic decrement  $\delta$ , damping ratio  $\zeta$  and damping coefficient  $c$  [21, pp. 52–53]. These are calculated for prototype 1, which have a moving magnet with mass 10.25 g, in a table 10.

$$\delta = \frac{1}{n} \ln \frac{x(t)}{x(t+nT)} = \ln e^{\zeta \omega_n T} = \zeta \omega_n T \quad (90)$$

$$\zeta = \frac{\delta}{\sqrt{4\pi^2 + \delta^2}} = \frac{d}{2m\omega_n} \quad (91)$$

$$d = 2m\zeta\omega_n = \frac{2m\delta}{T} \quad (92)$$

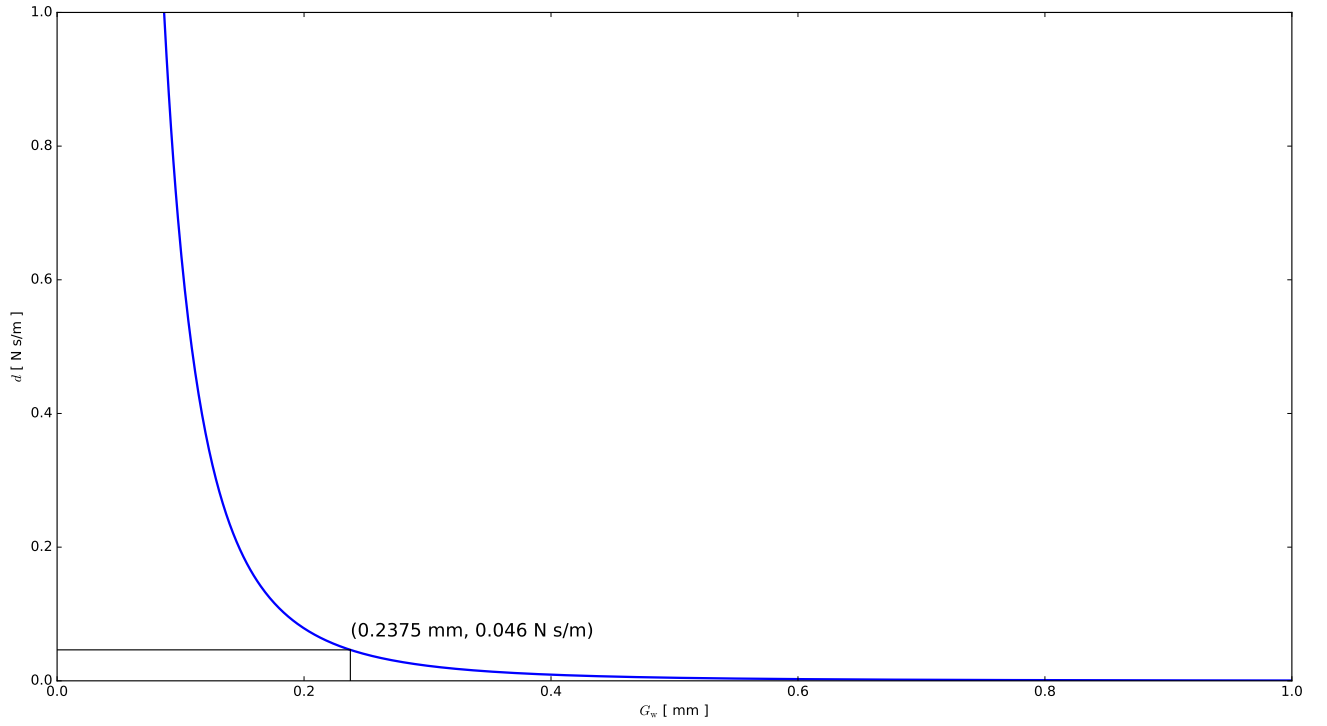


Figure 25: Viscous damping of prototypes 1 and 2 as a function of air gap

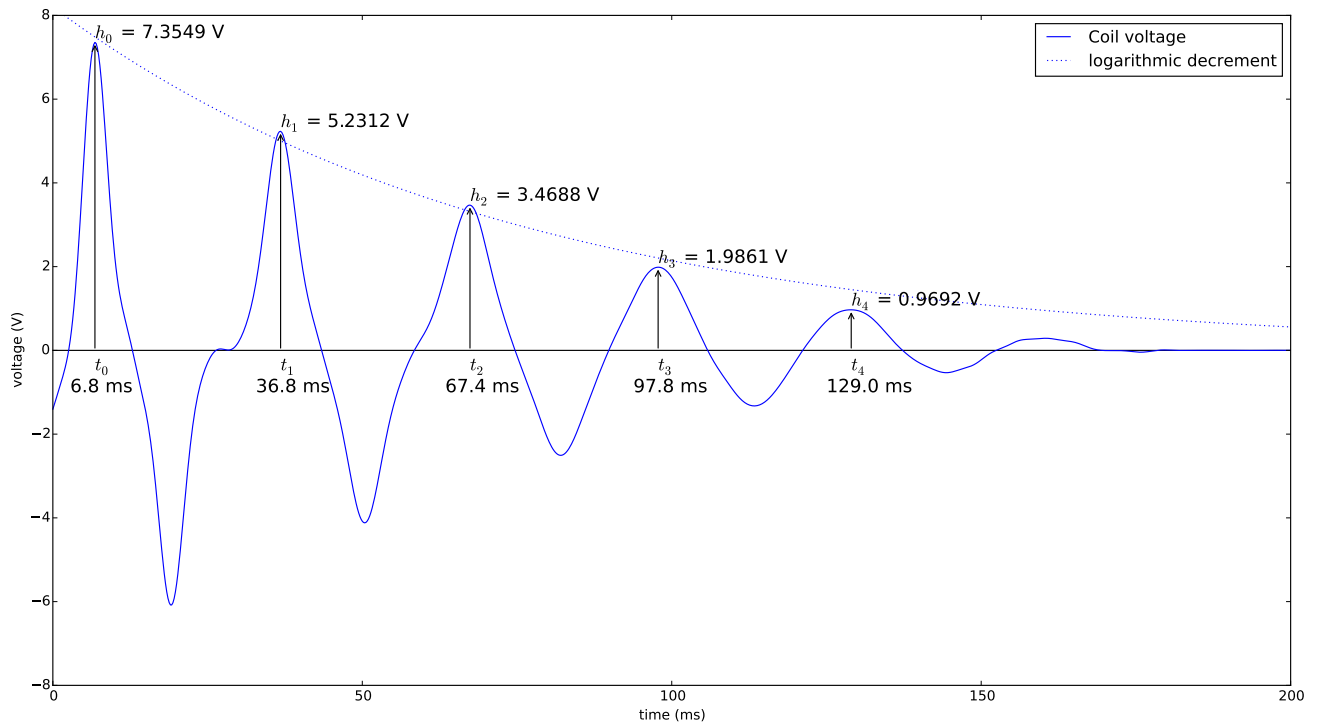


Figure 26: Damping of prototype 1

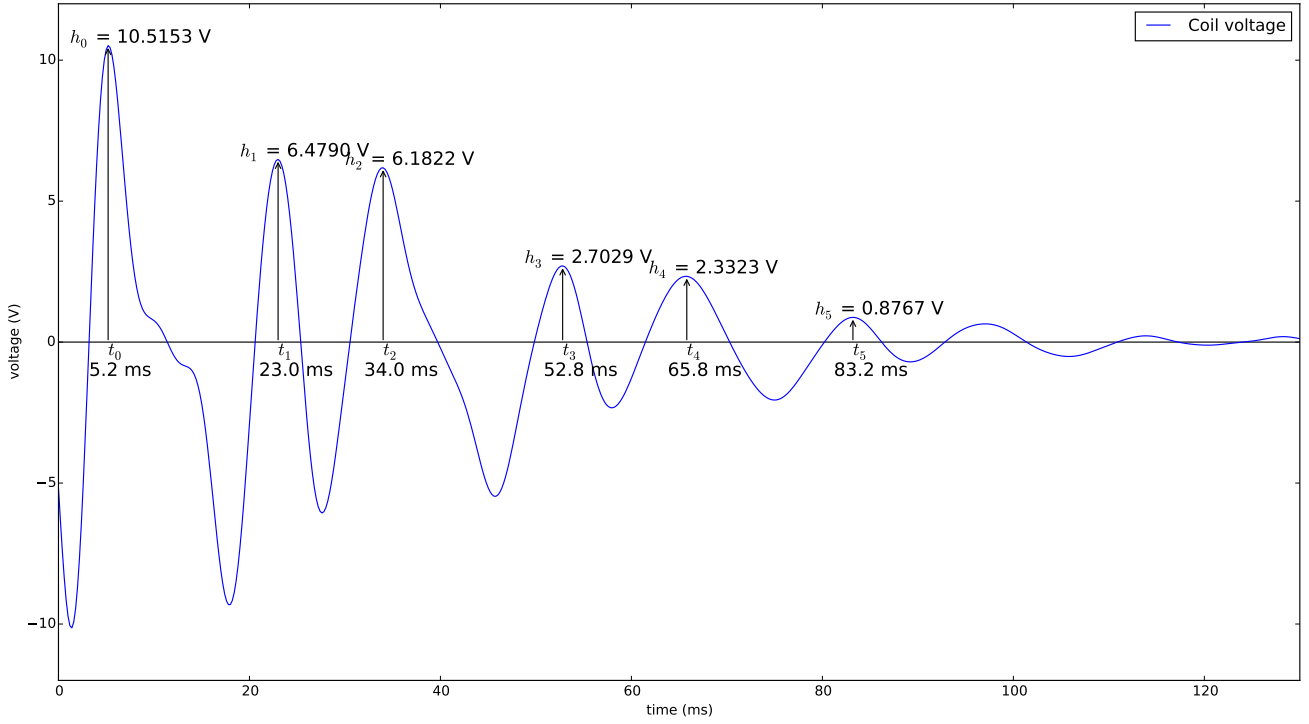


Figure 27: Damping of prototype 2

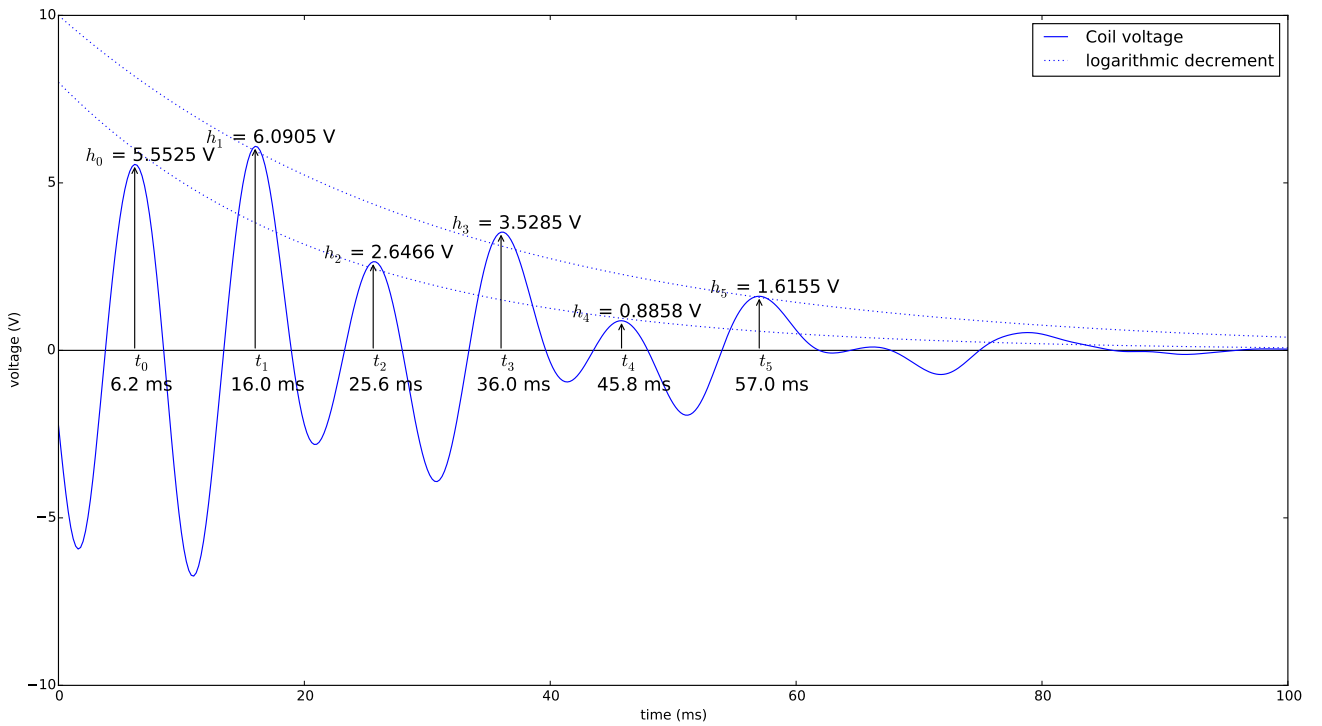


Figure 28: Damping of prototype 3



Depending on which two peaks are selected the damping coefficient can be anything from 0.23 N s/m to 0.47 N s/m. These numbers are also much higher than what the ones calculated with (21). This could mean that the viscous damping is not the only or not even the dominant source of damping. The measurement accuracy of the gap cannot explain error of this scale. One possible problem because there is nothing that keeps the magnet upright position in the middle of the tube and prevent the magnet from touching the walls. Instead there are the restoration force of the (magnet)spring which exerts torque to the magnet it starts to lean towards the walls of the tube like illustrated in Figure 29. This causes two disadvantages. First, the actual gap  $G_w$  decreases and there is a friction between the wall and the magnet. When two surfaces slice there are two types of friction coefficients; static and dynamic. The static coefficient of friction is higher than the dynamic coefficient of friction. When the amplitude of the vibration and also the velocity decreases it takes more time before the static friction is overcome and the magnet starts moving again. It could be possible that initial movement in this measurement is below the normal magnet velocity and therefore this test indicate more pessimistic values than the values when the magnet is moving by 1 g base excitation.

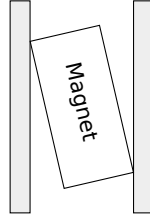


Figure 29: Tilted magnet.

It should be possible to use such a wall material that have low coefficient of friction such as Teflon, use magnets with low friction coating/plating or to use ferrofluid lubrication. Magnet aspect ratio where the magnet height is bigger than magnet radius should also reduce the force the magnet exerts to the wall and hence reduce the

Table 10: Viscous damping coefficients for prototype 1 and 2

damping	$x(t)$	$x(t + nT)$	$n$	$T$	$\delta$	$\zeta$	$d$
	V	V		ms			N s/m
$c_{0-1}$	7.3549	5.2312	1	30.00	0.3407	0.054	0.23
$c_{0-2}$	7.3549	3.4688	2	30.30	0.3758	0.060	0.25
$c_{0-3}$	7.3549	1.9861	3	30.33	0.4364	0.069	0.29
$c_{0-4}$	7.3549	0.9692	4	30.55	0.5067	0.080	0.34
$c_{1-2}$	5.2312	3.4688	1	30.60	0.4108	0.065	0.28
$c_{1-3}$	5.2312	1.9861	2	30.50	0.4842	0.077	0.33
$c_{1-4}$	5.2312	0.9692	3	30.73	0.5620	0.089	0.37
$c_{2-3}$	3.4688	1.9861	1	30.40	0.5576	0.088	0.38
$c_{2-4}$	3.4688	0.9692	2	30.80	0.6375	0.101	0.42
$c_{3-4}$	1.9861	0.9692	1	31.20	0.7174	0.113	0.47

Table 11: Viscous damping coefficients found in the literature.

Reference	$d_m$ N s/m
[26], [34], [35]	0.1
[36]	0.3
[37]	0.06
[38]	0.16 – 0.32
[39]	0.19
[40]	0.048

friction. Table 11 shows viscous damping coefficients reported in the literature. This suggests that both calculated and measured viscous damping coefficients fall within the values reported in the literature. Viscous damping coefficient  $d_m = 0.1$  N s/m is used in optimization since this value should be achievable with proper selection of materials and when  $G_w > 0.19$  mm.

### 4.3 Restoration force calculation validation

The result of the repulsion force calculation for magnets used in prototypes 1 and 2 is shown in figure 31. In order to validate the calculation results the actual repulsion force was measured using a precision scale (accuracy  $\pm 0.1$  g) and printed ruler that was attached to the tube that holds the magnets in place horizontally, see figure 30. To gain more accuracy to the distance measurement the camera was positioned perpendicular to the magnet and each position was photographed. Then the distance was measured using image analysis allowing the measurement below 1 mm accuracy for prototypes 1 and 2. Prototype 3 was more difficult to measure because the larger gap  $G_w$  allowed the magnet to be more off-center or even slightly tilted during the measurement.

Two different size of magnet pairs were measured in order to validate the force calculation algorithm. Figure 31 depicts the magnet spring using smaller magnets that are used in the prototypes 1 and 2 while the figure 32 depicts the the force between bigger magnets used in prototype 3. Each figure have two graphs; actual measurements with error bars, FEM calculation result

Figure 33 shows calculated and measured restoring force for prototypes 1 and 2. The calculated resting position  $d_{\text{rest}}$  is  $-7.88$  mm while measured was  $7.73$  mm which is within the measurement accuracy. Linearized spring constant around the resting position  $k = 18.09$  N/m which predicts  $6.7$  Hz resonance frequency. Figure 34 shows restoring force for the prototype 3 which is outside the measurement error. Displacement error of  $1.5$  mm would explain this or off-center positioning or tilting of the magnet. The calculated resting position  $d_{\text{rest}}$  is  $-2.33$  mm while measured was  $2.2$  mm which is within the measurement accuracy this suggest that the previous measurement have systematic error. Linearized spring constant at  $d_{\text{rest}}$  is  $k = 127.85$  N/m which predicts  $10.7$  Hz resonance frequency.

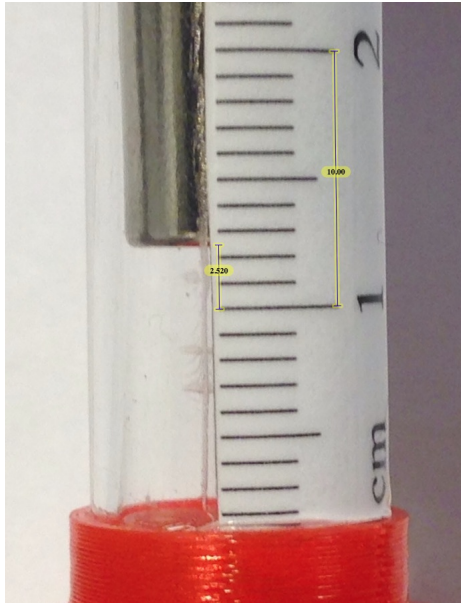


Figure 30: Distance reading in the force measurement

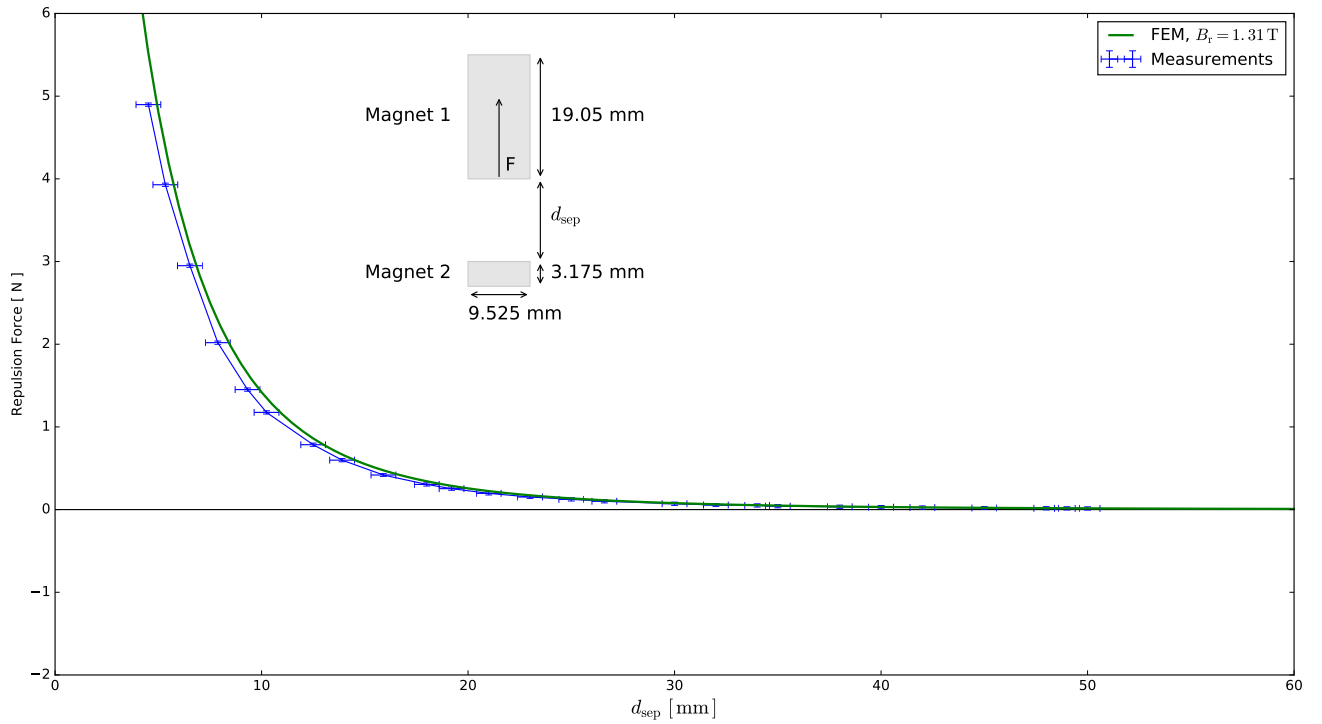


Figure 31: Magnet spring for prototypes 1 and 2

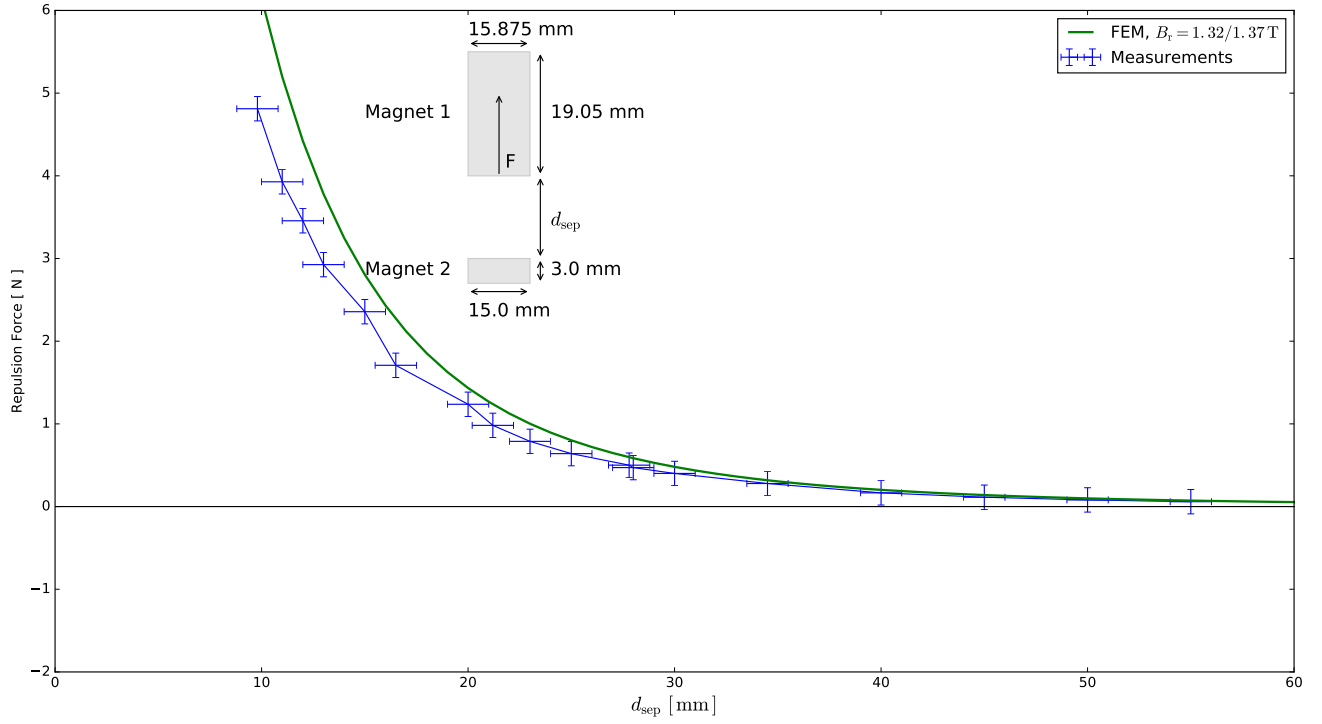


Figure 32: Magnet spring for prototype 3

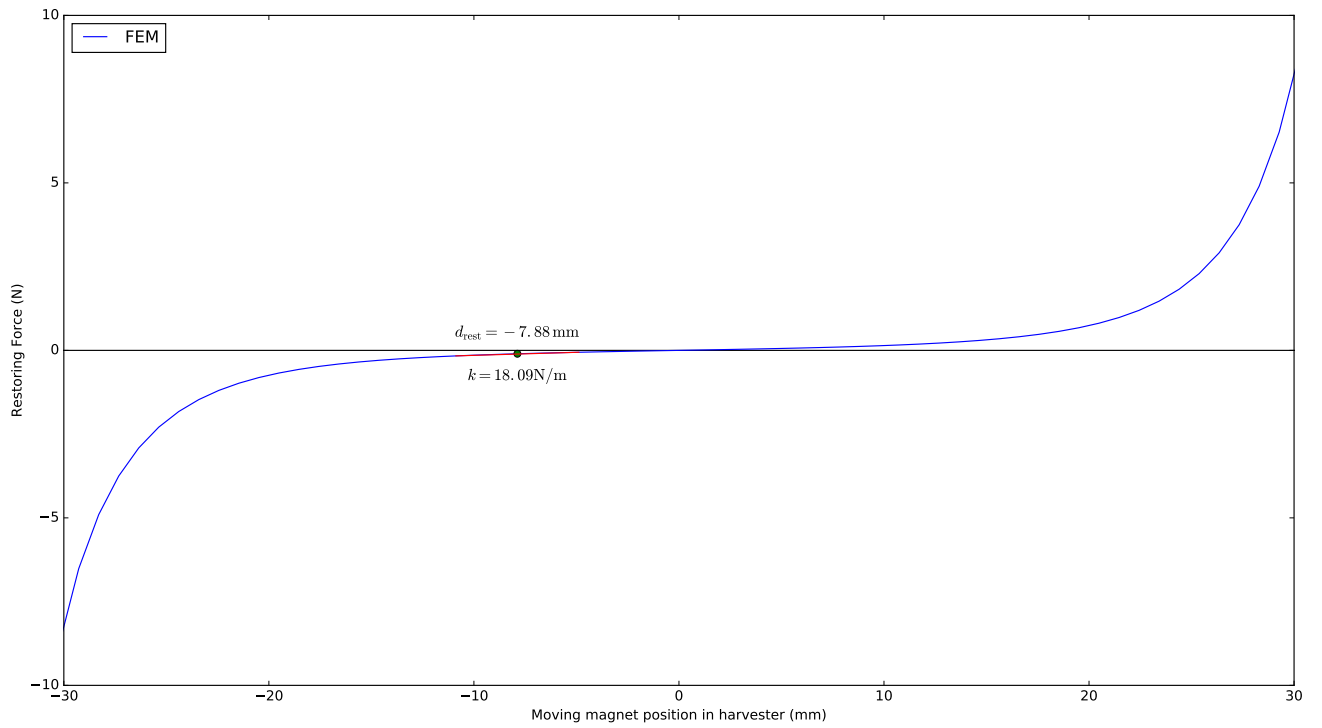


Figure 33: Restoring force for prototypes 1 and 2

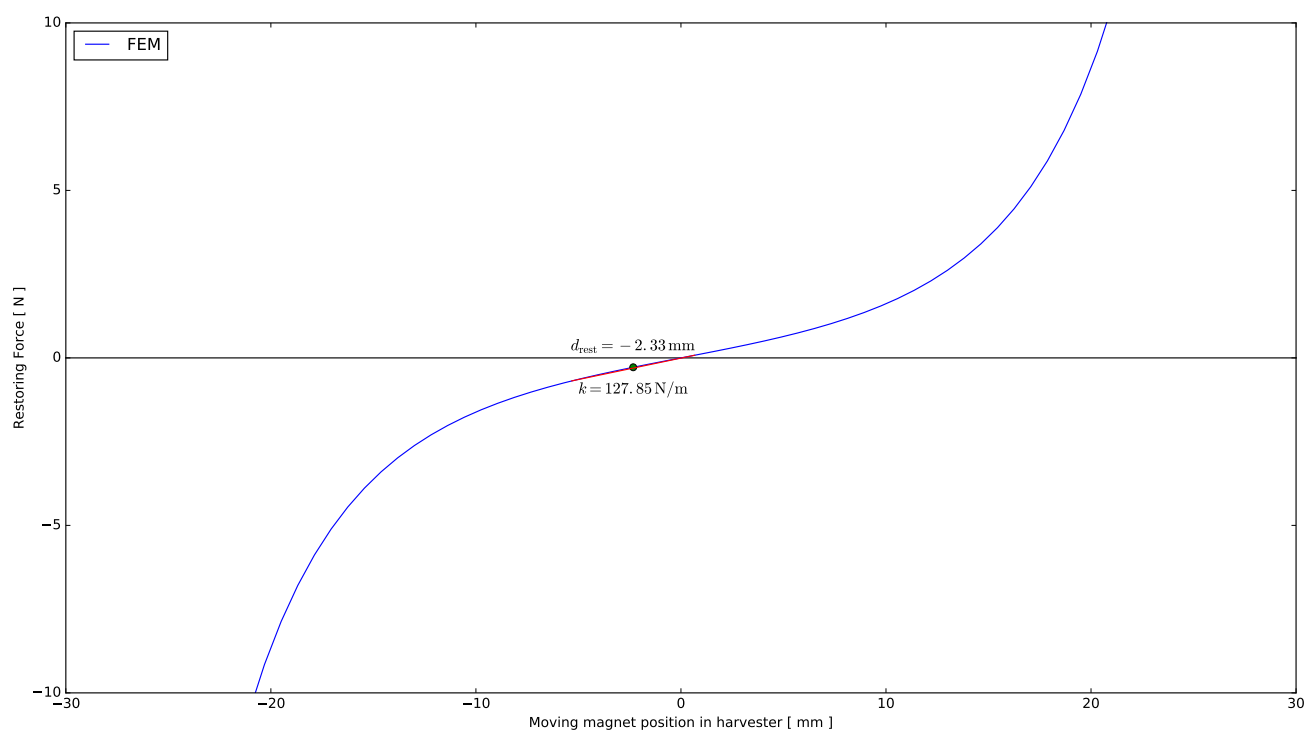


Figure 34: Restoring force for prototype 3

#### 4.4 Coil resistance validation

The purpose of this section is to validate the coil resistance equation (41) defined in 3.2.2. Three different coils were manufactured with using enamelled wires of different nominal diameters and different number of turns and then they were measured and compared against calculated values. Table 12 shows that the equation (41) have a good agreement with the measurements. There are some deviation from the actual measurement but it is due to unevenness of the outer layer of the hand-wound coil and therefore inherent measurement inaccuracy of the  $r_o$ . Another factor that could have contributed to higher resistance values is unintentional wire elongation due to uncontrolled wire tension during winding.

Table 12: Coil resistance equation validation

$d_{co}$	$N$	$r_i$	$r_o$	Eq (41)	Measurement
$\mu\text{m}$		mm	mm	$\Omega$	$\Omega$
100	3046	6.025	12.1	377	391
150	1351	6.025	12.8	77	79.4
200	800	6.025	13.0	26	26.6

#### 4.5 Flux linkage computational model validation

This section tries to validate the computational model for flux linkage. This is done by constructing several coils around acrylic tubes which outer radius will become the coils inner radius  $r_i = 6.025$  mm. Different coils are made using different coil height  $h_{coil}$ , coil outer diameter  $r_o$  and wire diameter  $d_{co}$ . Both one and two coil configurations are tested. In the two coil configuration the winding direction of the second coil is opposite of the first coil, otherwise they will cancel each other out when the magnet is between them. Also the load resistance is varied to cause different amount of electrical damping. Table 13 shows the dimensions of the coils used in the drop tests. The resistance in the table is not calculated but instead measured because the coils are hand made and the fill factor nor the wire tension cannot be controlled accurately.

Table 13: Different coils and loads used in each drop test

Drop test number	coils	$N$	$d_{co}$	$r_o$	$h_{coil}$	$R_{coil}$	$R_{load}$
			$\mu\text{m}$	mm	mm	$\Omega$	$\Omega$
1	1	500	200	8.15	12.1	12.69	75
2	1	500	200	8.15	12.1	12.69	13.7
3	1	1351	150	12.80	6.2	26.65	1M
4	2	3000	100	12.90	6.0	783	1M
5	2	3000	100	12.90	6.0	783	783

The same magnet with dimensions  $h_{mag} = 19.05$  mm and  $r_{mag} = 4.7625$  mm are used in all drop tests. Residua flux density of the N42 neodymium magnet is assumed

to be the nominal value specified by the manufacturer which is 1.31 T. The acrylic tube is positioned vertically and the the magnet is held inside the tube so that it does not touch the tube walls from any side before it is dropped. The dropping distance is 200 mm and it is measured from the middle of the magnet to the middle of the coil or to the middle of the first coil in case where there are two coils in series.

In this experiment the parasitic viscous damping is assumed to be zero since the friction from either air or the walls of the tube is insignificant and there is no compressed air since both end of the tube are open. In a free fall the magnet accelerates due to gravity and therefore the position and velocity of the magnet is easy to solve in ordinary differential equation (ODE) solver. ODE solver only needs a starting values and a function that returns derivatives of those values. Such a function is implemented in Python and the source code is shown in listing 1.

Figure 35, Figure 36 and Figure 37 shows the magnet displacement, velocity, acceleration, flux linkage, time derivative of the flux linkage and the voltage over the load resistor as a function of time. Figure 38 and Figure 39 shows the same plots for configuration where two coils are connected in series. Plots in the figures are zoomed to show time between 175 ms and 230 ms because that is the time window when the magnet approaches and passes through the coil(s). All parameters plotted in blue are calculated and the output voltage plotted in red is measured. Only the output voltage is measured since I had no measurement equipment available to measure the intermediate values. The time offset is adjusted by setting the maximum value of calculated and measured voltage to the same point in the x-axis. Figures demonstrates how closely this flux linkage calculation procedure agrees with measurements. This suggest that if the position and speed of the moving magnet is known then the output voltage and power can be calculated accurately.

```

1 def falling(state, t, m_Br, h_m, r_mag, h_coil, r_i, r_o, N, d_co, res, m, b):
2     g = 9.819 # gravity in Helsinki
3
4     x = state[0] # displacement
5     xd = state[1] # velocity
6
7     # calculate transduction factor (partial derivative of magnetic flux with
8     # respect to x)
9     fluxdx = calc_flux_gradient(m_Br, h_m, r_mag, h_coil, r_i, r_o, N, d_co, x)
10    # compute acceleration xdd
11    xdd = -g - b * xd / m - fluxdx * fluxdx / res * xd / m
12    # time derivative of the magnetic flux is transduction factor times velocity
13    fluxdt = fluxdx * xd
14
15    # return all state derivatives
16    return [xd, xdd, fluxdt]

```

Listing 1: Python code for derivatives.

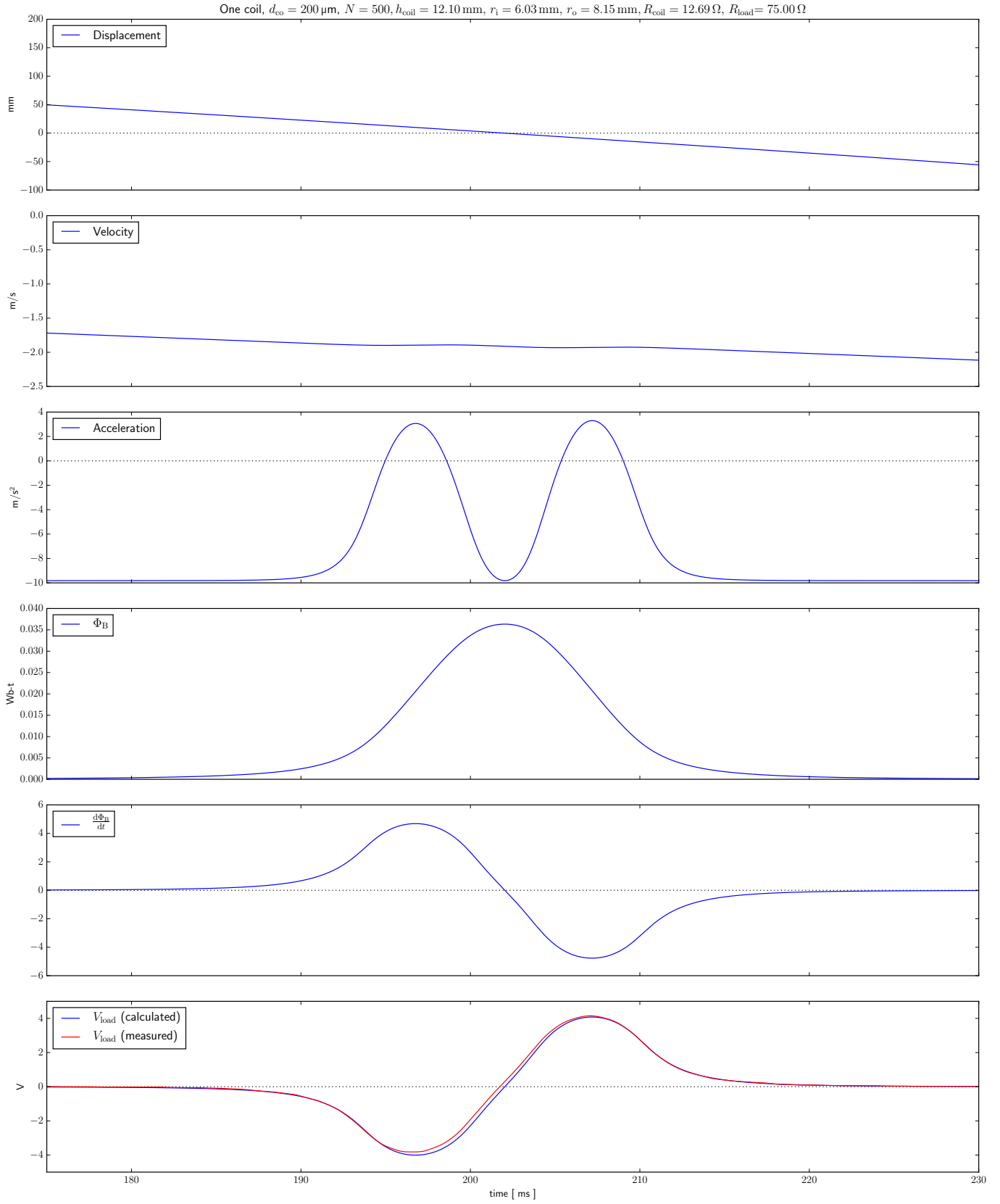


Figure 35: Magnet drop test through a coil, drop test number 1.



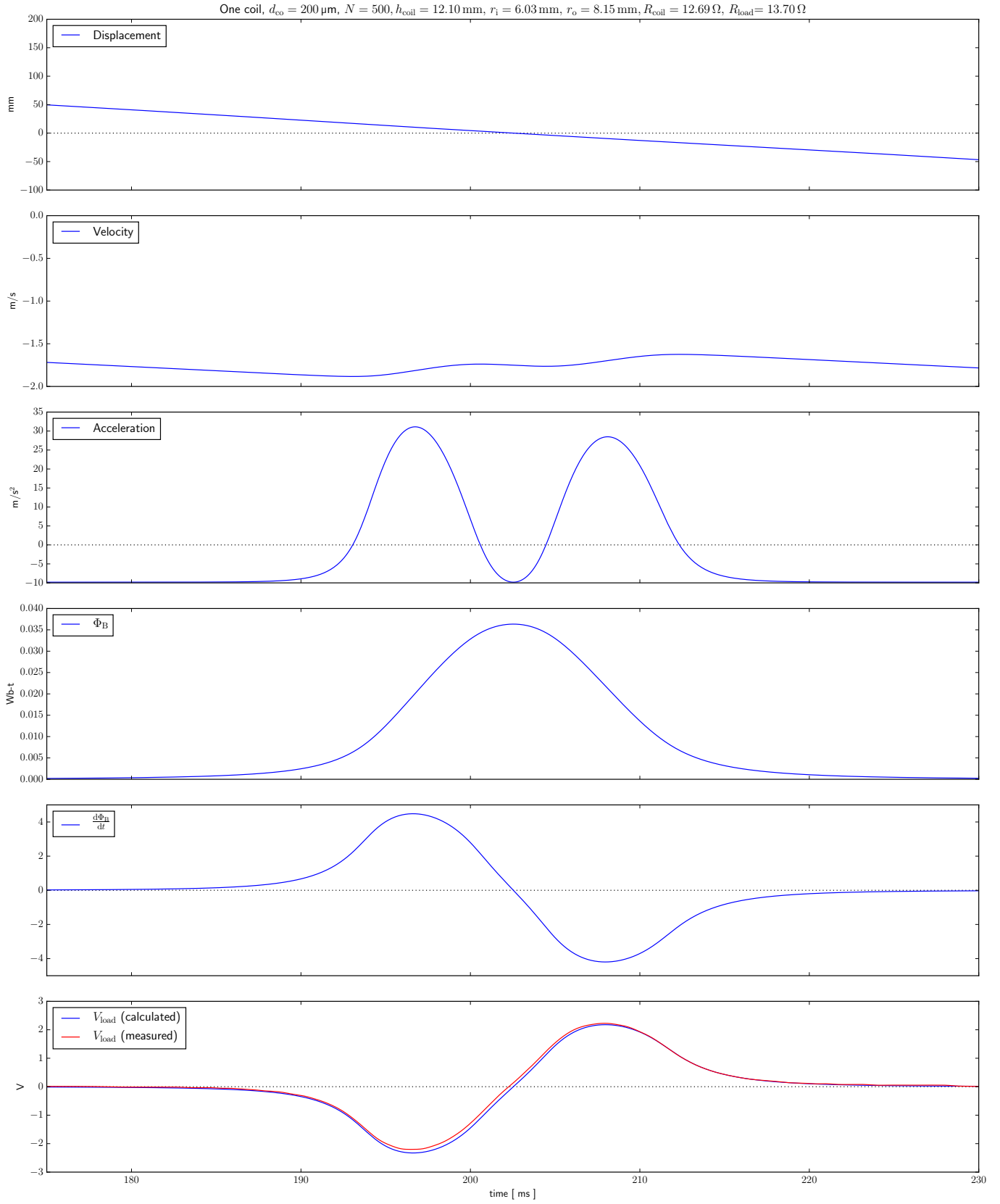


Figure 36: Magnet drop test through a coil, drop test number 2.

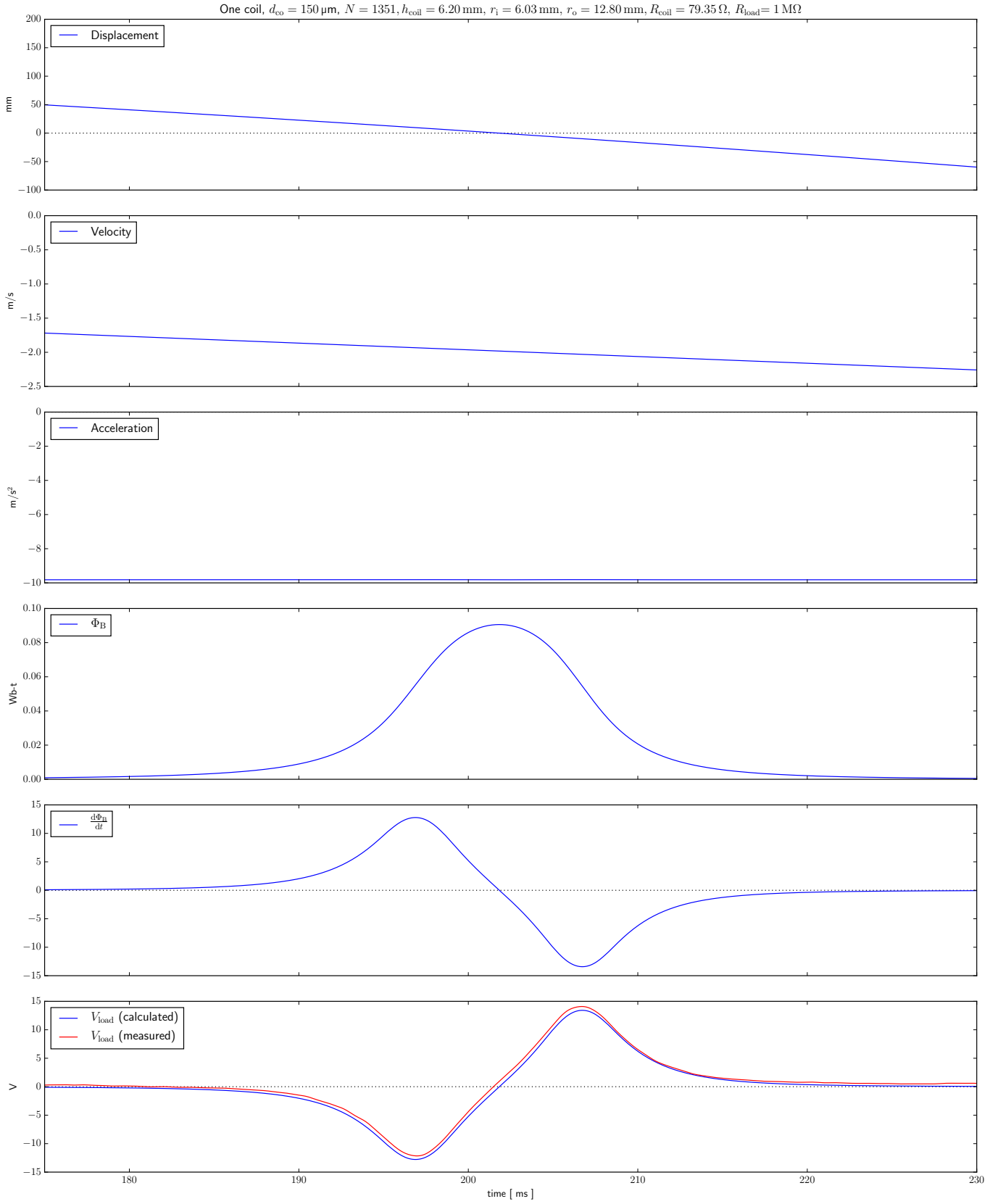


Figure 37: Magnet drop test through a coil, drop test number 3.

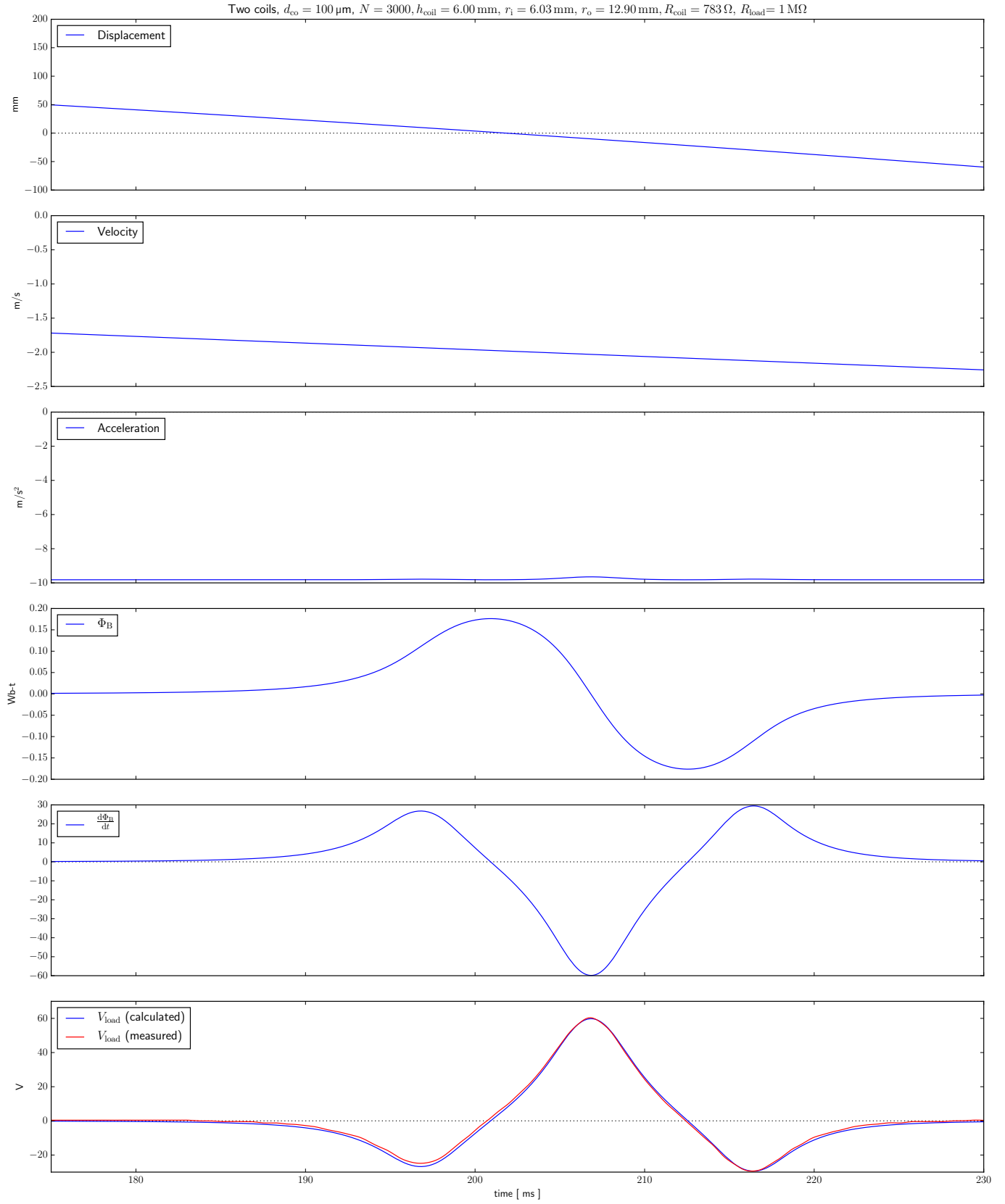


Figure 38: Magnet drop test through a coil, drop test number 4.

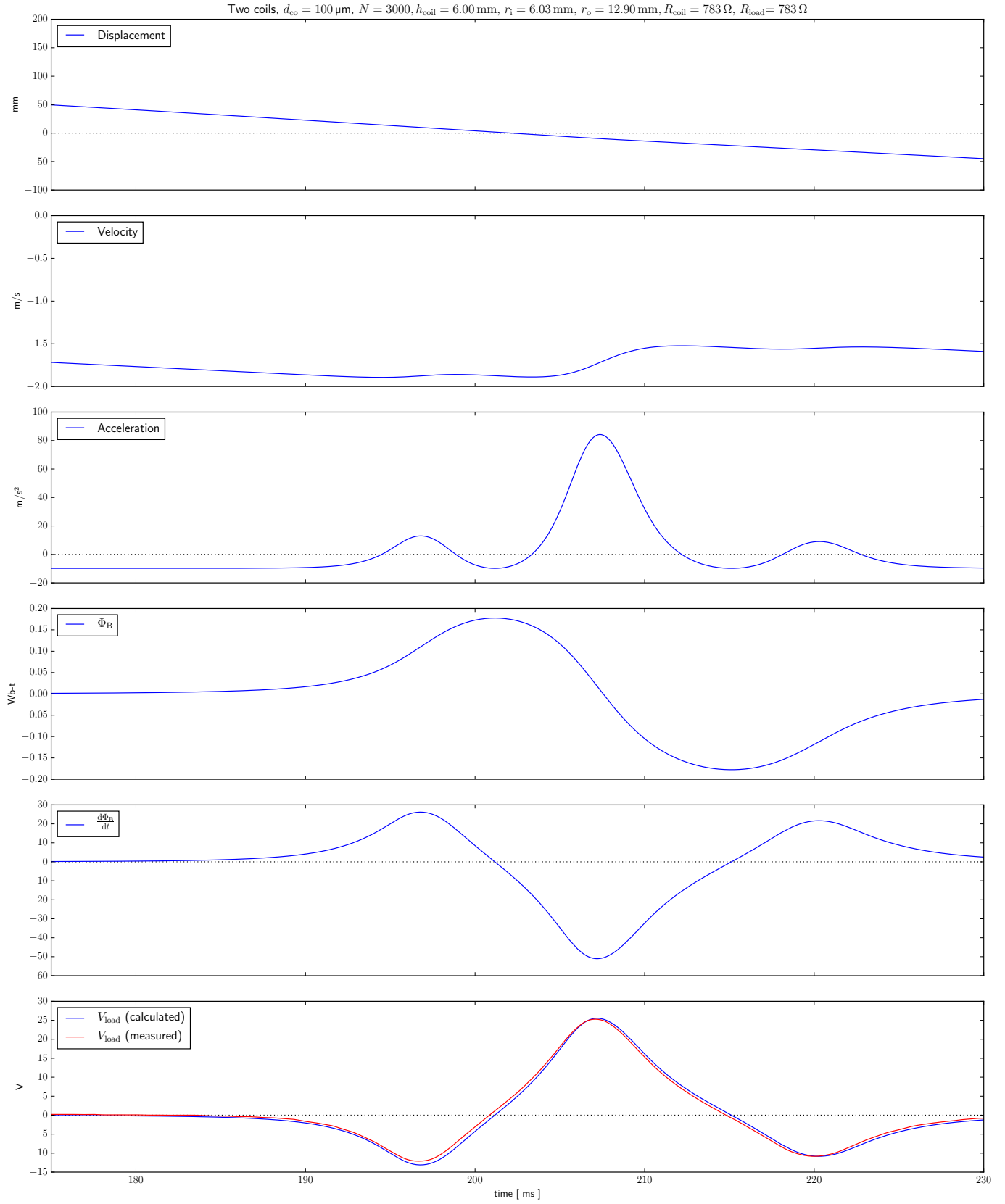


Figure 39: Magnet drop test through a coil, drop test number 5.

## 4.6 Power calculation validation

This section tries to validate the power calculation of one coil configuration against values from the literature. Spreeman have calculated optimal dimensions for such an harvester in [34], [35] and [26]. All those optimize harvester for  $1 \text{ cm}^3$  construction volume and they all have fixed the coil outer radius to  $r_o = 6 \text{ mm}$ . However there seems to be some variation in reported maximum construction heights between these studies. The maximum construction height  $h$  was reported to be  $9 \text{ mm}$  in [35] and  $8.9 \text{ mm}$  in [26]. Theoretical value of height for  $1 \text{ cm}^3$  construction volume should be

$$h = \frac{V_{\max}}{\pi \cdot r_o^2} = \frac{1 \text{ cm}^3}{\pi \cdot (6 \text{ mm})^2} \approx 8.84 \text{ mm}. \quad (93)$$

Figure 40 shows parameter sweep for  $r_i$  and  $h_{\text{coil}}$  while keeping all other parameters constant and exactly the same as described in [26] because this is the latest and most comprehensive of those three. These fixed parameters are shown in Table 14. The Figure 40 is very similar to one presented in [26] even though the values are hard to decode from the grayscale contour maps in [26]. Plots show that the transconductance maximum ( $k_{\max}$ ), output voltage maximum ( $V_{\max}$ ) and output power maximum ( $P_{\max}$ ) are all in different point in the search space. Numerical values from [26] as well as two dimensional search with fixed  $t_0/h_{\text{coil}}$  are shown in Table 15 for both one coil configuration. Values are in a good agreement with the values reported in [26] but they are not exactly the same. The difference could be due to approximations made in [26]. There they calculated the magnetic flux density to group of coil turns to save processing time while here, the flux density is calculated to each single turn separately. This approach also uses smaller discretization steps along the radius because the computational power is not such an issue with modern computers.

Table 14: Fixed parameters in one coil configuration

Parameter	Description	Value
$V$	construction volume	$1 \text{ cm}^3$
$h$	construction height	$8.9 \text{ mm}$
$r_o$	coil outer radius	$6 \text{ mm}$
$G_c$	gap between coil and magnet	$0.5 \text{ mm}$
$B_r$	residual flux density	$1.1 \text{ T}$
$\rho_{\text{mag}}$	magnet density	$7.6 \text{ g/cm}^3$
$k_{\text{co}}$	copper fill factor	$0.6$
$d_{\text{co}}$	wire diameter	$40 \mu\text{m}$
$R'$	resistance per unit length	$13.6 \Omega/\text{m}$
$\ddot{Y}$	excitation amplitude	$10 \text{ m/s}^2$
$f$	excitation frequency	$100 \text{ Hz}$
$d_m$	parasitic damping	$0.1 \text{ N/m/s}$

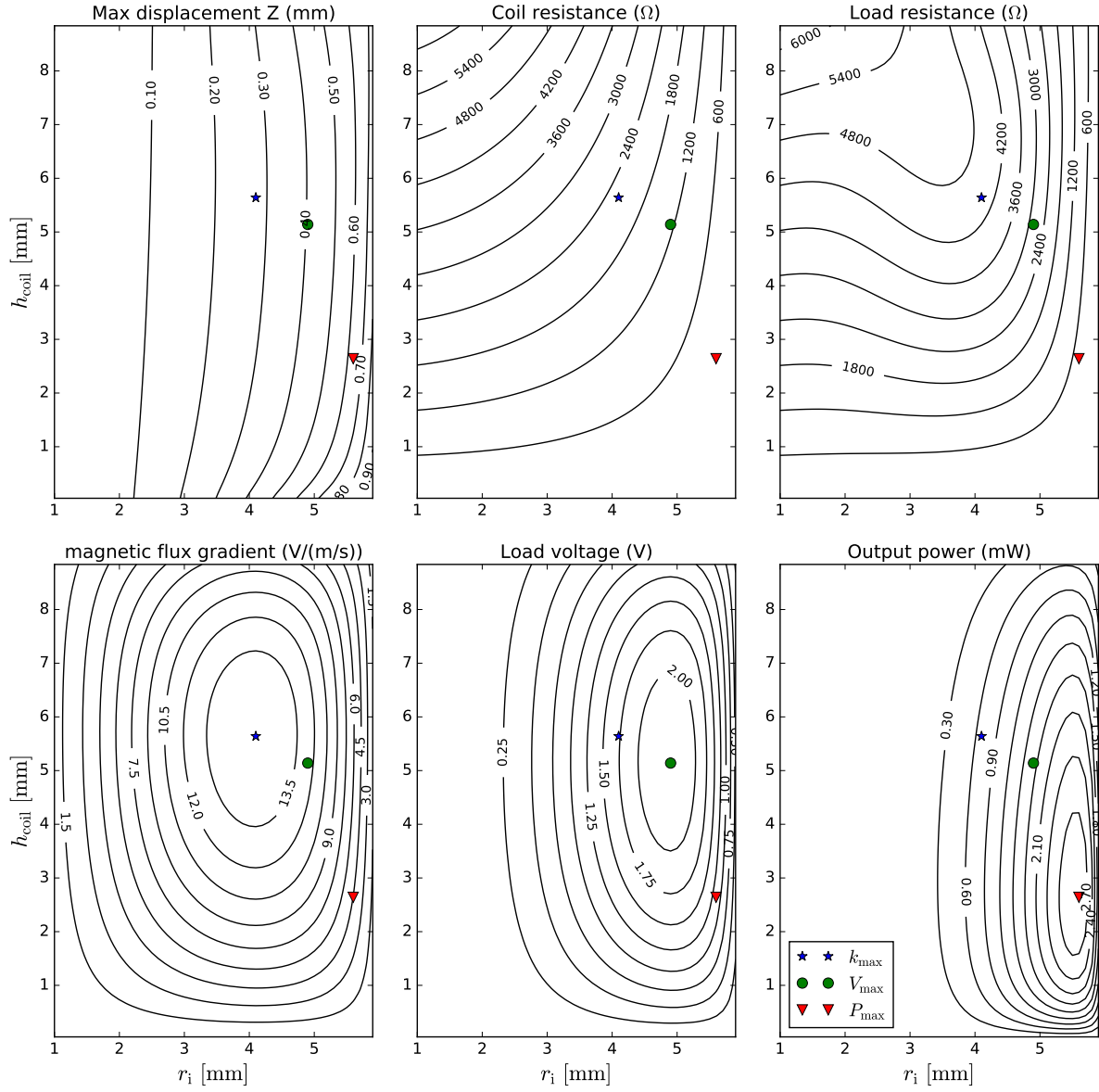


Figure 40: 2D search space for one coil harvester where  $r_0 = 6$  mm and  $h = 8.9$  mm

Table 15: Optimization result comparison

Method	$P_{load,max}$	$V_{load}$	$r_i$	$h_{coil}$	$h_{mag}/h$	$t_0/h_{coil}$
	mW	V	mm	mm		
Optimization [26]	2.94	1.47	5.41	2.53	0.92	0.75
2D search	2.93	1.26	5.55	2.74	0.923	0.75
2D search	2.94	1.25	5.55	2.74	0.938	0.797

## 4.7 Testing prototypes with a shaker

Figure 41 shows the logical representation of the vibration test setup and Figure 42 shows the fixing of the harvester to the exciter head. Accelerometer with blue wire is fixed to the harvester fixing mechanics with a straining gage cement (Kyowa CC-33A). There is a laptop that is connected to signal generator and oscilloscope via Ethernet. Signal generator is connected to a power amplifier that drives the vibration exciter. One oscilloscope channel is connected over the load resistor which is connected between harvester coil wires. The other oscilloscope channels is connected to the sensor power/coupler which biases the piezoelectric acceleration sensor and conditions it to measurement instrument. The vibrator system does not have any feedback loop which means that the controlling of the vibration generator is an open loop control. Therefore before any actual measurement can start the response of the system needs to be characterized and proper correction coefficient derived to ensure flat amplitude response over the measurement bandwidth. Figure 43 presents the compensation curve that were applied to achieve flat 1 g amplitude response from 6 Hz to 100 Hz. It should be noted that the vibration accelerations cannot be set to more than 0.2 g with this measurement setup because the feedback signal is weak and noisy. While the performance measurements were made at 1 g vibration amplitudes other amplitudes were tested also. Vibration tests confirmed the hypothesis about the wall friction. With small acceleration levels the the force exerted to the magnet did not exceed the threshold level for magnet to start moving and the output of the harvester remained at 0 V. After the threshold level was exceeded the output power was roughly proportional to the base excitation vibration acceleration squared.

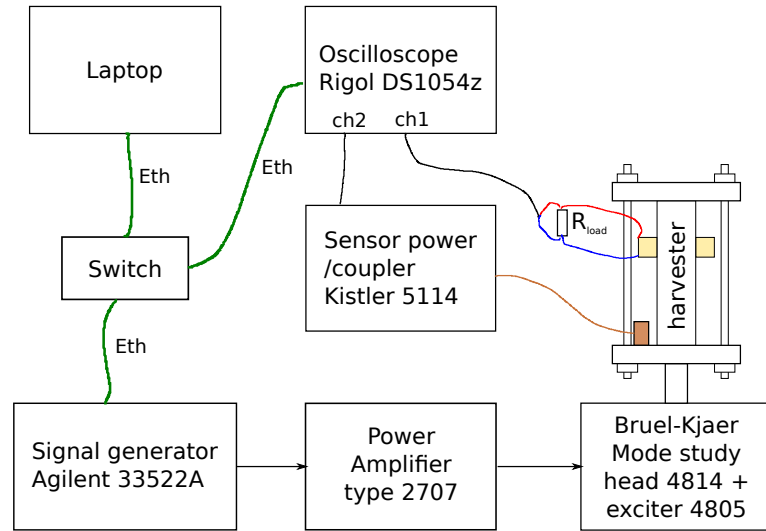


Figure 41: Vibrator test setup.

One Python script (*vibrate.py*) was created that controlled the vibrator and collected the data and then saved the raw data to the *.csv* file. This script could be run with parameters that define which frequency ranges will be measured with 10 Hz, 1 Hz, 0.1 Hz and 0.01 Hz increments and it is possible to omit the denser increments.

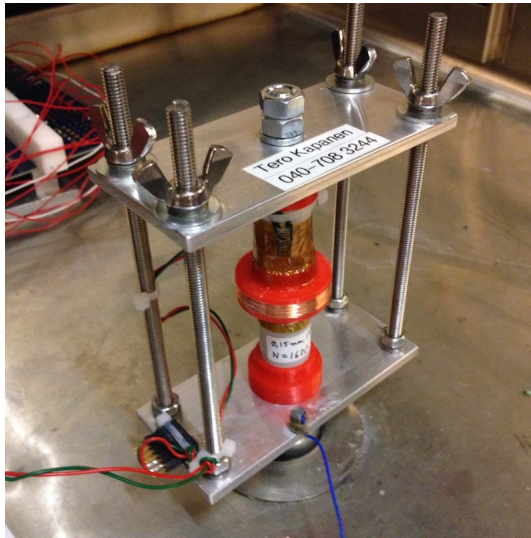


Figure 42: Mechanical fixing of harvester to vibrator.

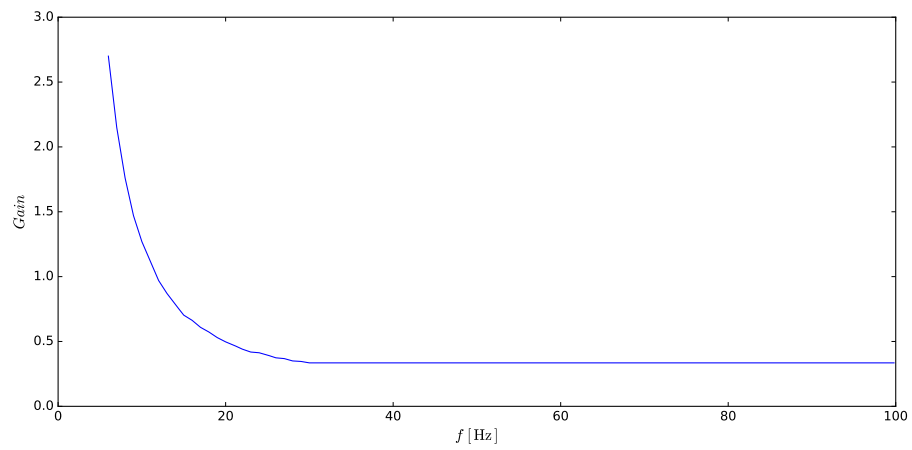


Figure 43: Vibrator compensation curve for flat 1 g amplitude response.



The idea is to run this script ones with coarse increments to determine the location of resonance frequency of the harvester and then run the actual test sweeps with smaller increments around the resonance frequency. The script starts by initializing the signal generator and the oscilloscope. For each tested frequency the script sets the appropriate time/div to the oscilloscope, sets the output frequency and compensated output amplitude to the signal generator. Then it waits two seconds for the output to stabilize and makes first preliminary measurement. If the input signal is clipped or the amplitude of the signal is too low it changes the volts/div setting as long as either the optimal volts/div setting is found or the minimum/maximum setting is set. After that the values for channel 1 and channel 2 is read from the oscilloscope and saved to the *.csv* file. The same is repeated for all frequencies and when the stop frequency is reached the script starts the frequency sweep in reverse order. This is done to see if the direction of the frequency sweep affects to the results.

Other Python scripts are used to analyze and visualize the data. One post-processing script *make\_meas.py* filters the data using 12<sup>th</sup> order low-pass filter with corner frequency of 70 Hz to remove unwanted noise from the measurement. The type of the filter is Chebyshev type II because it has no ripple on the pass-band and its transition to the stop band is sharper than with Butterworth. After filtering three consecutive zero crossings are searched from the accelerometer data. The data between the first and the third zero crossing constitutes the date of one cycle time. Since the other oscilloscope channel measures simultaneously this allows indexing the harvester output over exactly one cycle. The root-mean-square is calculated over the samples of one cycle and the value along with the frequency is stored in other file (*sweep\_137R\_20160816\_1654.csv*) which starts with *sweep\_* and contains output load resistance value, date and time. This is then repeated to all measured frequencies. This allows measuring the same harvester with different output loads all generating their own file. Python script *draw\_response.py* read all files that starts with *sweep\_* and generates voltage and output power plots as a function of frequency. Such plots for prototype 1 is shown in Figure 44, for prototype 2 in Figure 47, for prototype 3 in Figure 49.

Other python script (*make\_plots.py*) is used to analyse the measured data at specific frequencies. This script shows the raw data as well as filtered data both in frequency domain and in time domain. Before doing FFT the input data is windowed using Blackman window [41]

$$w[n] = 0.42 + 0.2 \cos\left(\frac{2\pi n}{2M+1}\right) + 0.08 \cos\left(\frac{4\pi n}{2M+1}\right), \quad -M \leq n \leq M \quad (94)$$

to remove discontinuations both at the beginning and at the end of the sampled signal. In the time domain graph the root-mean-square value of the voltage over load is calculated and highlighted in the plot. Such plots for prototype 1 is presented in Figure 45, for prototype 2 in Figure 48 and for prototype 3 in Figure 50.

The predicted resonance frequency for prototypes 1 and 2 was 6.7 Hz while the measured resonance frequency was around 7 Hz. Figures 44 and 47 shows that the resonance frequency shifts to higher frequencies with higher output resistances due to non-linearity of the spring with large displacements. This is in line with results

reported in [39]. However, when the load resistance is lower and hence the electrical damping is higher the displacement of the magnet is reduced to the region of the magnetic spring where it behaves more linearly and hence the linearized spring coefficient results accurate enough approximation for resonance frequency prediction. Base excitation acceleration of  $\ddot{Y} = 1 \text{ g}$  means that the displacement  $Y = 5.1 \text{ mm}$  which is in the same order of magnitude with the coil height  $h_{\text{coil}}$ . This means that the displacement of the moving magnet is so large that the transconductance factor  $k_t$  cannot be taken as constant. This poses a limitation at low frequencies to the power calculation algorithm defined in section 3.2. However, if the base excitation frequency is 50 Hz then the same  $\ddot{Y} = 1 \text{ g}$  results to less than  $100 \mu\text{m}$  base excitation displacement and the algorithm should be more accurate. Output power calculation predicts  $P_{\text{max}} = 11.35 \text{ mW}$  while dynamic simulation predicts  $P_{\text{rms}} = 5.53 \text{ mW}$  and the measured output power is  $P_{\text{rms}} = 7.78 \text{ mW}$  at parasitic damping  $d_m = 0.1 \text{ N s/m}$ .

The predicted resonance frequency of the prototype 3 was 10.7 Hz while the measured resonance frequency was 11.3 Hz. Figure 49 shows the same shift to the higher frequency with high load impedance. It also shows other phenomena that is characteristic to the nonlinear springs [39], it has two possible states in which it can be and the state depends on the direction of the frequency sweep. In other words the current state depends on the previous state. When the excitation frequency is increasing it stays at the high output voltage state with higher frequencies than when the frequency of excitation is decreasing. This effect is reduced significantly when the electrical damping is higher and the magnet displacement remains in the approximately linear region of the magnetic spring.

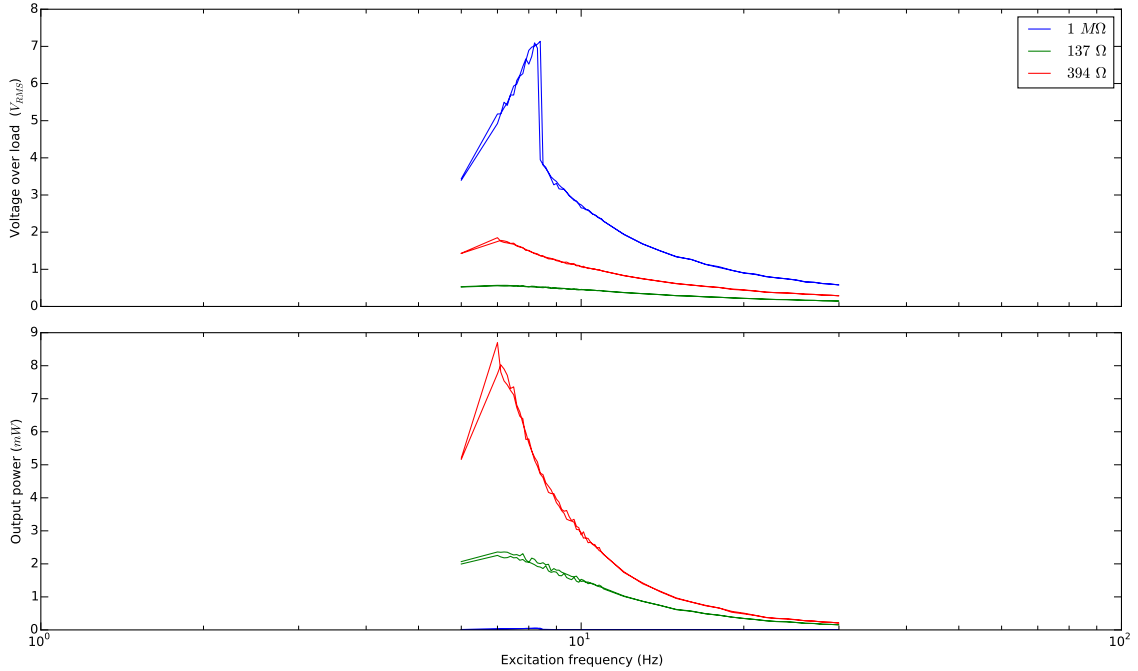


Figure 44: Frequency response of the prototype 1.

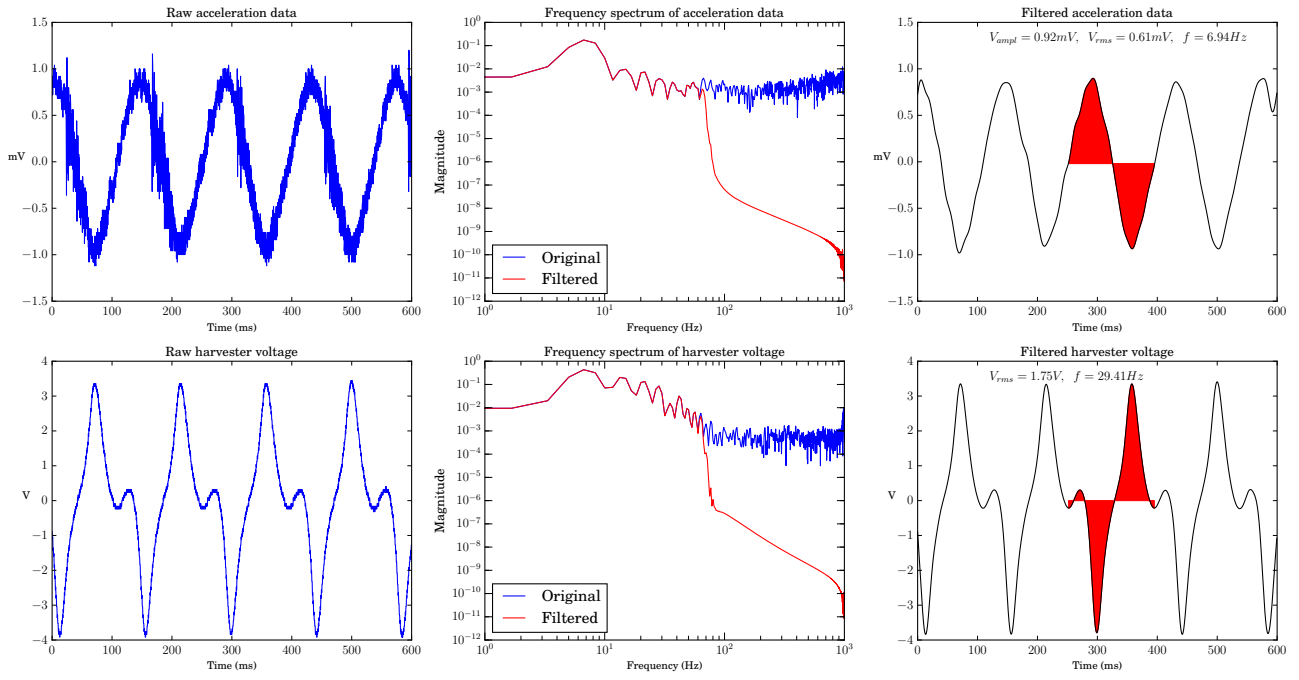


Figure 45: Prototype 1, harvester output at 7 Hz to  $R_{\text{load}} = 394 \Omega$ .

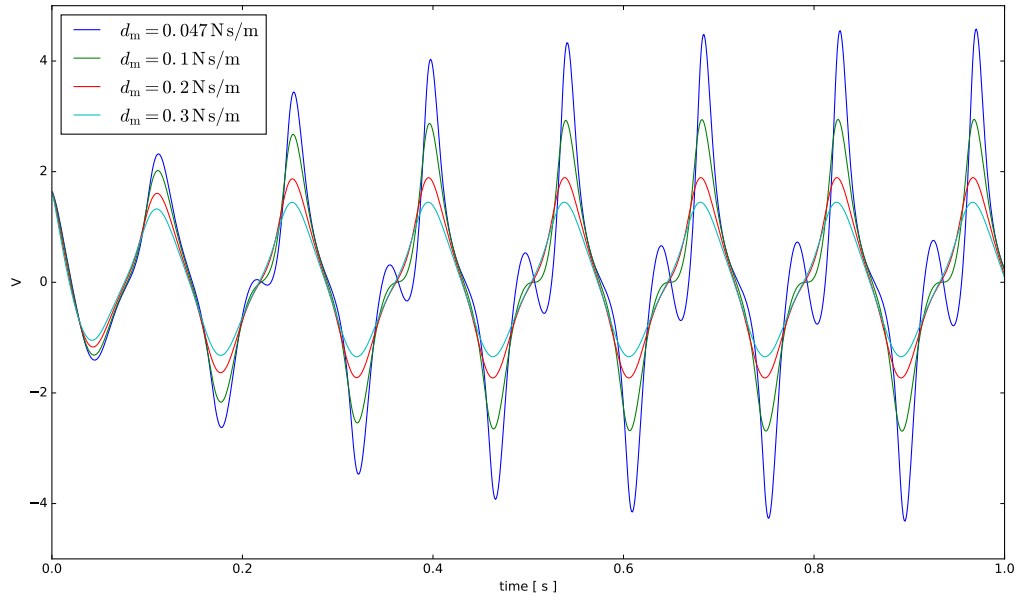


Figure 46: Prototype 1 simulated output voltage over  $R_{\text{load}} = 394 \Omega$  with 1 g base excitation at 7 Hz.

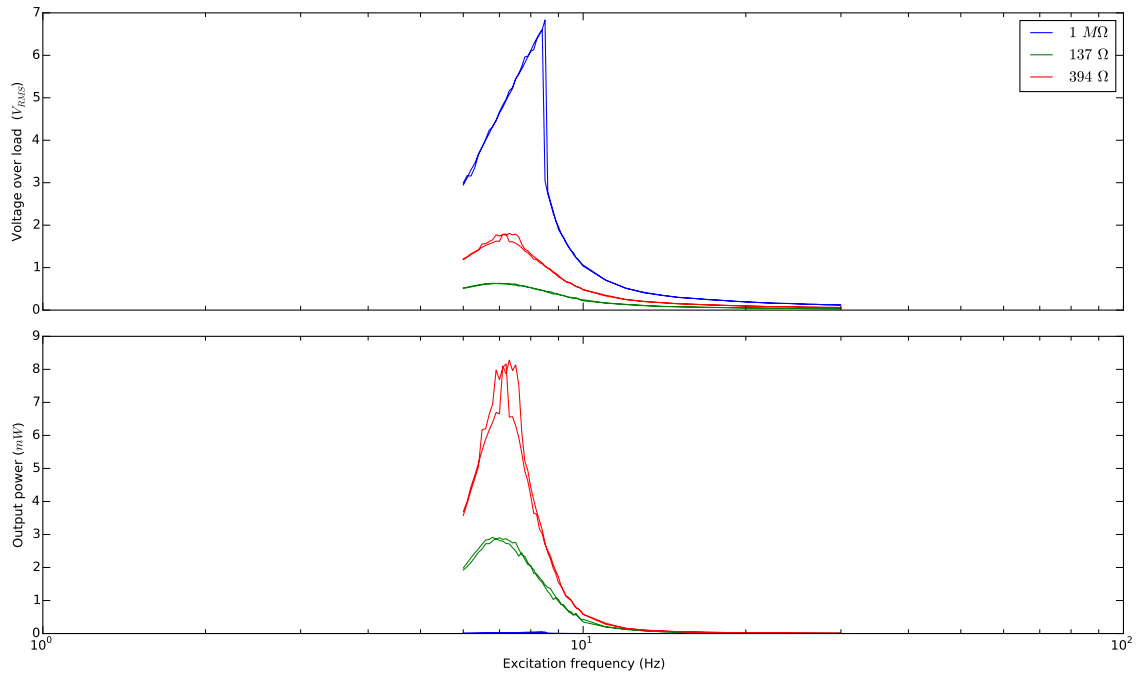


Figure 47: Frequency response of the prototype 2.

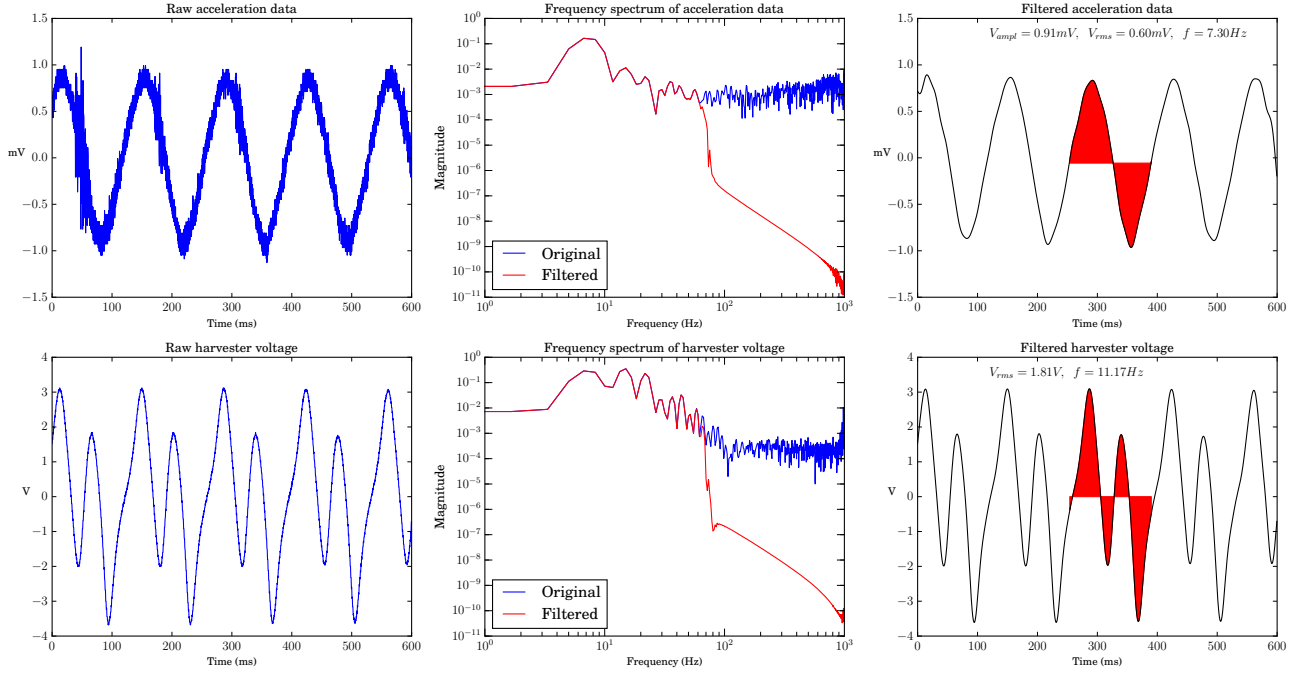


Figure 48: Prototype 2, harvester output at 7.3 Hz to  $R_{\text{load}} = 394 \Omega$ .

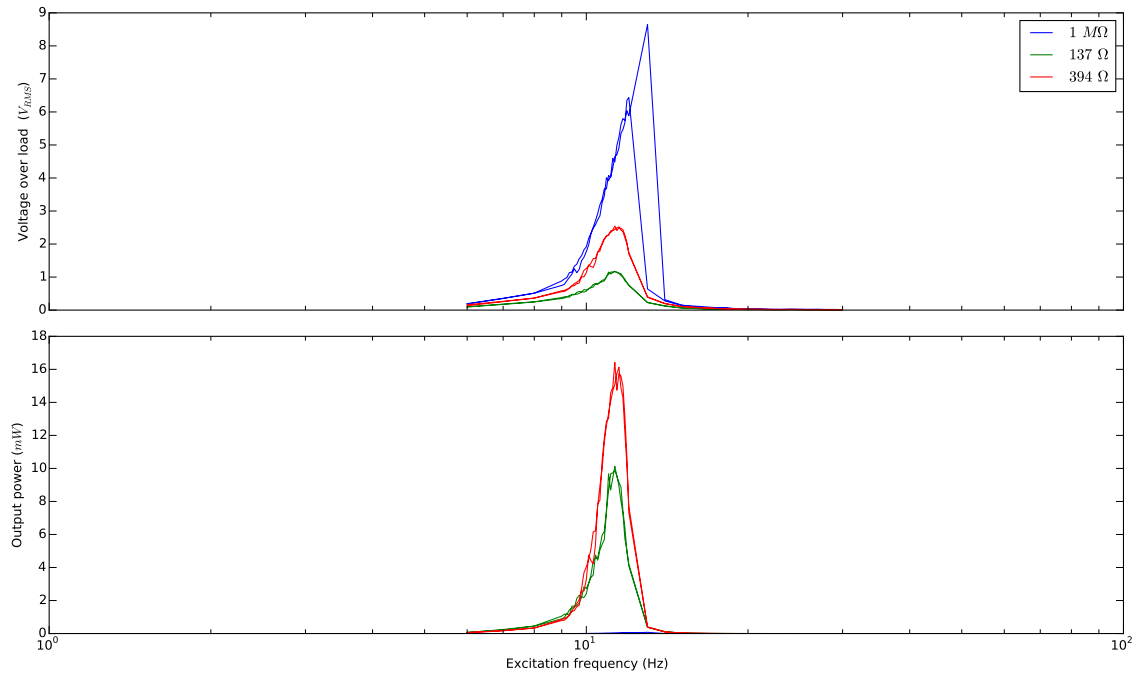
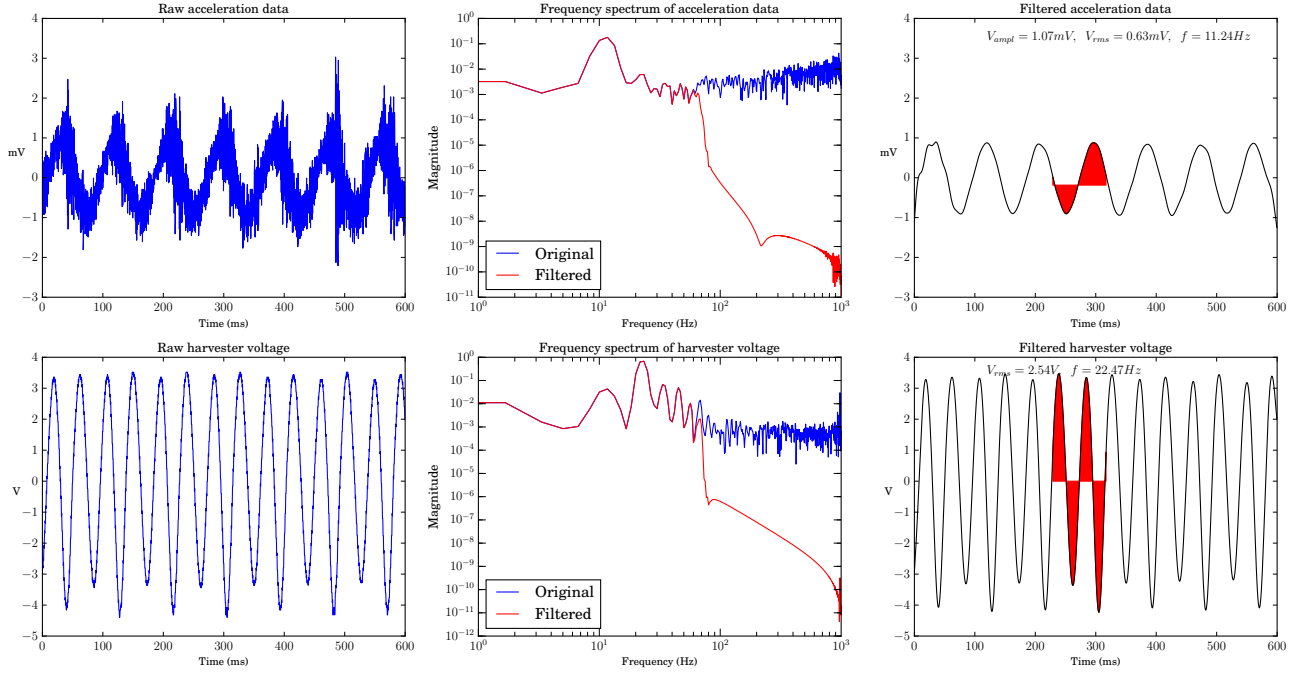


Figure 49: Frequency response of the prototype 3.

Figure 50: Prototype 3, harvester output at 11.3 Hz to  $R_{load} = 394 \Omega$ .

## 5 Parameter optimization

This chapter solves different optimization problems and identifies how different parameters affect to the output power and voltage using the power calculation defined earlier. Each optimization evaluates both one and two coil configurations and compares them against each other. First, Section 5.1 tries to find optimal dimension for harvester with  $1 \text{ cm}^3$  construction volume. Section 5.2 evaluates the effect of  $k_{\text{co}}$ , Section 5.3 effect of  $d_{\text{co}}$ , Section 5.4 the effect of construction volume size, Section 5.5 the effect of shape of the construction volume, Section 5.6 the effect of  $B_r$  to the harvester performance. Finally, Section 5.7 tries to find optimal coil dimensions for predefined magnet size.

### 5.1 Constrained construction volume and fixed aspect ratio

In this optimization approach the construction volume is constrained and also the aspect ratio is fixed. In other words, the maximum construction height  $h = 8.9 \text{ mm}$  and coil outer radius  $r_o = 6 \text{ mm}$  are fixed. Since the purpose of this optimization is to only find optimal values for coil height ( $h_{\text{coil}}$ ), coil inner radius ( $r_i$ ) and magnet resting position ( $t_0$ ), other parameters are also fixed and their effect on the maximum output power is analyzed in the subsequent sections. The fixed parameters can be seen from Table 14 in Section 4.6.

Genetic Algorithms (GA) are the type of optimization algorithms that tries to mimic the evolution found in nature [42]. The population is composed of individuals whose parameters are coded as genotypes, the individuals then mates with each other producing offspring that share the genes of their parents added with some random mutation. The fitness is calculated to all individual and then individuals are selected to the next generation depending on their fitness. This survival of the fittest causes the hill climbing behavior of the optimization algorithm. Evolutionary algorithms have two selection mechanisms. One for selection of parents and other for selection of survivors. If those two selections overlap it causes “greediness” to the algorithm and therefore the algorithm may prematurely converge to local maxim instead of global maxim. All implementations have to balance between exploration and exploitation. While search space exploration can be achieved by weaker selection pressure and allowing more reproductive variations the exploitation being the opposite means faster convergence.

For this optimization problem which have constrained volume and fixed aspect ration, i.e.  $r_o$  and  $h$  is given, the genotypes are coded as follows.  $R_{\text{ratio}}$  is a real number between zero and one, which is used to calculate

$$r_i = R_{\text{ratio}} \cdot r_o \quad (95)$$

$$r_{\text{mag}} = r_i - G_c \quad (96)$$

Similarly  $H_{\text{ratio}}$  and  $T_{\text{ratio}}$  are real numbers between zero and one which is used for

$$h_{\text{coil}} = H_{\text{ratio}} \cdot h \quad (97)$$

$$t_0 = T_{\text{ratio}} \cdot h_{\text{coil}} \quad (98)$$

$$h_{\text{mag}} = \begin{cases} h - h_{\text{coil}} + t_0 & \text{(for one coil configuration)} \\ h - 2h_{\text{coil}} + 2t_0 & \text{(for two coil configuration)} \end{cases} \quad (99)$$

The maximum output power is calculated using the procedure described in Section 3.2 and it is used as the fitness of the individual. Distributed Evolutionary Algorithms in Python (DEAP) was used in the evolutionary algorithm implementation. Short introduction to the DEAP can be found from [43]. Figure 51 shows how the  $P_{\text{max}}$ ,  $R_{\text{ratio}}$ ,  $H_{\text{ratio}}$  and  $T_{\text{ratio}}$  evolve from generation to generation. each line show minimum and maximum value of the population in solid line and average of the population in dashed line. Figure 52 shows the optimized coil and the axial magnetic flux contour map.

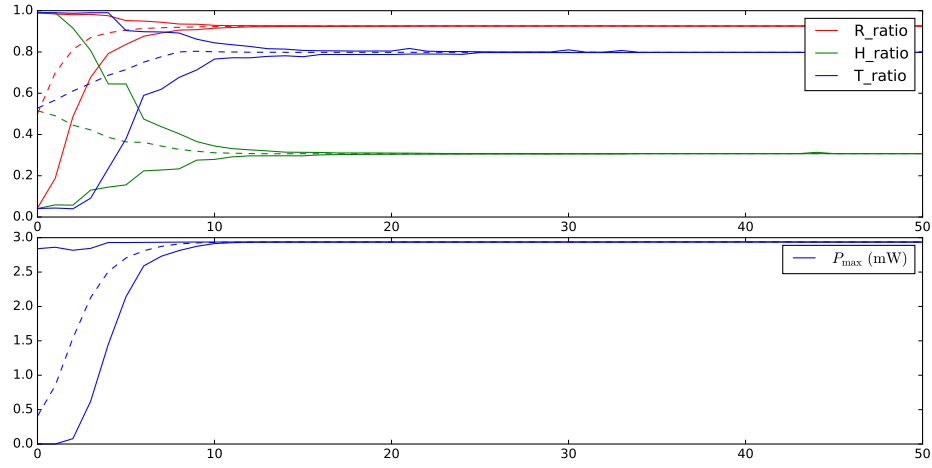


Figure 51: Genotypes and output power evolution as a function of generations.

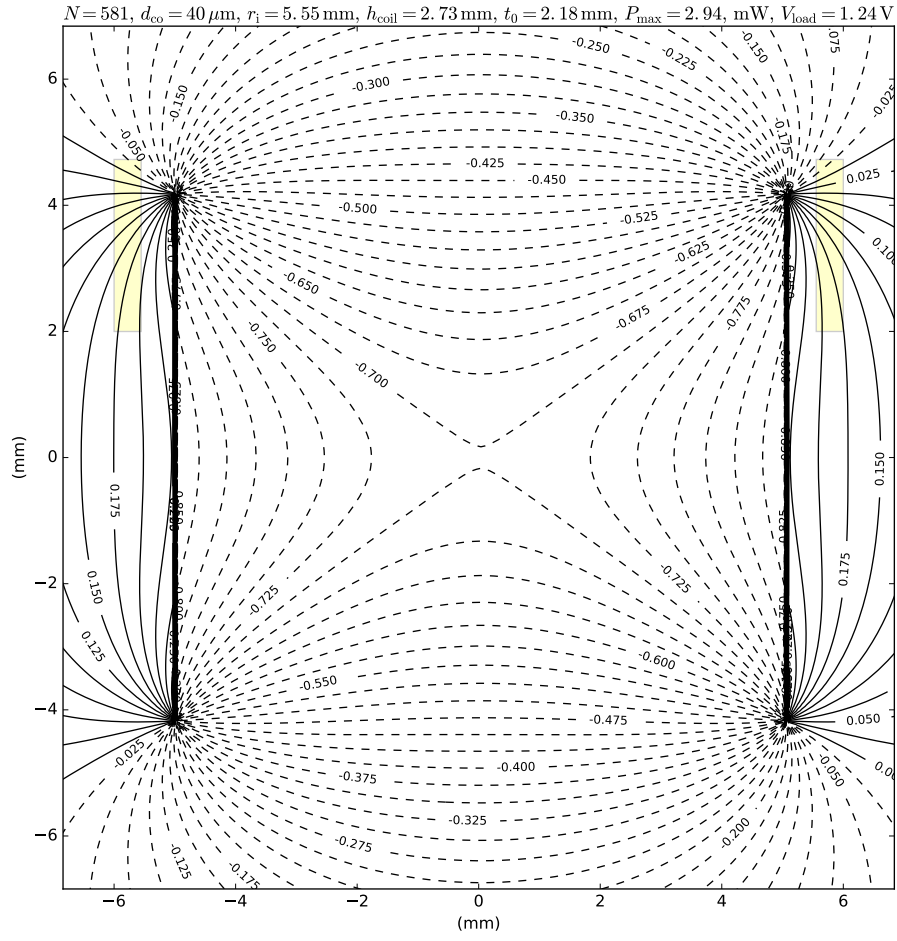


Figure 52: Optimized one coil design and axial magnetic flux countours.



This magnet in-line with coil configuration is shown in [26] to be inferior to other architectures mainly because the author uses only one coil version in his comparisons. However, if he would have included the two coil version the ranking between competing configurations would have been totally different. Table 16 shows output power and voltage advantage using two coils instead of one in the harvester. This table have data published by Spreeman as a reference as well as two dimensional parameter sweeps where  $t_0$  is kept constant and  $r_i$  and  $h_{\text{coil}}$  are swept and the parameters responsible of the maximum output power is recorded. This parameter sweep is done to evaluate the implementation of the GA algorithm. Table 16 shows that the DEAP optimization framework can be trusted since its results are very close to the simple parameter sweep.

Table 16: Optimization result comparison

Method	coils	$P_{\text{load,max}}$	$V_{\text{load}}$	$r_i$	$h_{\text{coil}}$	$h_{\text{mag}}/h$	$t_0/h_{\text{coil}}$
		mW	V	mm	mm		
[26]	1	2.94	1.47	5.41	2.53	0.92	0.75
2D search	1	2.93	1.26	5.55	2.74	0.923	0.75
GA	1	2.94	1.24	5.55	2.73	0.938	0.797
2D search	1	2.94	1.25	5.55	2.74	0.938	0.797
GA	2	3.98	2.02	5.58	2.40	0.997	0.99
2D search	2	3.98	1.99	5.60	2.49	0.994	0.99

Table 17 describes the maximum output power sensitivity to dimensional variations for  $1\text{ cm}^3$  construction volume. Each dimension is varied by  $0.1\text{ mm}$  while other dimensions are kept constant. This approach assumes that the number of turns remains constant and therefore the fill factor changes with the changing dimensions. This assumption is made because it is trivial to assure constant turn ratio in production while it is much more difficult to ensure high dimensional accuracy. The other assumption is that the changing magnet radius  $r_{\text{mag}}$  does not alter the coil inner radius  $r_i$  but instead alters the gap  $G_c$  between the magnet and the coil. With these assumptions the sensitivity analysis should better reflect the real world production variations. The amplitude of the variation is set to  $(0.1\text{ mm})$  since one magnet manufacturer [44] specifies that their manufacturing tolerances for magnets is  $\pm 0.004\text{ in} \approx \pm 0.1\text{ mm}$ .

It can be seen from Table 17 that the maximum output power is most sensitive to magnet radius  $r_{\text{mag}}$  and least sensitive to coil height  $h_{\text{coil}}$ . Also it can be seen that the relative sensitivity is similar with one and two coil configurations. It should be noted that  $0.1\text{ mm}$  is about 2% of  $r_{\text{mag}}$  with  $1\text{ cm}^3$  construction volume. For larger construction volumes the variation relative to dimensions would be smaller.

When the search space have more than two dimensions it becomes difficult to visualize the results. Using exhaustive search is also computationally expensive. While it takes almost five seconds for GA optimization to finish 50 generations of population size 500 with Intel Core i7-6700K, it will take approximately 30 seconds to exhaustively search for two dimensional search space with  $0.05\text{ mm}$  step size. In

Table 17: Output power  $P_{\max}$  sensitivity to dimensional variations

Parameter	One coil				Two coils			
	+0.1 mm		−0.1 mm		+0.1 mm		−0.1 mm	
	mW	%	mW	%	mW	%	mW	%
$h_{\text{mag}}$	0.08	2.7	−0.08	−2.7	0.11	2.8	−0.10	−2.5
$r_{\text{mag}}$	0.45	15.3	−0.40	−13.6	0.54	13.6	−0.49	−12.3
$h_{\text{coil}}$	0.02	0.7	−0.03	−1.0	0.08	2.0	−0.05	−1.3
$r_{\text{i}}$	−0.07	−2.4	0.07	2.4	−0.07	−1.8	0.07	1.8
$r_{\text{o}}$	−0.07	−2.4	0.07	2.4	−0.07	−1.8	0.07	1.8
$t_0$	−0.09	−3.1	0.08	2.7	−0.12	−3.0	0.15	3.8

other words it is more than five times faster to use GA to search three dimensional search space than to exhaustively search two dimensional search space.

## 5.2 Effects of fill factor to parameter optimization

The previous optimization with constrained construction volume and fixed  $r_o$  and  $h$  were repeated with different fill factors ( $k_{co}$ ) and the results is plotted in Figure 53 and numerical results are shown in Table 18. The fixed parameters can be seen from Table 14 in Section 4.6.

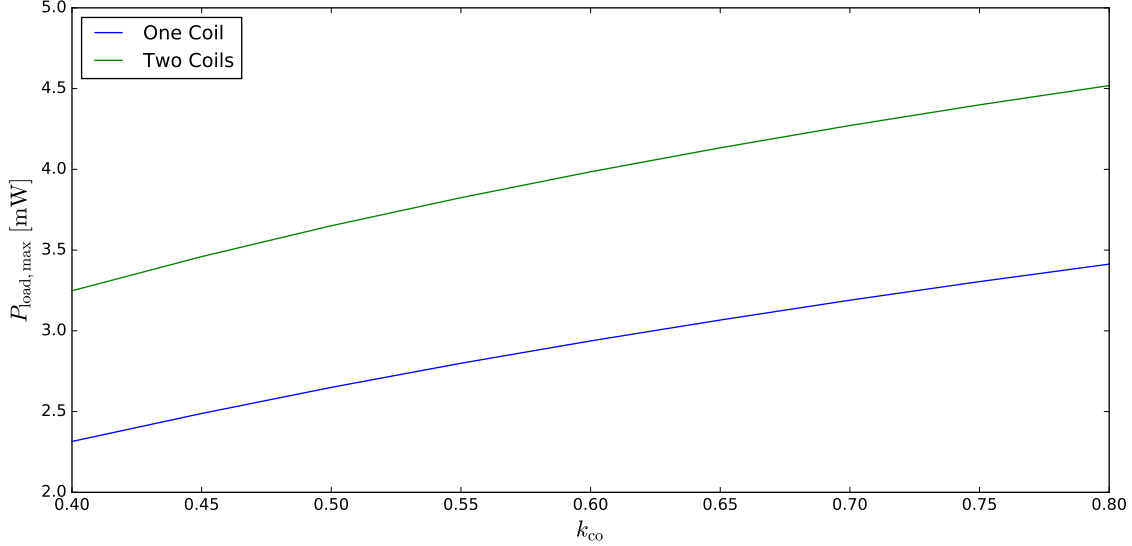


Figure 53: Optimizing the constrained volume case with different  $k_{co}$ .

Table 18: Fill factor comparison

$k_{co}$	coils	$P_{load,max}$	$V_{load}$	$r_i$	$h_{coil}$	$h_{mag}/h$	$t_0/h_{coil}$
		mW	V	mm	mm		
0.6	1	2.94	1.24	5.55	2.73	0.938	0.797
0.8	1	3.41	1.56	5.58	2.67	0.946	0.820
0.6	2	3.98	2.02	5.58	2.40	0.997	0.990
0.8	2	4.52	2.53	5.62	2.39	0.995	0.990

Higher fill ratio corresponds to higher output power as well as higher output voltage. For one coil configuration the fill factor increase from 0.6 to 0.8 increase the output power by 16.0% and for two coil configuration 13.6%. In both cases the coils reduce in size while the fill factor increase. The reduction happens from both parameters, coil height  $h_{coil}$  and coil inner radius  $r_i$ . Reduction in the size of coil allows increase in the size of the magnet. In addition, coil rounds that are closer to magnet capture more magnetic flux.

The ratio  $t_0/h_{coil}$  is 0.99 in the two coil configurations with both fill factors. This is probably due to the limit in the optimization process which does not allow any  $T_{ratio}$  to have value 1. This is done for all parameters to ensure that there will be no division by zero in the calculation procedure. Most likely the optimal value would be that  $t_0 = h_{coil}$  which would result to ratio 1 and moreover  $h_{mag} = h$ .

### 5.3 Effects of wire diameter to parameter optimization

This optimization uses six different easily available wire sizes and optimizes dimensional parameters for both one and two coil configurations. Some studies [26] suggest that the diameter of the wire have no effect on the maximum output power. However, this is true only if one assumes that the utilization factor  $k_{co}$  remains constant, i.e. if one assumes that  $k_{co} = S_2$  instead of  $k_{co} = S_1 S_2$ . This optimization assumes that such a manufacturing capability exists that  $S_2$  remains constant with varying wire diameter. Since there exists manufacturers [28] who ensure orthocyclic winding down to 50  $\mu\text{m}$  it is assumed that  $S_2 = 0.907$  in this optimization. The fixed parameters can be seen from Table 14 in Section 4.6.

It can be seen from the Figure 54, Figure 55 and Figure 56 that the maximum output power increases modestly while the diameter of the wire increases. However, this change is very small compared to the change on the output voltage which decreases much more steeply with increase in wire diameter.

High output voltage is also desired property since there will be some voltage drops in the rectifying stage where the AC voltage is converted to DC and the relative proportion of those voltage drops to the output voltage directly affects the overall system efficiency. Therefore, wire diameter can be used to select the desired output voltage while the output power remains relatively constant. In wire diameter selection care must be taken that the maximum current carrying capacity of the wire is not exceeded. Maximum current carrying density for compact designs such as tight winding with no air flow is 2 A/mm<sup>2</sup> according to Pressman [45] This value is given for switching mode power supplies which normally have higher currents and thicker wires and it is not sure how well it can be applied to low power energy harvesters. Sir William Henry Preece developed an equation for conductor fusing current [46].

$$I = a \cdot d^{3/2},$$

where  $I$  is the fusing current in Ampers,  $a = 80 \text{ A}$  is the material constant for copper and  $d$  is the wire diameter in millimeters.

Table 19: Current carrying capacity of copper wires

Nominal diameter	Maximum current			Fusing current Preece
	2 A/mm <sup>2</sup>	4 A/mm <sup>2</sup>	6 A/mm <sup>2</sup>	
$\mu\text{m}$	mA	mA	mA	mA
25	0.98	2.0	2.9	316
50	3.9	7.9	12	894
100	16	31	47	2 530
150	35	71	106	4 648
200	63	126	188	7 155
250	98	196	295	10 000

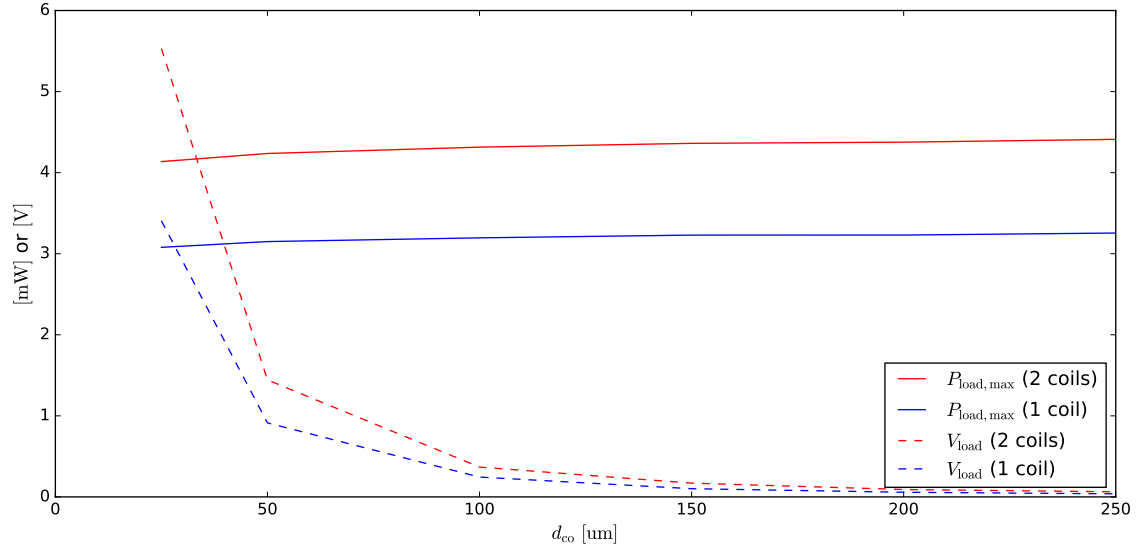


Figure 54: Optimizing 1 cm<sup>3</sup> construction volume with different  $d_{co}$ .

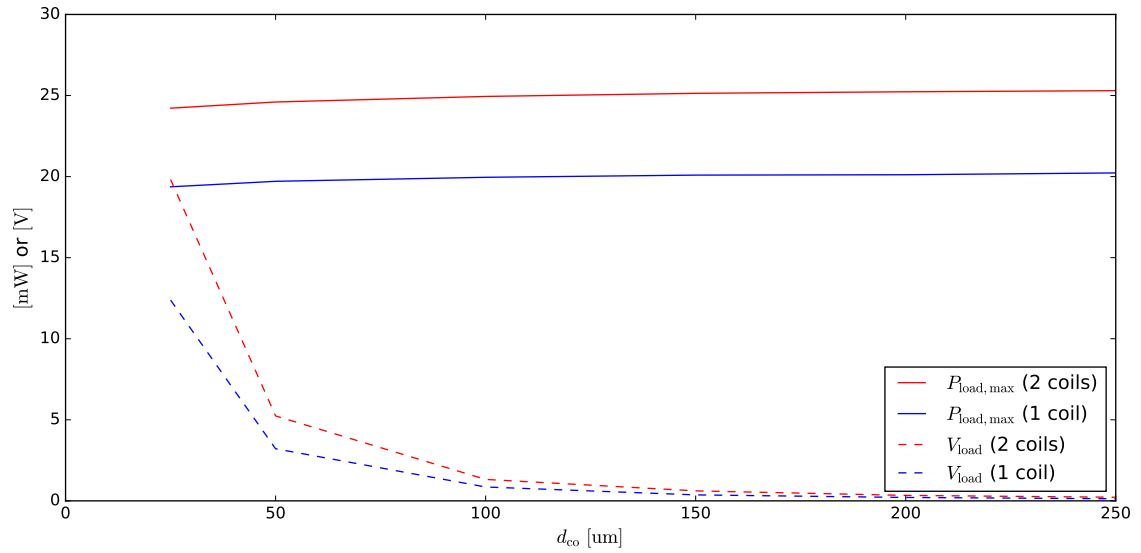


Figure 55: Optimizing 2 cm<sup>3</sup> construction volume with different  $d_{co}$ .

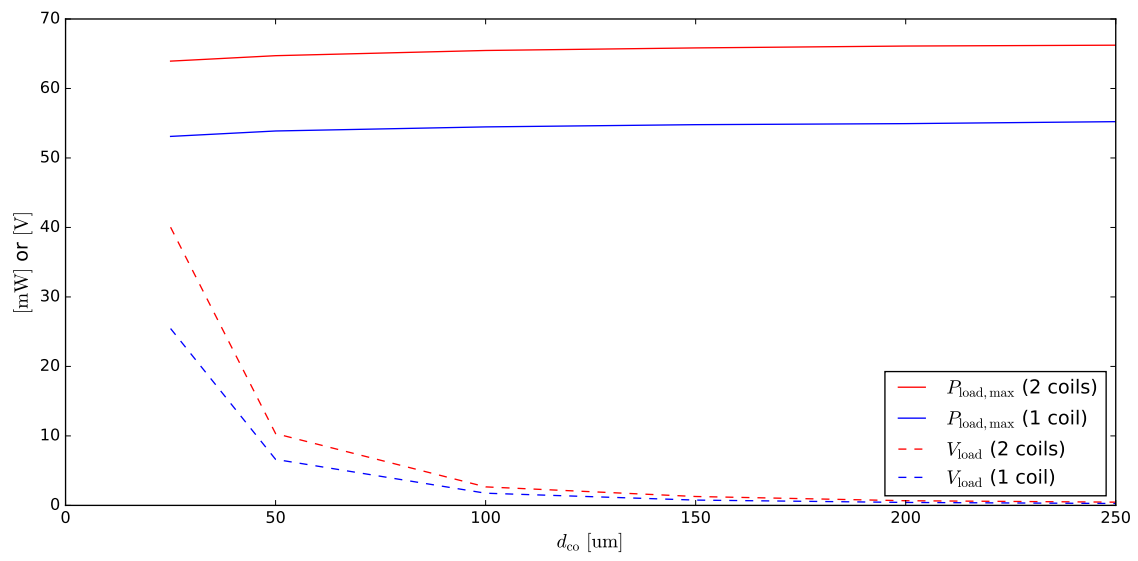


Figure 56: Optimizing  $3\text{ cm}^3$  construction volume with different  $d_{co}$ .

## 5.4 Construction volume size

This optimization solves optimal parameters for different construction volumes using the same method than in previous optimization. In this optimization the wire diameter  $d_{\text{co}} = 50 \mu\text{m}$  and therefore typical fill factor  $k_{\text{co}} = 0.686$  with ortocycling winding. The fixed parameters can be seen from Table 14 in Section 4.6. It can be seen from the Table 20 and Figure 57 that the maximum output power to the load  $P_{\text{load}}$  increases much more rapidly than either linear dimensions or the construction volume. This is partly due to the assumption that the gap (0.5 mm) between the magnet and the coil remains constant with varying feature size. This assumption is made because it is thought to be dependent on the manufacturing tolerances which cannot be altered without making significant changes to the actual manufacturing process. Other explanation is that the volume of the magnet increases faster than the construction volume, in other words, the relative volume of the magnet increases as a function of  $r_o$ . This increase can be seen in Figure 58. While the changes in linear dimensions seem modest the effect on magnet volume (and mass) is in third order of the linear change and the output power is proportional to the second power of the moving magnet mass. Maximum theoretical output power from base excited harmonic vibration is [26]

$$P_{\text{theo,max}} = \frac{m^2 d_e \ddot{Y}^2}{2(d_e + d_m)^2} \quad (100)$$

Table 20: Effects of construction volume size to parameters

Dimensions			One coil				Two coils			
$r_o$	$h$	$V$	$P_{\text{load}}$	$V_{\text{load}}$	$N$	$R_{\text{coil}}$	$P_{\text{load}}$	$V_{\text{load}}$	$N$	$R_{\text{coil}}$
mm	mm	cm <sup>3</sup>	mW	V		$\Omega$	mW	V		$\Omega$
2.00	2.97	0.04	0.000 039	0.00	74	7	0.000 068	0.00	63	13
3.00	4.45	0.13	0.004 22	0.01	169	26	0.006 97	0.02	140	43
4.00	5.93	0.30	0.081 8	0.07	253	52	0.126	0.12	213	89
5.00	7.42	0.58	0.657	0.30	341	89	0.941	0.50	288	151
6.00	8.90	1.01	3.148	0.88	407	128	4.236	1.44	338	214
7.00	10.38	1.60	10.88	2.13	475	175	13.91	3.40	378	281
8.00	11.87	2.39	30.22	4.37	519	220	37.09	6.87	405	345
9.00	13.35	3.40	71.93	8.10	560	268	85.50	12.57	425	409
10.00	14.83	4.66	152.8	14.06	609	325	177.0	21.71	454	487

Figure 59 shows that the two coil harvester configuration is especially beneficial with small construction volumes in terms of output power and output voltage. However, the benefit for output power decreases with increasing  $r_o$ . While this is also true for the output voltage the effect is not as dramatic. When the construction volume size increases even further there may be a point where the increase in performance does not warrant the increase in production costs.

Other effect of the construction size is that the size of mechanical tolerances are smaller relative to the dimensions of harvester. Since the radius of the magnet  $r_{\text{mag}}$

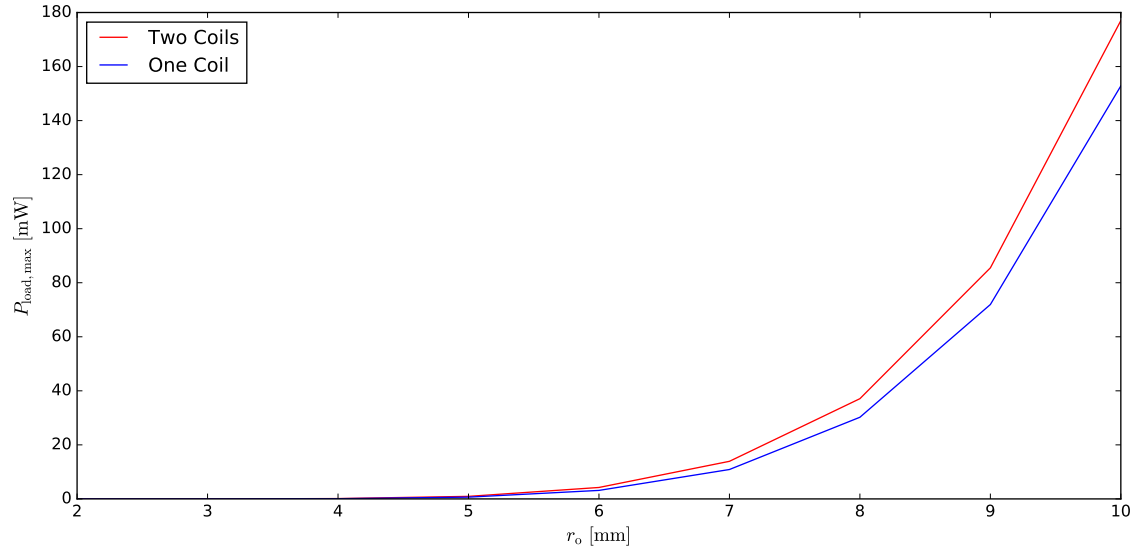


Figure 57: Output power as a function of  $r_o$ .

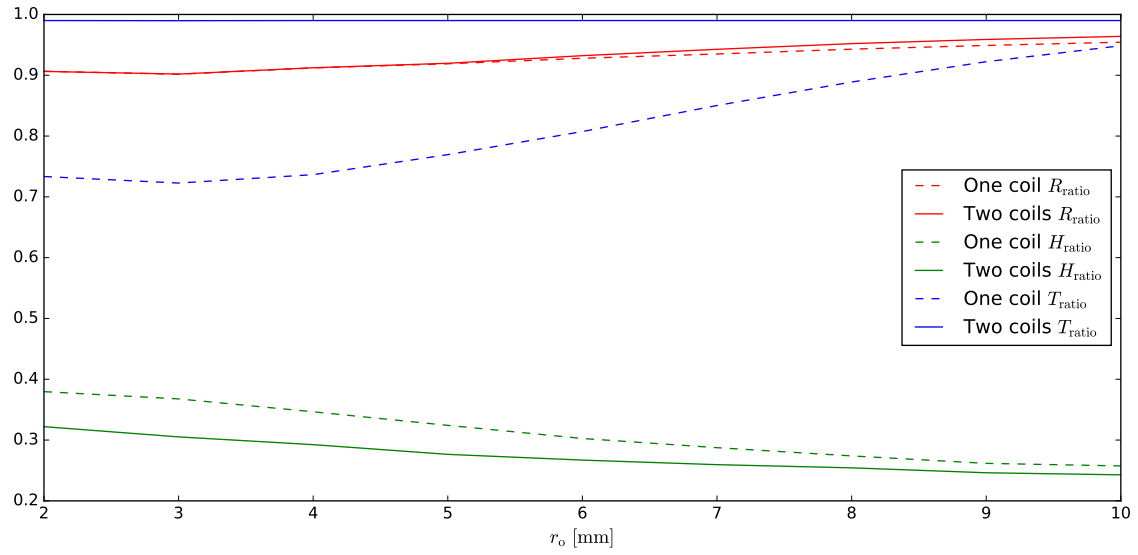


Figure 58: Dimensional ratios as a function of  $r_o$ .



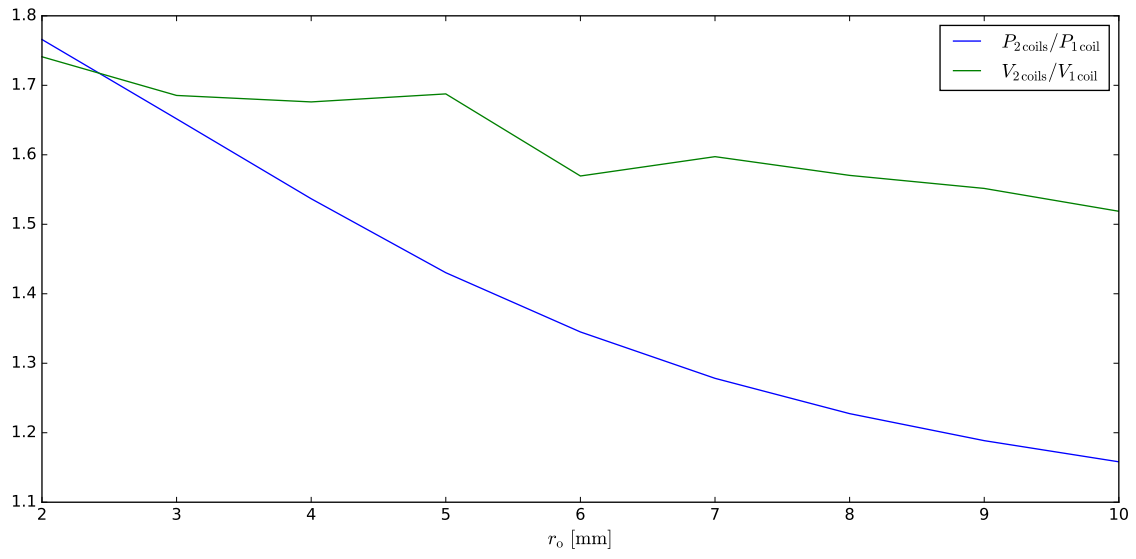


Figure 59: Output power and voltage of two coils configuration relative to one coil configuration.

is most sensitive to the manufacturing dimensions its sensitivity is calculated over the different dimensions. Figure 60 shows how the output power changes relatively to the maximum output power. This sensitivity analysis have the same assumptions as previously, mainly that the gap between the magnet and the inner radius of the coil  $r_i$  changes with changing magnet radius  $r_{\text{mag}}$ .

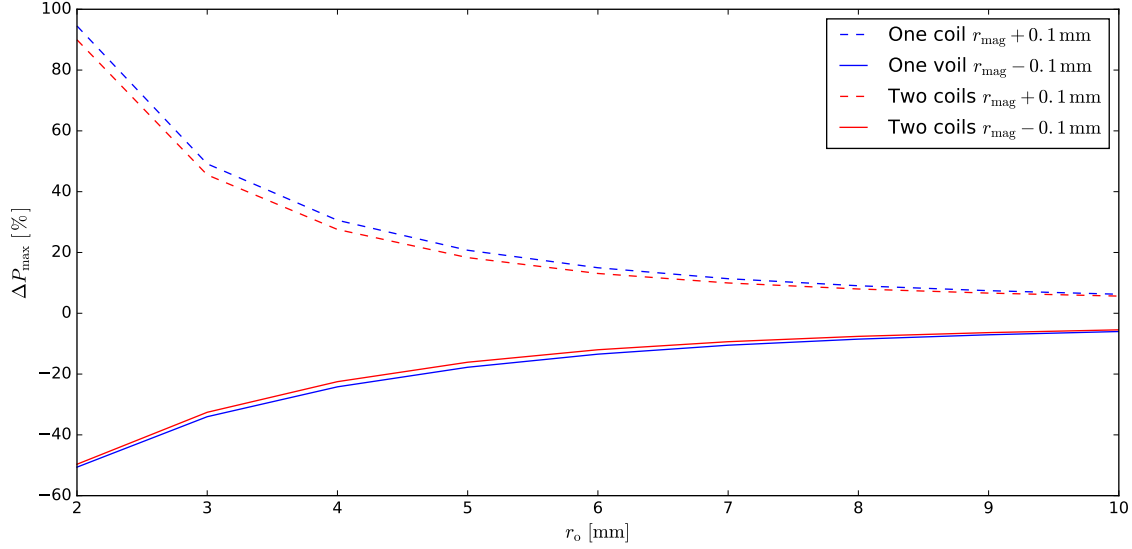


Figure 60: Output power and voltage change with  $r_{\text{mag}}$  variation.

## 5.5 Shape of the construction volume

In all previous optimizations the aspect ratio

$$HR = \frac{h}{r_0} = \text{constant} \quad (101)$$

was fixed. From fixed aspect ratio the coil output radius ( $r_o$ ) can be solved

$$HR = \frac{V_{\text{max}}}{\pi \cdot r_o^3} \implies r_o = \sqrt[3]{\frac{V_{\text{max}}}{\pi \cdot HR}} \quad (102)$$

The goal of this optimization is to find the optimum shape for the construction volume. To reduce the search space it is possible to impose boundary which determines the maximum possible aspect ratio. This boundary is called  $HR_{\text{max, ratio}}$  and its value is set to 2. This allows calculating the coil outer radius, using  $HR_{\text{ratio}}$  which is a variable between zero and one,

$$r_o = \sqrt[3]{\frac{V_{\text{max}}}{\pi \cdot HR_{\text{max, ratio}} \cdot HR_{\text{ratio}}}} \quad (103)$$

and maximum height of the construction

$$h = \frac{V_{\max}}{\pi \cdot r_o^2} \quad (104)$$

Rest of the dimensions are calculated in a similar manner than before. In this optimization the residual flux density of the permanent magnet was 1.1 T, the wire diameter  $d_{\text{co}} = 50 \mu\text{m}$  and therefore typical fill factor  $k_{\text{co}} = 0.686$  with orthocyclic winding. The fixed parameters can be seen from Table 14 in Section 4.6. Figure 61 shows the progress of the optimization for  $2 \text{ cm}^3$  construction volume. Figure 62 shows the final dimensions of the coil and magnet and the isometric axial magnetic flux density lines.

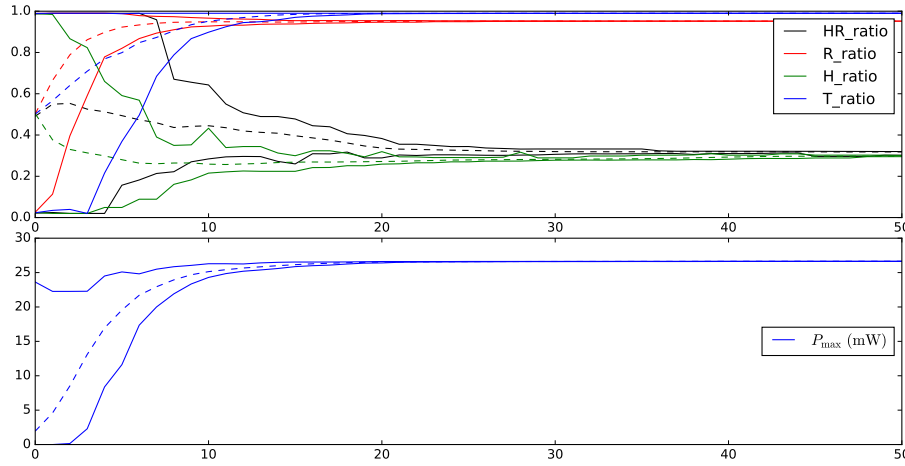


Figure 61: Optimization progress dimensions for  $2 \text{ cm}^3$  construction volume.

Optimal dimensional proportions as a function of construction volume are presented in Figure 63. This figure shows that the optimal resting position for the magnet is at  $t_0 = h_{\text{coil}}$  when the construction volume is greater than  $2 \text{ cm}^3$  and that there are no difference between one or two coil configuration beyond that point. The thickness of the coil ( $r_o - r_i$ ) remains relatively constant and this is shown in the red lines where the coil inner radius grows closer to coil outer radius as the construction volume size increases.

The optimal aspect ratios as a function of construction volume are illustrated in Figure 64. It shows that the optimal optimal aspect ratio ( $h/r_o$ ) becomes smaller as the construction volume increases and that the aspect ratio is smaller in two coil configuration than it is with one coil configuration.

Even though optimal aspect ratio exists for any given harvester the impact of the aspect ratio optimization is minute to the maximum available output power as can be seen from Figure 65. The aspect ratio can vary from 0.35 to 1.5 and the maximum output power is within 10% of its optimal value for both configurations. It may then be beneficial to use magnets with high aspect ratio because it may benefit more from reduced wall friction than what it would lose with theoretical output power.

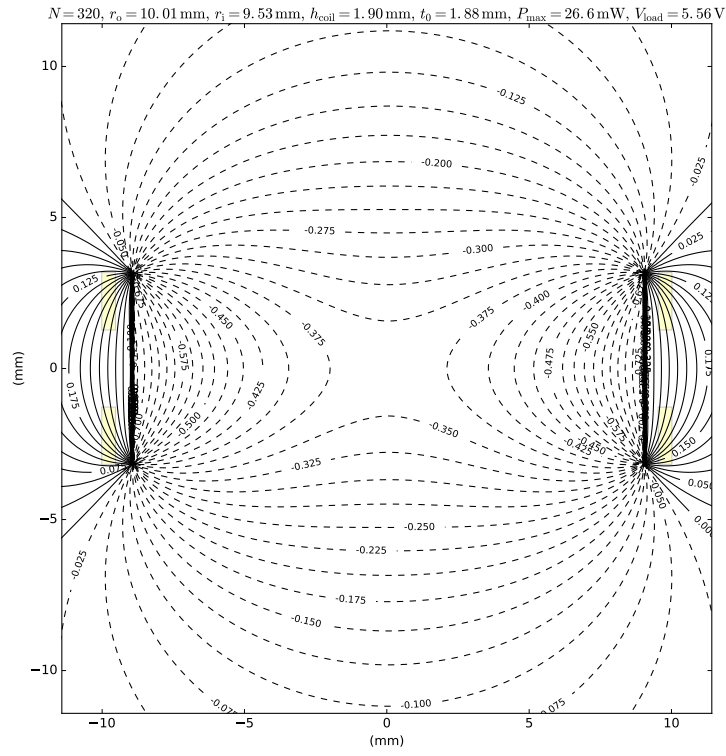


Figure 62: Optimal dimensions for  $2 \text{ cm}^3$  construction volume.

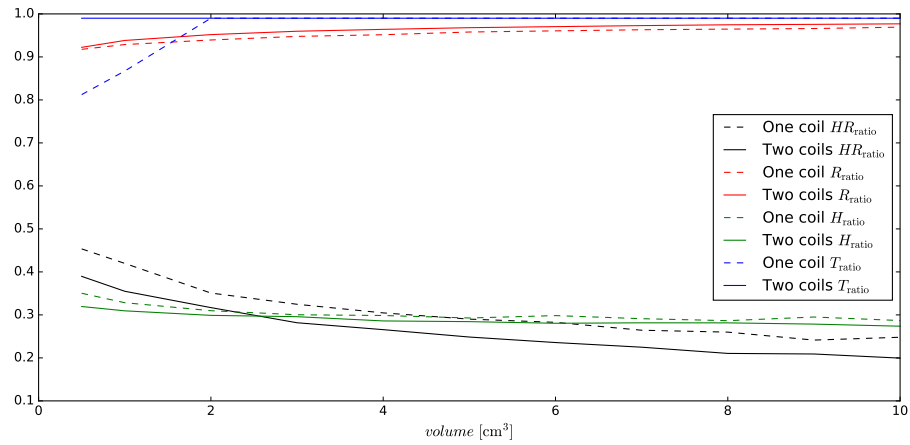


Figure 63: Optimal dimensions as a function of construction volume.

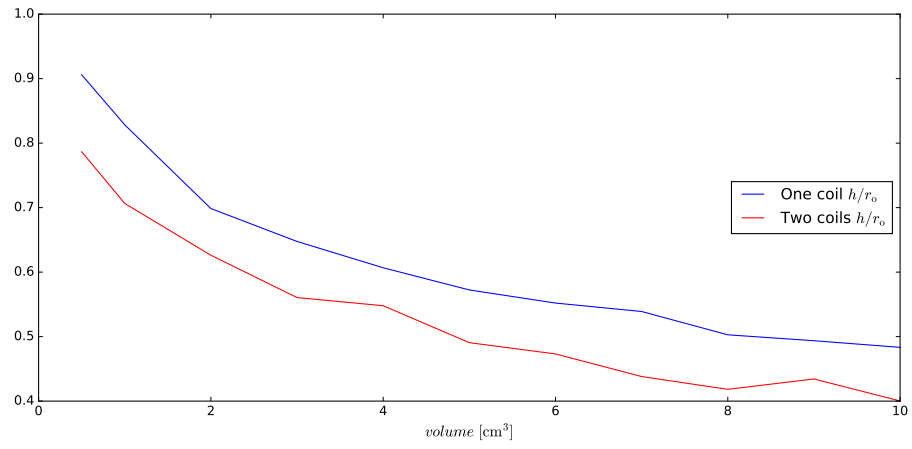


Figure 64: Optimal aspect ratio as a function of construction volume.

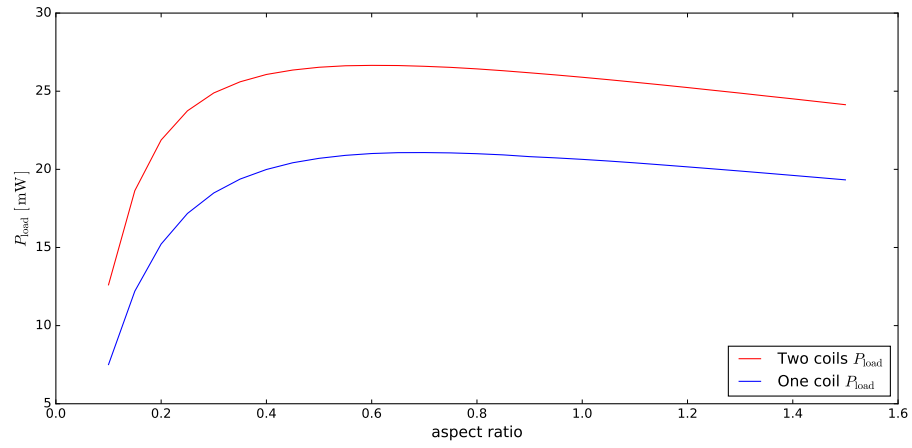


Figure 65: Output power as a function of aspect ratio for  $2 \text{ cm}^3$  construction volume.

## 5.6 Residual flux density of the permanent magnet

The purpose of this parameter sweep is to see how much the residual flux density of the permanent magnet affects to the output power. Each time the  $B_r$  is changed and then the maximal output power for  $2\text{ cm}^3$  construction volume is derived and the results are shown in Figure 66. The fixed parameters can be seen from Table 14 in Section 4.6. Neodymium magnets are strongest permanent magnet currently commercially available. Table 21 shows the properties of different neodymium magnets. Below the maximum operating temperature defined by the temperature grade the demagnetization is reversible. Demagnetization is irreversible between the maximum operating temperature and the curie temperature and all magnetization is lost at the curie temperature. The proper selection of the magnet temperature grade should ensure that the worst case operating conditions are below the maximum operating temperature conditions with a proper safety margin. Railway standard EN 50155 [1] temperature class TX defines the maximum ambient air temperature as  $85^\circ\text{C}$ . If more than  $15^\circ\text{C}$  safety margin is desired then the proper temperature grade should be at least  $120^\circ\text{C}$ .

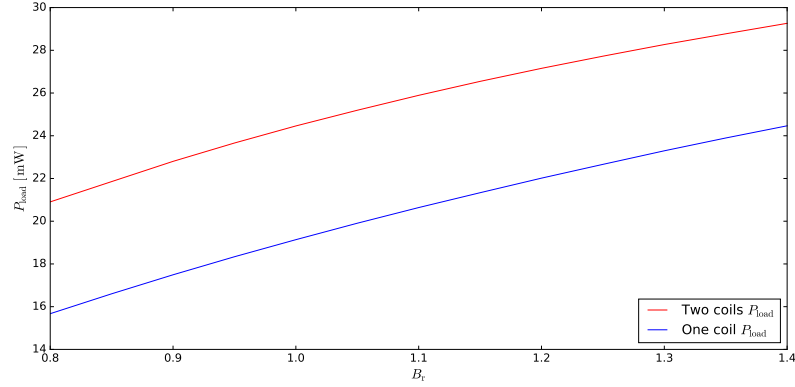


Figure 66: Output power as a function of permanent magnet residual flux density  $B_r$ .

Neodymium magnets with N42 grade and  $150^\circ\text{C}$  maximum operating temperature

Table 21: Residual flux densities [44]

Material type	$B_r$	Max. temp. grade	Curie temp.
	T	$^\circ\text{C}$	$^\circ\text{C}$
N35	1.17 – 1.21	200	350
N38	1.22 – 1.26	200	350
N40	1.26 – 1.29	180	340
N42	1.30 – 1.32	150	340
N45	1.33 – 1.37	150	340
N48	1.38 – 1.42	120	340
N50	1.41 – 1.45	100	340

are readily available as a off-the-shelf items while the 120 °C versions are harder to find. Similarly while N42 seems to be more readily available than N50. Residual flux density tolerances of  $\pm 0.02$  T changes the maximum output power  $\pm 0.244$  mW which is  $\pm 1$  % for both one coil configuration and 0.221 mW which is 0.8 % for two coil configuration.

## 5.7 Fixed magnet

In previous optimization approaches the increase in the size of the magnet were more beneficial than the increase in the size of the coils. In this optimization approach the magnet is fixed and the goal is to find the coil dimensions that gives the maximum output power without restrictions to the dimensions of the coil. Now there are three optimization parameters  $R_{\text{ratio}}$ ,  $H_{\text{ratio}}$  and  $T_{\text{ratio}}$  that determines the dimension with the  $R_{\text{maxratio}} = 3$  which sets the upper limit to the search space.

$$r_i = r_{\text{mag}} + G_c \quad (105)$$

$$r_o = r_i \cdot (1 + R_{\text{ratio}} \cdot R_{\text{maxratio}}) \quad (106)$$

$$h_{\text{coil}} = H_{\text{ratio}} \cdot h_{\text{mag}} \quad (107)$$

$$t_0 = T_{\text{ratio}} \cdot h_{\text{coil}} \quad (108)$$

In this optimization the fixed parameters are  $B_r = 1.31$  T,  $G_c = 1.26$  mm,  $d_{\text{co}} = 150$   $\mu\text{m}$ ,  $r_{\text{mag}} = 4.7625$  mm and  $h_{\text{mag}} = 19.05$  mm unless otherwise noted. Two dimensional parameter sweep helps to visualize effect of  $r_o$  and  $h_{\text{coil}}$  to the harvester parameters. Figure 69 that there will be no optimum for transconductance or output voltage since they increase without bound as the size of the coil increase. However, this does not hold true for maximum output power since with the increase in coil size also the resistance of the coil increases and therefore the output power maximum exists. The figure also shows that the output power is not very sensitive to the dimensions of the coil. The second most inner contour line defines the values of  $r_o$  and  $h_{\text{coil}}$  which produces at least 22 mW output power to resistive load. This is more than 91.3% of the maximum output power. This suggest that the harvester is not sensitive to the variation of  $r_o$  or  $h_{\text{coil}}$ . Coil may be minimized significantly with only a modest effect to the output power but more dramatic effect to the available output voltage.

Since the the coils size is much larger proportionally to the size of the magnet than in constrained volume optimization the affect of the wire size to the output needs to be evaluated again. Table 22 shown the effect of wire size to the dimensions and other parameters of the harvester. It can be seen that the optimal size of the coil does not change with changing wire diameter and the output power remains approximately the same. However the coil resistance ( $R_{\text{coil}}$ ), voltage over load ( $V_{\text{load}}$ ) and optimal load resistance ( $R_{\text{load}}$ ) depends on the wire diameter. While two coils doubles the output voltage it also doubles the coil resistance and increase the optimal output resistance to almost fourfold since  $R_{\text{load,optim}} = R_{\text{coil}} + k_t^2/d_m$ .

Figure 67 shows optimization progress and Figure 68 shows the results of coil dimension optimization for magnet which have  $r_{\text{mag}} = 4.7625$  mm and  $h_{\text{mag}} = 19.05$  mm.

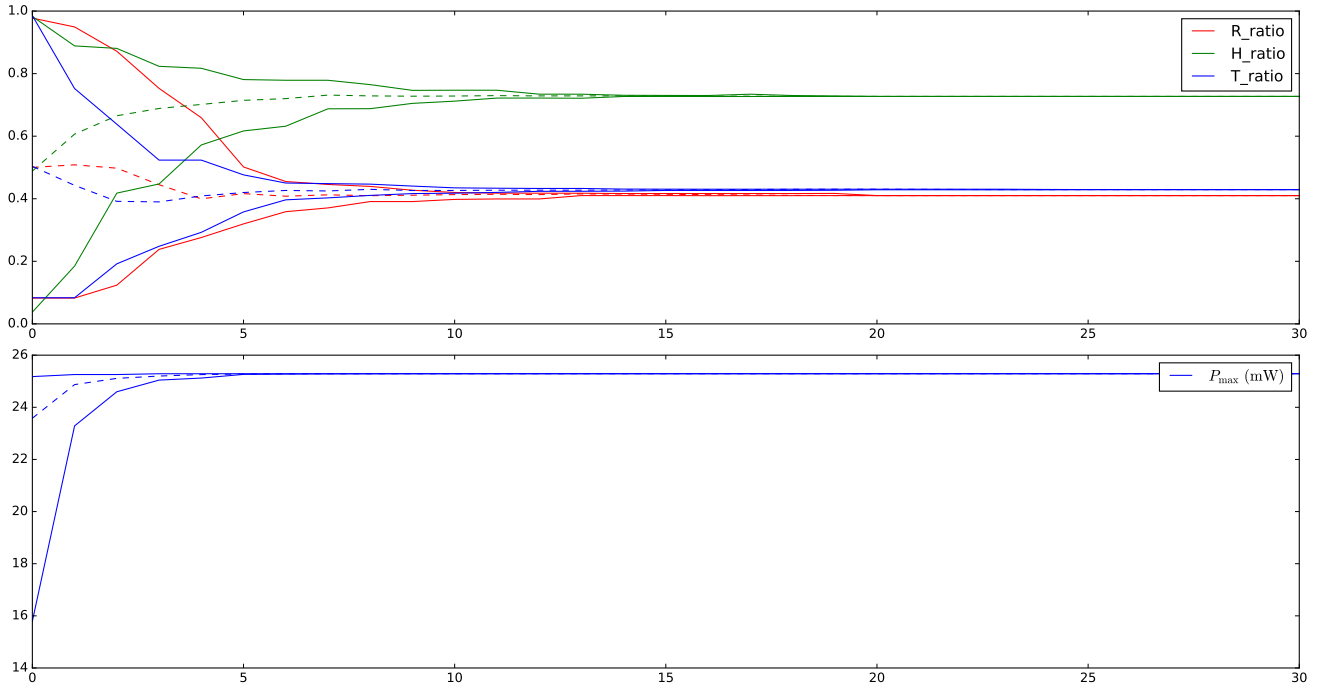


Figure 67: Coil optimization progress for fixed magnet with  $r_{\text{mag}} = 4.7625 \text{ mm}$  and  $h_{\text{mag}} = 19.05 \text{ mm}$ .

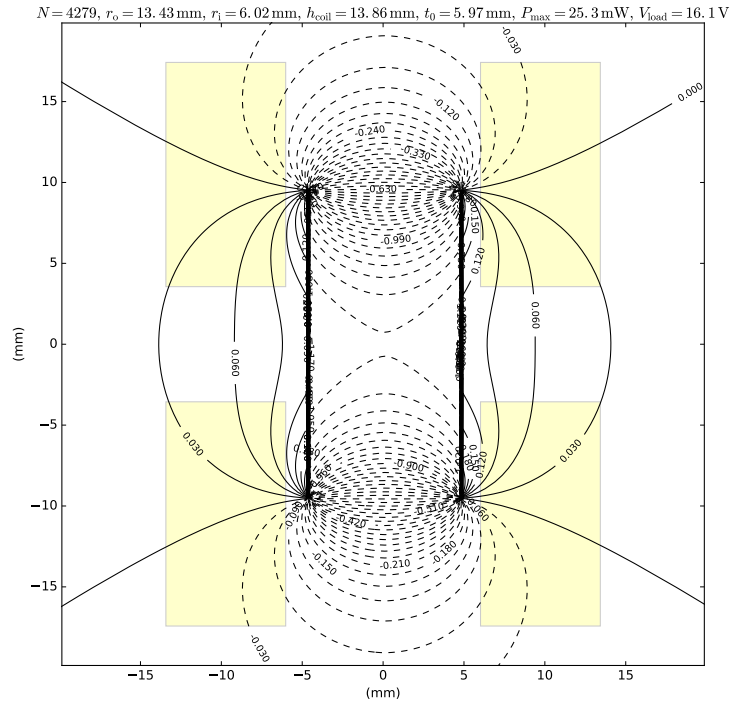


Figure 68: Optimal coil dimension for permanent magnet with  $r_{\text{mag}} = 4.7625 \text{ mm}$  and  $h_{\text{mag}} = 19.05 \text{ mm}$ .



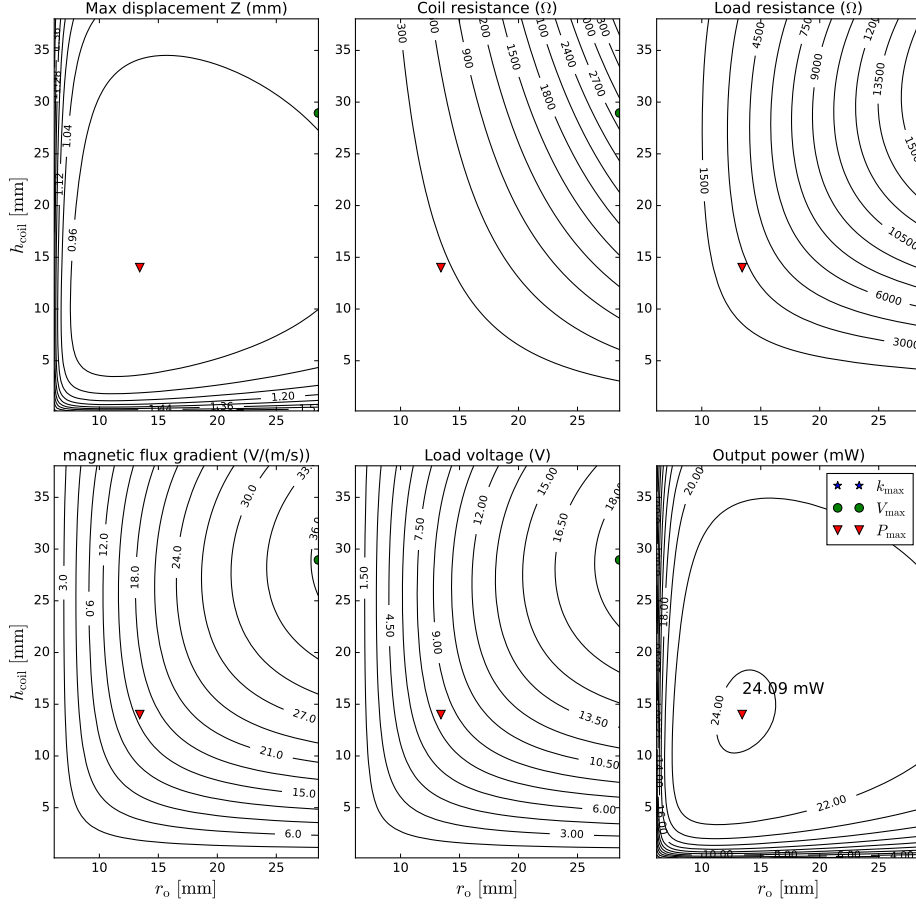


Figure 69:  $r_o$  and  $h_{coil}$  parameter sweeps for harvester with  $B_r = 1.31$  T,  $G_c = 1.26$  mm,  $d_{co} = 150$   $\mu$ m,  $k_{co} = 0.736$ ,  $r_{mag} = 4.762$  5 mm and  $h_{mag} = 19.05$  mm.

Table 22: Harvester optimized parameters as a function of  $d_{co}$

$d_{co}$	$P_{load}$	$V_{load}$	$N$	$k$	$R_{coil}$	$R_{load}$	$r_i$	$r_o$	$h_{coil}$	$t_0$
$\mu$ m	mW	V		V/(m/s)	$\Omega$	$\Omega$	mm	mm	mm	mm
One coil										
50	23.95	67.24	35536	130.36	18854	188778	6.02	13.38	13.83	5.94
100	24.04	17.59	9338	34.09	1240	12864	6.02	13.40	13.86	5.96
150	24.09	8.01	4269	15.54	251	2665	6.02	13.38	13.92	5.97
200	24.12	4.63	2487	8.98	82	888	6.02	13.50	13.95	5.97
250	24.13	2.92	1559	5.66	32	353	6.02	13.30	13.94	5.98
Two coils										
50	25.21	134.42	35503	260.59	37672	716724	6.02	13.38	13.82	5.94
100	25.26	35.19	9348	68.23	2483	49035	6.02	13.41	13.87	5.96
150	25.29	16.02	4262	31.05	502	10144	6.02	13.39	13.88	5.97
200	25.30	9.26	2489	17.96	166	3391	6.02	13.50	13.96	5.98
250	25.31	5.84	1559	11.33	65	1349	6.02	13.30	13.93	5.97

Figure 70 shows how much the output power increases when using the same magnet sizes as in constrained volume optimization if the construction size and hence coil size restriction is removed. The x-axis in the figure is the coil outer radius of the constrained construction size, not the output radius of the fixed magnet optimization. It can be seen that lifting the coil size restriction benefits more harvesters with smaller magnets than what it does with the bigger magnets.

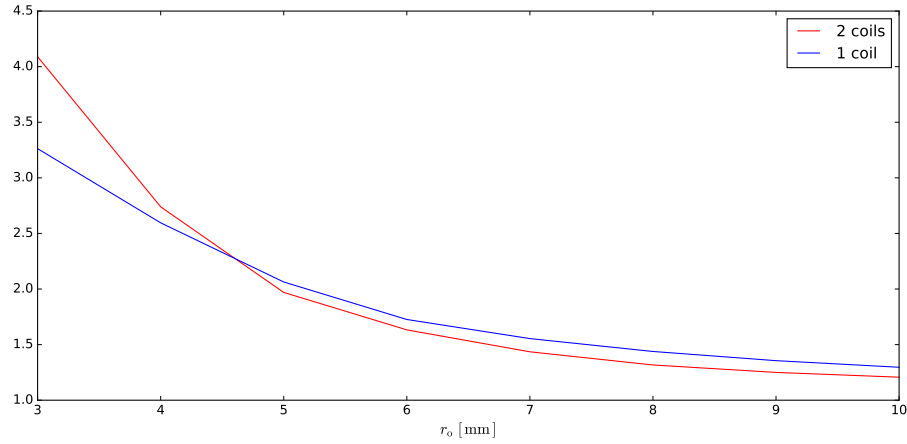


Figure 70: Output power increase when the coil size is not restricted relative to the restricted construction volume.

## 6 Conclusions

This thesis successfully achieved its aims introduced in Chapter 1 in creating computational model for single degree of freedom spring-mass-damper with main focus on moving magnet and coil dimensioning, validating the model and optimizing its parameters. Chapter 2 introduced briefly different energy harvesting technologies, compared them and showed their possible application and why such technologies are relevant for WSN and IoT. The electrical and mechanical model was presented in Chapter 3 which was consequently validated in Chapter 4. Finally the model was used to solve different optimization problems in Chapter 5.

The initial assumptions were that the available vibration levels ( $>1\text{ g}$  at axle) and frequency is known and that the harvester and its resonance frequency can be tuned to that most dominant ambient frequency. It is also assumed that the moving mass is large compared to the mass of the harvester and that the wireless sensor node will consume on average less than  $1\text{ mW}$ . Since the vibration frequency could vary and it may not always be at the resonance frequency of the energy harvester the required power level would be at least  $10\text{ mW}$  at  $1\text{ g}$ . These assumptions defines the search space for the optimization.

Magnetic spring restoration force calculation agreed well with the measurements and it can be used to set the resonant frequency of the harvester. Linearization of the spring constant resulted accurate predictions for the maximum output power since the displacement of the moving magnet remains in a fairly linear region when the output load is optimal. The use of magnet springs is not mandatory for the operation of the harvester and they can be replaced with ordinary springs with more linear spring coefficient.

Viscous damping coefficient modelling resulted over optimistic values and for more accuracy wall friction model should be incorporated to the mechanical model. Measured viscous damping coefficients could also be used to make the predictions more accurate. Since the friction is determined mainly on the material properties the desired damping level should be achievable with proper material choices and this desired value can then be used as an input for the optimization.

Magnetic flux linkage calculation demonstrated to be both computationally inexpensive with modern computers as well as highly accurate. As long as the position and velocity of the moving magnet is known the output voltage and hence output power to resistive load can be calculated accurately. This part and its validation took the most of the efforts in this thesis. There were four different algorithms for magnetic flux density calculation and the diversity of algorithms provided both cross validation and speed comparison between them.

Parameter optimization revealed that many generalizations made in the literature does not hold true if even one fixed parameter is changed. One of the most comprehensive study in the literature does not analyze two coil configuration at all and it only analyses and compares harvesters in construction volume of  $1\text{ cm}^3$ . The two coil configuration is most advantageous in small construction volumes but its benefits decrease with increasing construction size. The mass of the moving magnet is the single most important factor determining the maximum output power for the

vibration energy harvester with limited construction volume since the mass of the magnet is dependent on the volume of the magnet and the maximum output power is proportional to the proof mass squared.

Most papers in the literature uses copper fill factor  $k_{co}$  of hand-wound coils even though production capabilities exist to use orthocyclic winding down to  $50\text{ }\mu\text{m}$  wire diameters and I have not yet seen an analysis that considers the insulation thickness of the enamelled copper wire. The change in the maximum output power changes only minutely with wire diameter but both output voltage and output impedance changes dramatically. This means that the wire diameter selection can be used to provide proper voltage to the rectifier and power conditioning circuit. Magnet with highest possible residual flux density should be used.

Other optimization approach presented in this thesis uses predefined magnet size and shape and finds optimal dimensions for the coil(s) without space restrictions. In this approach the coil size does not compete from the same space with the magnet and hence the size of the optimal coils are significantly larger and they are not that sensitive to the manufacturing tolerances. However the beneficial effect of using larger coils diminishes with increase in the size of the magnet.

Future research could include rectifying and power conditioning to the optimization loop. This could result in different optimal dimensions since the complete system is to be optimized instead of just the harvester. Other possible ways to extend this research is to finding ways to increase the bandwidth of the operation. These could include using several harvesters in parallel with different resonance frequencies or actively changing the resonance frequency. Different topologies could also be evaluated and the use of back iron or similar element which guides the magnetic flux around the coil. The damping model is another area that could be improved by including the wall friction into the model.

## References

- [1] Electrotechnical Standardization, European Committee for. *Railway applications-Rolling stock equipment used on rolling stock*. 2007.
- [2] Kapanen, Tero. *EM Harvester Simulation*. Oct. 10, 2016. URL: [https://github.com/WarmT/EM\\_harvester\\_simulation](https://github.com/WarmT/EM_harvester_simulation).
- [3] Kazmierski, Thomas J. and Beeby, Steve. *Energy harvesting systems : principles, modeling and applications*. Springer, 2011. ISBN: 9781441975669 (electronic bk.) DOI: [10.1007/978-1-4419-7566-9](https://doi.org/10.1007/978-1-4419-7566-9).
- [4] B.V., Elsevier. *Scopus*. Dec. 27, 2015. URL: <http://www.scopus.com/>.
- [5] Rob van der Meulen, Gartner. *Gartner Says 6.4 Billion Connected "Things" Will Be in Use in 2016, Up 30 Percent From 2015*. Oct. 11, 2015. URL: <http://www.gartner.com/newsroom/id/3165317> (visited on 03/20/2016).
- [6] Horowitz, Paul and Hill, Winfield. The Art of Electronics. In: *The Art of Electronics, by Paul Horowitz, Winfield Hill, Cambridge, UK: Cambridge University Press, 2015* 1 (2015).
- [7] Zuo, L. and Tang, X. Large-scale vibration energy harvesting. In: *Journal of Intelligent Material Systems and Structures* 24.11 (2013), pp. 1405–1430. DOI: [10.1177/1045389X13486707](https://doi.org/10.1177/1045389X13486707).
- [8] Hendijanizadeh, M, Sharkh, SM, Elliott, SJ, and Moshrefi-Torbati, M. Output power and efficiency of electromagnetic energy harvesting systems with constrained range of motion. In: *Smart Materials and Structures* 22.12 (2013), p. 125009.
- [9] Mitcheson, Paul D, Yeatman, Eric M, Rao, G Kondala, Holmes, Andrew S, and Green, Tim C. Energy harvesting from human and machine motion for wireless electronic devices. In: *Proceedings of the IEEE* 96.9 (2008), pp. 1457–1486.
- [10] Wang, Wensi S, O'Donnell, Terence, Wang, Ningning, Hayes, Michael, O'Flynn, Brendan, and O'Mathuna, C. Design considerations of sub-mW indoor light energy harvesting for wireless sensor systems. In: *ACM Journal on Emerging Technologies in Computing Systems (JETC)* 6.2 (2010), p. 6.
- [11] Spies, Peter, Mateu, Loreto, and Pollak, Markus. *Handbook of energy harvesting power supplies and applications*. 2015. ISBN: 9789814303064.
- [12] Moss, Scott D, Payne, Owen R, Hart, Genevieve A, and Ung, Chandarin. Scaling and power density metrics of electromagnetic vibration energy harvesting devices. In: *Smart Materials and Structures* 24.2 (2015), p. 023001. DOI: [doi:10.1088/0964-1726/24/2/023001](https://doi.org/10.1088/0964-1726/24/2/023001).
- [13] Beeby, S P, Tudor, M J, and White, NM. Energy harvesting vibration sources for microsystems applications. In: *Measurement science and technology* 17.12 (2006), R175.

- [14] Wardlaw, J. L. and Karsilayan, A. İ. Self-Powered Rectifier for Energy Harvesting Applications. In: *IEEE Journal on Emerging and Selected Topics in Circuits and Systems* 1.3 (Sept. 2011), pp. 308–320. ISSN: 2156-3357. DOI: [10.1109/JETCAS.2011.2164975](https://doi.org/10.1109/JETCAS.2011.2164975).
- [15] Dayal, R., Dwari, S., and Parsa, L. A New Design for Vibration-Based Electromagnetic Energy Harvesting Systems Using Coil Inductance of Microgenerator. In: *IEEE Transactions on Industry Applications* 47.2 (Mar. 2011), pp. 820–830. ISSN: 0093-9994. DOI: [10.1109/TIA.2010.2101995](https://doi.org/10.1109/TIA.2010.2101995).
- [16] Dayal, R., Dwari, S., and Parsa, L. Design and Implementation of a Direct AC-DC Boost Converter for Low-Voltage Energy Harvesting. In: *IEEE Transactions on Industrial Electronics* 58.6 (June 2011), pp. 2387–2396. ISSN: 0278-0046.
- [17] Instruments, Texas. *SimpleLink CC3100/CC3200 Wi-Fi Internet-on-a-chip Networking Sub-system Power Management*. SWRA462–Application Report. 2014.
- [18] Wowk, Victor. *Machinery vibration: measurement and analysis*. McGraw Hill Professional, 1991.
- [19] DLI, Azima. *Commercial Standards (DLI Machinery Vibration Severity Chart)*. Sept. 17, 2016. URL: <http://azimadli.com/vibman/commercialstandardsdlimachineryvibrationseveritychart.htm>.
- [20] Commission, International Electrical et al. *Railway applications-Rolling stock equipment-Shock and vibration tests*. 2010.
- [21] Inman, D.J. *Engineering Vibration*. Pearson Prentice Hall, 2008. ISBN: 9780132281737.
- [22] Doebelin, Ernest. *System dynamics: modeling, analysis, simulation, design*. CRC Press, 1998.
- [23] Furlani, Edward P. *Permanent magnet and electromechanical devices: materials, analysis, and applications*. Academic Press, 2001.
- [24] Group, The ELEKTRISOLA. *Technical Data for Enamelled Copper Wire by Size acc. to IEC 60317*. Aug. 26, 2016. URL: <http://www.elektrisola.com/enamelled-wire/technical-data-by-size/iec-60-317.html>.
- [25] McLyman, Colonel Wm. T. *Transformer and Inductor Design Handbook*. Marcel Dekker, Inc., 2004. ISBN: 0-8247-5393-3.
- [26] Spreemann, Dirk and Manoli, Yiannos. *Electromagnetic vibration energy harvesting devices: Architectures, design, modeling and optimization*. Vol. 35. Springer Science & Business Media, 2012.
- [27] Hartu. *Orthocyclically wound air coils*. Aug. 26, 2016. URL: <http://www.hartu.de/en/orthocyclic-coils-382.html>.
- [28] UK, Recoil Limited. *Coil Winding Products*. Aug. 26, 2016. URL: <http://www.recoilltd.com/recoilproducts/recoilproducts.htm>.

- [29] Foelsch, Kuno. Magnetfeld und Induktivität einer zylindrischen Spule. In: *Archiv für Elektrotechnik* 30.3 (1936), pp. 139–157.
- [30] Friedman, MD and Byrd, MD. *Handbook of elliptic integrals for engineers and scientists*. 1971. ISBN: 3-540-04838-3.
- [31] Callaghan, Edmund E and Maslen, Stephen H. The magnetic field of a finite solenoid. In: (1960).
- [32] Derby, Norman and Olbert, Stanislaw. Cylindrical magnets and ideal solenoids. In: *American Journal of Physics* 78.3 (2010), pp. 229–235.
- [33] Stephen, NG. On energy harvesting from ambient vibration. In: *Journal of sound and vibration* 293.1 (2006), pp. 409–425.
- [34] Spreemann, D, Folkmer, B, and Manoli, Y. Comparative study of electromagnetic coupling architectures for vibration energy harvesting devices. In: *Proceedings of PowerMems* (2008), pp. 257–260.
- [35] Spreemann, Dirk, Hoffmann, Daniel, Folkmer, Bernd, and Manoli, Yiannos. Numerical optimization approach for resonant electromagnetic vibration transducer designed for random vibration. In: *Journal of Micromechanics and Microengineering* 18.10 (2008), pp. 104001+10. URL: <http://stacks.iop.org/0960-1317/18/i=10/a=104001>.
- [36] Cepnik, Clemens, Yeatman, Eric M, and Wallrabe, Ulrike. Effects of nonconstant coupling through nonlinear magnetics in electromagnetic vibration energy harvesters. In: *Journal of Intelligent Material Systems and Structures* 23.13 (2012), pp. 1533–1541.
- [37] Saha, Chitta Ranjan, O'Donnell, Terence, Loder, Heiko, Beeby, Steve, and Tudor, John. Optimization of an electromagnetic energy harvesting device. In: *IEEE Transactions on Magnetics* 42.10 (2006), pp. 3509–3511.
- [38] Büren, Thomas von and Tröster, Gerhard. Design and optimization of a linear vibration-driven electromagnetic micro-power generator. In: *Sensors and Actuators A: Physical* 135.2 (2007), pp. 765–775.
- [39] Mann, B.P. and Sims, N.D. Energy harvesting from the nonlinear oscillations of magnetic levitation. In: *Journal of Sound and Vibration* 319.1 (2009), pp. 515–530.
- [40] Green, Peter L, Worden, Keith, Atallah, Kais, and Sims, Neil D. The effect of duffing-type non-linearities and coulomb damping on the response of an energy harvester to random excitations. In: *Journal of Intelligent Material Systems and Structures* (2012), p. 1045389X12446520.
- [41] Mitra, SK. *Digital Signal Processing: A Computer-Based Approach*. New York: McGraw-Hill, 2001.
- [42] Whitley, Darrell and Sutton, Andrew M. “Genetic algorithms—A survey of models and methods”. In: *Handbook of natural computing*. Springer, 2012, pp. 637–671.

- [43] Fortin, Félix-Antoine, De Rainville, François-Michel, Gardner, Marc-André, Parizeau, Marc, and Gagné, Christian. DEAP: Evolutionary Algorithms Made Easy. In: *Journal of Machine Learning Research* 13 (July 2012), pp. 2171–2175.
- [44] Inc, K&J Magnetics. *Your Source for the World's Strongest Magnets*. Sept. 11, 2016. URL: <https://www.kjmagnetics.com/>.
- [45] Abraham I. Pressman Keith Billings, Taylor Morey. *Switching power supply design*. McGraw-Hill, Inc., 2009. ISBN: 978-0-07-148272-1.
- [46] Preece, William Henry. On the heating effects of electric currents. No. III. In: *Proceedings of the Royal Society of London* 44.266-272 (1888), pp. 109–111.



## A Repulsion force calculation

```

1 from __future__ import division
import numpy as np
3 from numpy import cos, power, sqrt, pi, multiply, array
from scipy.interpolate import interp1d
5 from numba import jit

7
@jit
9 def calc_force_dist(r_m1, h_m1, Br_m1, r_m2, h_m2, Br_m2, d, Nr, Nphi):
    mu0 = 1.256637e-6
11    m1_Ms = Br_m1 / mu0
    m2_Ms = Br_m2 / mu0
13    m1_Rslice = (r_m1 * r_m1) / Nr
    m2_Rslice = (r_m2 * r_m2) / Nr
15    const = mu0 * m1_Ms * m2_Ms * Nphi / (4 * pi) * multiply(pi * m1_Rslice /
        Nphi, pi * m2_Rslice / Nphi)

17    delta_phi = 2 * pi / Nphi
    hm = array([d, -(d + h_m1), -(d + h_m2), (d + h_m1 + h_m2)], dtype='float')
19    S1 = 0.0
    R_i_prev = 0.0
21    for i in range(0, Nr):
        R_i = sqrt(R_i_prev * R_i_prev + m1_Rslice)
23        ri = (R_i + R_i_prev) / 2
        R_i_prev = R_i
25        S2 = 0.0
        R_ii_prev = 0.0
27        for ii in range(0, Nr):
            R_ii = sqrt(R_ii_prev * R_ii_prev + m2_Rslice)
29            rii = (R_ii + R_ii_prev) / 2
            R_ii_prev = R_ii
31            S3 = 0.0
            ri_rii_producs = ri * ri + rii * rii
33            hm0_p1 = ri_rii_producs + hm[0] * hm[0]
            hm1_p1 = ri_rii_producs + hm[1] * hm[1]
35            hm2_p1 = ri_rii_producs + hm[2] * hm[2]
            hm3_p1 = ri_rii_producs + hm[3] * hm[3]
37            p2 = 2 * ri * rii
            for j in range(0, Nphi):
39                phi = j * delta_phi + delta_phi / 2
                S3 += hm[0] / power(hm0_p1 - p2 * cos(phi), 3 / 2) \
41                    + hm[1] / power(hm1_p1 - p2 * cos(phi), 3 / 2) \
                    + hm[2] / power(hm2_p1 - p2 * cos(phi), 3 / 2) \
43                    + hm[3] / power(hm3_p1 - p2 * cos(phi), 3 / 2)
            S2 += S3
45        S1 += S2
    F = const * S1
47    return F

49
51 def calc_force(r_m1, h_m1, Br_m1, r_m2, h_m2, Br_m2, h_range, Nr, Nphi):
    F = np.zeros(h_range.size)

```

```

53     for index, d in enumerate(h_range):
        F[index] = calc_force_dist(r_m1, h_m1, Br_m1, r_m2, h_m2, Br_m2, d, Nr,
        Nphi)
        return F
55
57 def calc_force_to_moving_magnet(r_m1, h_m1, Br_m1, r_m2, h_m2, Br_m2, Nr, Nphi,
    d_sep, h_steps):
    h_min = 0.001 # minimum distance between opposing magnets is 1 mm
59     h_range = np.linspace(h_min, 2 * d_sep, 2 * h_steps)
    F = calc_force(r_m1, h_m1, Br_m1, r_m2, h_m2, Br_m2, h_range, Nr, Nphi)
61     fem_int = interp1d(h_range, F, kind='cubic')
63
    x_int = np.linspace(-d_sep + 2 * h_min, d_sep - 2 * h_min, h_steps)
    F_int = fem_int(d_sep - x_int) - fem_int(d_sep + x_int)
65     return (x_int, F_int)

```

Listing 2: Python code for repulsion force calculation.

## B Magnetic flux linkage calculation

```

1 # -*- coding: utf-8 -*-
from __future__ import division
3 from scipy.special import ellipk, ellipe, ellipkinc, ellipeinc
from sympy import elliptic_k, elliptic_pi
5 import matplotlib.pyplot as plt
import matplotlib.patches as patches
7 import numpy as np
from numba import jit
9
    tol = 1e-5
11
13 @jit
def cel(kc, p, c, s):
15     if kc == 0:
        return np.nan
17     errtol = 0.000001
    k = abs(kc)
19     pp = p
    cc = c
21     ss = s
    em = 1.0
23     if p > 0:
        pp = np.sqrt(p)
        ss = s / pp
25     else:
27         f = kc * kc
        q = 1.0 - f
29         g = 1.0 - pp
        f = f - pp
31         q = q * (ss - c * pp)

```

```

33     pp = np.sqrt(f / g)
34     cc = (c - ss) / g
35     ss = -q / (g * g * pp) + cc * pp
36     f = cc
37     cc = cc + ss / pp
38     g = k / pp
39     ss = 2 * (ss + f * g)
40     pp = g + pp
41     g = em
42     em = k + em
43     kk = k
44     # while np.abs(g-k) > g*errtol:
45     while abs(g - k) > g * errtol:
46         k = 2 * np.sqrt(kk)
47         kk = k * em
48         f = cc
49         cc = cc + ss / pp
50         g = kk / pp
51         ss = 2 * (ss + f * g)
52         pp = g + pp
53         g = em
54         em = k + em
55     return (np.pi / 2 * (ss + cc * em) / (em * (em + pp)))

56
57 @jit
58 def Heuman_Lambda(phi, m):
59     if phi == np.pi / 2:
60         return 1.0
61     if m == 1:
62         m = 1 - 1e-9
63     mdash = (1 - m)
64
65     K = ellipk(m)
66     E = ellipe(m)
67     incF = ellipkinc(phi, mdash)
68     incE = ellipeinc(phi, mdash)
69
70     HL = 2 / np.pi * (E * incF + K * incE - K * incF)
71     return HL
72
73
74 @jit
75 def nasa_axial(Br, a, b, r, z):
76     """
77     nasa_axial calculates the magnetic flux density of a cylindrical permanent
78     magnet as defined in [NASA].
79
80     Br = Residual Flux Density [T]
81     a = Coil radius [m]
82     b = magnet length / 2 [m]
83     r = radius from the z axis
84     z = z coordinate
85

```

[NASA] Callaghan, E.E. and Maslen, S.H., 1960. The magnetic field of  
a finite solenoid.

"""

if ((z == b) and (r == a)) or ((z == -b) and (r == a)):

    r = 1.0001 \* r

if r == 0:

    r = 1e-100

z1 = z + b

m1 = 4 \* a \* r / (z1 \* z1 + (a + r) \* (a + r))

z2 = z - b

m2 = 4 \* a \* r / (z2 \* z2 + (a + r) \* (a + r))

if (a - r) == 0:

    phi1 = np.pi / 2

    phi2 = np.pi / 2

    BZ = Br / 4 \* (z1 / np.pi \* np.sqrt(m1 / (a \* r)) \* ellipk(m1) -  
                    (z2 / np.pi \* np.sqrt(m2 / (a \* r)) \* ellipk(m2)))

else:

    phi1 = np.arctan(abs(z1 / (a - r)))

    phi2 = np.arctan(abs(z2 / (a - r)))

    if z1 == 0:

        BZ = - Br / 4 \* \

            (z2 / np.pi \* np.sqrt(m2 / (a \* r)) \* ellipk(m2) +

            (a - r) \* z2 / abs((a - r) \* z2) \* Heuman\_Lambda(phi2, m2))

    elif z2 == 0:

        BZ = Br / 4 \* \

            (z1 / np.pi \* np.sqrt(m1 / (a \* r)) \* ellipk(m1) +

            (a - r) \* z1 / abs((a - r) \* z1) \* Heuman\_Lambda(phi1, m1))

    else:

        BZ = Br / 4 \* \

            (z1 / np.pi \* np.sqrt(m1 / (a \* r)) \* ellipk(m1) +

            (a - r) \* z1 / abs((a - r) \* z1) \* Heuman\_Lambda(phi1, m1) -

            (z2 / np.pi \* np.sqrt(m2 / (a \* r)) \* ellipk(m2) +

            (a - r) \* z2 / abs((a - r) \* z2) \* Heuman\_Lambda(phi2, m2)))

return BZ

@jit

def nasa\_radial(Br, a, b, r, z):

    if ((z == b) and (r == a)) or ((z == -b) and (r == a)):

        r = 1.0001 \* r

    if r == 0:

        r = 1e-100

    # if z == b:

    # z = z \* 10001 / 10000

z1 = z + b

m1 = 4 \* a \* r / (z1 \* z1 + (a + r) \* (a + r))

```

141     z2 = z - b
142     m2 = 4 * a * r / (z2 * z2 + (a + r) * (a + r))
143
144     BZ = Br / np.pi * np.sqrt(a / r) * \
145         ((2 - m1) / (2 * np.sqrt(m1)) * ellipk(m1) - ellipse(m1) / np.sqrt(m1) -
146          ((2 - m2) / (2 * np.sqrt(m2)) * ellipk(m2) - ellipse(m2) / np.sqrt(m2))
147         )
148
149     return BZ
150
151 @jit
152 def Foelsch1_axial(Br, a, b, r, z):
153     """
154     Foelsch1_axial calculates the magnetic flux density of a cylindrical
155     permanent magnet as defined in [Foelsch].
156
157     Br = Residual Flux Density [T]
158     a = Coil radius [m]
159     b = magnet length / 2 [m]
160     r = radius from the z axis
161     z = z coordinate
162
163     [Foelsch]    Foelsch, K., 1936. Magnetfeld und Induktivitat einer
164                  zylindrischen Spule. Archiv fur Elektrotechnik,
165                  30(3), pp.139-157.
166     """
167
168     if a == r:
169         r = 1.0001 * r
170     z1 = z + b
171     z2 = z - b
172     Rr4 = 4 * a * r
173     Rrsquared = ((a + r) * (a + r))
174     n = Rr4 / Rrsquared
175
176     beta1 = Rrsquared / (Rrsquared + z1 * z1)
177     beta2 = Rrsquared / (Rrsquared + z2 * z2)
178     m1 = n * beta1
179     m2 = n * beta2
180
181     sqrt1n = np.sqrt(1 - n)
182
183     if r <= a:
184         A1 = (float(elliptic_k(m1)) + float(elliptic_pi(n, m1)) * sqrt1n) * np.
185         sqrt(1 - beta1)
186         A2 = (float(elliptic_k(m2)) + float(elliptic_pi(n, m2)) * sqrt1n) * np.
187         sqrt(1 - beta2)
188     else:
189         A1 = (float(elliptic_k(m1)) - float(elliptic_pi(n, m1)) * sqrt1n) * np.
190         sqrt(1 - beta1)
191         A2 = (float(elliptic_k(m2)) - float(elliptic_pi(n, m2)) * sqrt1n) * np.
192         sqrt(1 - beta2)

```

```

191     if (z >= -b) and (z <= b):
192         BZ = Br * (A2 + A1) / (2 * np.pi)
193     elif z < -b:
194         BZ = Br * (A2 - A1) / (2 * np.pi)
195     else:
196         BZ = Br * (A1 - A2) / (2 * np.pi)
197
198     return BZ
199
200 @jit
201 def Foelsch2_axial(Br, a, b, r, z):
202     """
203     Foelsch2_axial calculates the magnetic flux density of a cylindrical
204     permanent magnet as defined in [Foelsch].
205
206     Br = Residual Flux Density [T]
207     a = Coil radius [m]
208     b = magnet length / 2 [m]
209     r = radius from the z axis
210     z = z coordinate
211
212     [Foelsch]    Foelsch, K., 1936. Magnetfeld und Induktivitat einer
213                  zylindrischen Spule. Archiv fur Elektrotechnik,
214                  30(3), pp.139-157.
215     """
216
217     if ((z == b) and (r == a)) or ((z == -b) and (r == a)):
218         r = 1.0001 * r
219
220     z1 = z + b
221     z2 = z - b
222
223     n = 4 * a * r / (a + r) ** 2
224     beta1 = (a + r) ** 2 / ((a + r) ** 2 + z1 * z1)
225     beta2 = (a + r) ** 2 / ((a + r) ** 2 + z2 * z2)
226     m1 = n * beta1
227     m2 = n * beta2
228     K1 = ellipk(m1)
229     E1 = ellipe(m1)
230     K2 = ellipk(m2)
231     E2 = ellipe(m2)
232
233     if m1 == 1:
234         sin2phi = 0
235     else:
236         sin2phi = (1 - n) / (1 - m1)
237     phi1 = np.arcsin(np.sqrt(sin2phi))
238     sin2b1 = 1 - m1
239     Finc = ellipkinc(phi1, sin2b1)
240     if Finc == np.inf:
241         Finc = 10e20
242     Einc = ellipeinc(phi1, sin2b1)
243
244     A1 = np.pi / 2 + K1 * np.sqrt(1 - beta1) * (1 + np.sqrt(1 - n)) + Finc * (K1
    - E1) - K1 * Einc

```

```

243 B1 = 2 * K1 * np.sqrt(1 - beta1) - A1
245
246 if m2 == 1:
247     sin2phi = 0
248 else:
249     sin2phi = (1 - n) / (1 - m2)
250 phi2 = np.arcsin(np.sqrt(sin2phi))
251 sin2b2 = 1 - m2
252 Einc = ellipeinc(phi2, sin2b2)
253 Finc = ellipkinc(phi2, sin2b2)
254 if Finc == np.inf:
255     Finc = 10e20
256 A2 = np.pi / 2 + K2 * np.sqrt(1 - beta2) * (1 + np.sqrt(1 - n)) + Finc * (K2
257 - E2) - K2 * Einc
258 B2 = 2 * K2 * np.sqrt(1 - beta2) - A2
259
260 if r <= a:
261     if (z >= -b) and (z <= b):
262         BZ = Br * (A2 + A1) / (2 * np.pi)
263     elif z < -b:
264         BZ = Br * (A2 - A1) / (2 * np.pi)
265     else:
266         BZ = Br * (A1 - A2) / (2 * np.pi)
267 #         BZ = Br * (A2 - A1) / (2 * np.pi)
268 else:
269     if (z >= -b) and (z <= b):
270         BZ = Br * (B2 + B1) / (2 * np.pi)
271     elif z < -b:
272         BZ = Br * (B2 - B1) / (2 * np.pi)
273     else:
274         BZ = Br * (B1 - B2) / (2 * np.pi)
275
276 return BZ
277
278 @jit
279 def Derby_axial(Br, a, b, r, z):
280     """
281     Derby_axial calculates the magnetic flux density of a cylindrical permanent
282     magnet as defined in [DERBY].
283
284     Br = Residual Flux Density [T]
285     a = Coil radius [m]
286     b = magnet length / 2 [m]
287     r = radius from the z axis
288     z = z coordinate
289
290     [DERBY] Derby, N. and Olbert, S., 2010. Cylindrical magnets and ideal
291     solenoids. American Journal of Physics, 78(3), pp.229-235.
292     """
293
294     if ((abs(z - b) < tol) and (abs(r - a) < tol)) or \
295         ((abs(z + b) < tol) and (abs(r - a) < tol)):
296         r = 1.0001 * r

```

```

297     z1 = z + b
299     beta1 = z1 / np.sqrt(z1 * z1 + (r + a) * (r + a))
301     k1 = np.sqrt((z1 * z1 + (a - r) * (a - r)) / (z1 * z1 + (a + r) * (a + r)))
303
305     z2 = z - b
307     beta2 = z2 / np.sqrt(z2 * z2 + (r + a) * (r + a))
309     k2 = np.sqrt((z2 * z2 + (a - r) * (a - r)) / (z2 * z2 + (a + r) * (a + r)))
311
313     gamma = (a - r) / (a + r)
315     Bz = Br / np.pi * a / (a + r) * (beta1 * cel(k1, gamma * gamma, 1, gamma) -
317                                     beta2 * cel(k2, gamma * gamma, 1, gamma))
319
321     return Bz
323
325 @jit
327 def flux_linkage_Foelsch1_axial(Br, h_mag, r_mag, h_coil, r_i, r_o, k_co, d_co,
329 d, parts):
331     Nz_float = 2 * h_coil / (d_co * np.sqrt(np.pi / k_co))
333     Nr_float = 2 * (r_o - r_i) / (d_co * np.sqrt(np.pi / k_co))
335     Nr = int(round(Nr_float))
337     Nz = int(round(Nz_float))
339     dN = Nz_float / Nz * Nr_float / Nr
341
343     FL = 0.0
345     dz = h_coil / Nz
347     z = d - h_coil / 2 + dz / 2
349     for j in xrange(Nz):
351         dFL = 0.0
353
355         dr = r_mag / parts
357         r = dr / 2
359         for i in xrange(parts):
361             Bz = Foelsch1_axial(Br, r_mag, h_mag / 2, r, z)
363             dFL += Bz * np.pi * 2 * r * dr
365             r += dr
367
369         dr = (r_i - r_mag) / parts
371         r = r_mag + dr / 2
373         for i in xrange(parts):
375             Bz = Foelsch1_axial(Br, r_mag, h_mag / 2, r, z)
377             dFL += Bz * np.pi * 2 * r * dr
379             r += dr
381
383         dr = (r_o - r_i) / Nr
385         r = r_i + dr / 2
387         for i in xrange(Nr):
389             Bz = Foelsch1_axial(Br, r_mag, h_mag / 2, r, z)
391             dFL += Bz * np.pi * 2 * r * dr
393         FL += dN * dFL
395         r += dr
397     z += dz
399     return FL

```



349

351 @jit

```
def flux_linkage_Foelsch2_axial(Br, h_mag, r_mag, h_coil, r_i, r_o, k_co, d_co,
d, parts):
```

```
    Nz_float = 2 * h_coil / (d_co * np.sqrt(np.pi / k_co))
```

```
    Nr_float = 2 * (r_o - r_i) / (d_co * np.sqrt(np.pi / k_co))
```

```
    Nr = int(round(Nr_float))
```

```
    Nz = int(round(Nz_float))
```

```
    dN = Nz_float / Nz * Nr_float / Nr
```

```
    FL = 0.0
```

```
    dz = h_coil / Nz
```

```
    z = d - h_coil / 2 + dz / 2
```

```
    for j in xrange(Nz):
```

```
        dFL = 0.0
```

```
        dr = r_mag / parts
```

```
        r = dr / 2
```

```
        for i in xrange(parts):
```

```
            Bz = Foelsch2_axial(Br, r_mag, h_mag / 2, r, z)
```

```
            dFL += Bz * np.pi * 2 * r * dr
```

```
            r += dr
```

```
        dr = (r_i - r_mag) / parts
```

```
        r = r_mag + dr / 2
```

```
        for i in xrange(parts):
```

```
            Bz = Foelsch2_axial(Br, r_mag, h_mag / 2, r, z)
```

```
            dFL += Bz * np.pi * 2 * r * dr
```

```
            r += dr
```

```
        dr = (r_o - r_i) / Nr
```

```
        r = r_i + dr / 2
```

```
        for i in xrange(Nr):
```

```
            Bz = Foelsch2_axial(Br, r_mag, h_mag / 2, r, z)
```

```
            dFL += Bz * np.pi * 2 * r * dr
```

```
            FL += dN * dFL
```

```
            r += dr
```

```
        z += dz
```

```
    return FL
```

389 @jit

```
def flux_linkage_nasa_axial(Br, h_mag, r_mag, h_coil, r_i, r_o, k_co, d_co, d,
parts):
```

```
    Nz_float = 2 * h_coil / (d_co * np.sqrt(np.pi / k_co))
```

```
    Nr_float = 2 * (r_o - r_i) / (d_co * np.sqrt(np.pi / k_co))
```

```
    Nr = int(round(Nr_float))
```

```
    Nz = int(round(Nz_float))
```

```
    dN = Nz_float / Nz * Nr_float / Nr
```

```
    FL = 0.0
```

```
    dz = h_coil / Nz
```

```
    z = d - h_coil / 2 + dz / 2
```

```

401     for j in xrange(Nz):
402         dFL = 0.0
403
404         dr = r_mag / parts
405         r = dr / 2
406         for i in xrange(parts):
407             Bz = nasa_axial(Br, r_mag, h_mag / 2, r, z)
408             dFL += Bz * np.pi * 2 * r * dr
409             r += dr
410
411         dr = (r_i - r_mag) / parts
412         r = r_mag + dr / 2
413         for i in xrange(parts):
414             Bz = nasa_axial(Br, r_mag, h_mag / 2, r, z)
415             dFL += Bz * np.pi * 2 * r * dr
416             r += dr
417
418         dr = (r_o - r_i) / Nr
419         r = r_i + dr / 2
420         for i in xrange(Nr):
421             Bz = nasa_axial(Br, r_mag, h_mag / 2, r, z)
422             dFL += Bz * np.pi * 2 * r * dr
423             FL += dN * dFL
424             r += dr
425         z += dz
426     return FL
427
428 @jit
429 def flux_linkage_Derby_axial(Br, h_mag, r_mag, h_coil, r_i, r_o, k_co, d_co, d,
430 parts):
431     Nz_float = 2 * h_coil / (d_co * np.sqrt(np.pi / k_co))
432     Nr_float = 2 * (r_o - r_i) / (d_co * np.sqrt(np.pi / k_co))
433     Nr = int(round(Nr_float))
434     if Nr == 0:
435         Nr = 1
436     Nz = int(round(Nz_float))
437     if Nz == 0:
438         Nz = 1
439     dN = Nz_float / Nz * Nr_float / Nr
440
441     FL = 0.0
442     dz = h_coil / Nz
443     z = d - h_coil / 2 + dz / 2
444     for j in xrange(Nz):
445         dFL = 0.0
446
447         dr = r_mag / parts
448         r = dr / 2
449         for i in xrange(parts):
450             Bz = Derby_axial(Br, r_mag, h_mag / 2, r, z)
451             dFL += Bz * np.pi * 2 * r * dr
452             r += dr
453

```

```

455     dr = (r_i - r_mag) / parts
456     r = r_mag + dr / 2
457     for i in xrange(parts):
458         Bz = Derby_axial(Br, r_mag, h_mag / 2, r, z)
459         dFL += Bz * np.pi * 2 * r * dr
460         r += dr
461
462     dr = (r_o - r_i) / Nr
463     r = r_i + dr / 2
464     for i in xrange(Nr):
465         Bz = Derby_axial(Br, r_mag, h_mag / 2, r, z)
466         dFL += Bz * np.pi * 2 * r * dr
467         FL += dN * dFL
468         r += dr
469     z += dz
470     return FL
471
472 def calc_flux_gradient(m_Br, h_mag, r_mag, h_coil, r_i, r_o, N, d_co, d):
473     parts = 30
474
475     k_co = np.pi * d_co * d_co * N / (4 * h_coil * (r_o - r_i))
476
477     Nz = int(round(2.0 * h_coil / (d_co * np.sqrt(np.pi / k_co))))
478     # Nz = 100
479
480     step = h_coil / Nz
481
482     y1 = flux_linkage_Derby_axial(m_Br, h_mag, r_mag, h_coil, r_i, r_o, k_co,
483     d_co, d - step, parts) # noqa
484     y2 = flux_linkage_Derby_axial(m_Br, h_mag, r_mag, h_coil, r_i, r_o, k_co,
485     d_co, d + step, parts) # noqa
486     k = (y2 - y1) / (2 * step)
487
488     return k
489
490 @jit
491 def calc_power(m_Br, h_mag, r_mag, h_coil, r_i, r_o, N, d_co, t0, a, f):
492     parts = 30
493
494     k_co = np.pi * d_co * d_co * N / (4 * h_coil * (r_o - r_i))
495
496     Nz = int(round(2.0 * h_coil / (d_co * np.sqrt(np.pi / k_co))))
497     step = h_coil / Nz
498
499     d = -(h_mag + h_coil) / 2 + t0 - step
500     y1 = flux_linkage_Derby_axial(m_Br, h_mag, r_mag, h_coil, r_i, r_o, k_co,
501     d_co, d, parts)
502     d = -(h_mag + h_coil) / 2 + t0 + step
503     y2 = flux_linkage_Derby_axial(m_Br, h_mag, r_mag, h_coil, r_i, r_o, k_co,
504     d_co, d, parts)
505     k = (y2 - y1) / (2 * step)

```

```

505     resistivity = 1.709e-8 / (d_co * d_co * np.pi / 4)
R_coil = N * np.pi * (r_o + r_i) * resistivity
dm = 0.1
507 R_load = R_coil + k * k / dm

509 de = k * k / (R_coil + R_load)
density = 7600.0
511 m = h_mag * np.pi * r_mag * r_mag * density
#     print "de = %.2f, m = %.2f g" % (de, m*1000)
513
omega = 2 * np.pi * f
515 Z = m * a / ((de + dm) * omega)
speed = Z * omega

517
V = k * speed
519 V_load = V * R_load / (R_coil + R_load)
P = V_load * V_load / R_load
521
return P
523

525 @jit
def calc_power_all(m_Br, h_mag, r_mag, h_coil, r_i, r_o, N, d_co, t0, a, f):
527     parts = 30

529     k_co = np.pi * d_co * d_co * N / (4 * h_coil * (r_o - r_i))

531     Nz = int(round(2.0 * h_coil / (d_co * np.sqrt(np.pi / k_co))))
step = h_coil / Nz
533
d = -(h_mag + h_coil) / 2 + t0 - step
535 y1 = flux_linkage_Derby_axial(m_Br, h_mag, r_mag, h_coil, r_i, r_o, k_co,
d_co, d, parts)
d = -(h_mag + h_coil) / 2 + t0 + step
537 y2 = flux_linkage_Derby_axial(m_Br, h_mag, r_mag, h_coil, r_i, r_o, k_co,
d_co, d, parts)
k = (y2 - y1) / (2 * step)
539
#     print "Nz = %d, Nr = %d, N = %d" % (round(Nz), round(Nr), round(N))
541     resistivity = 1.709e-8 / (d_co * d_co * np.pi / 4)
R_coil = N * np.pi * (r_o + r_i) * resistivity
543 dm = 0.1
R_load = R_coil + k * k / dm

545
de = k * k / (R_coil + R_load)
547 density = 7600.0
m = h_mag * np.pi * r_mag * r_mag * density
549 #     print "de = %.2f, m = %.2f g" % (de, m*1000)

omega = 2 * np.pi * f
551 Z = m * a / ((de + dm) * omega)
553 speed = Z * omega

555 V = k * speed

```

```

557     V_load = V * R_load / (R_coil + R_load)
558     P = V_load * V_load / R_load
559
560     return (Z, R_coil, R_load, k, V_load, P)
561
562 @jit
563 def calc_power_all_two_coils(m_Br, h_mag, r_mag, h_coil, r_i, r_o, N, d_co, t0,
564     a, f):
565     parts = 30
566
567     k_co = np.pi * d_co * d_co * N / (4 * h_coil * (r_o - r_i))
568
569     Nz = int(round(2.0 * h_coil / (d_co * np.sqrt(np.pi / k_co))))
570     step = h_coil / Nz
571
572     d = -(h_mag + h_coil) / 2 + t0 - step
573     y1 = flux_linkage_Derby_axial(m_Br, h_mag, r_mag, h_coil, r_i, r_o, k_co,
574     d_co, d, parts)
575     d = -(h_mag + h_coil) / 2 + t0 + step
576     y2 = flux_linkage_Derby_axial(m_Br, h_mag, r_mag, h_coil, r_i, r_o, k_co,
577     d_co, d, parts)
578     k = (y2 - y1) / (step) # k is now doubled !!!!!!!
579
580     resistivity = 1.709e-8 / (d_co * d_co * np.pi / 4)
581     R_coil = 2 * N * np.pi * (r_o + r_i) * resistivity # Rcoil is x2
582     dm = 0.1
583     R_load = R_coil + k * k / dm
584
585     de = k * k / (R_coil + R_load)
586     density = 7600.0
587     m = h_mag * np.pi * r_mag * r_mag * density
588     # print "de = %.2f, m = %.2f g" % (de, m*1000)
589
590     omega = 2 * np.pi * f
591     Z = m * a / ((de + dm) * omega)
592     speed = Z * omega
593
594     V = k * speed
595     V_load = V * R_load / (R_coil + R_load)
596     P = V_load * V_load / R_load
597
598     return (Z, R_coil, R_load, k, V_load, P)
599
600 @jit
601 def calc_power_two_coils(m_Br, h_mag, r_mag, h_coil, r_i, r_o, N, d_co, t0, a, f
602 ):
603     parts = 30
604
605     k_co = np.pi * d_co * d_co * N / (4 * h_coil * (r_o - r_i))
606
607     Nz = int(round(2.0 * h_coil / (d_co * np.sqrt(np.pi / k_co))))
608     step = h_coil / Nz

```

```

607     d = -(h_mag + h_coil) / 2 + t0 - step
        y1 = flux_linkage_Derby_axial(m_Br, h_mag, r_mag, h_coil, r_i, r_o, k_co,
609     d_co, d, parts)
        d = -(h_mag + h_coil) / 2 + t0 + step
        y2 = flux_linkage_Derby_axial(m_Br, h_mag, r_mag, h_coil, r_i, r_o, k_co,
        d_co, d, parts)
611     k = (y2 - y1) / (step) # k is now doubled !!!!!!!

613     resistivity = 1.709e-8 / (d_co * d_co * np.pi / 4)
        R_coil = 2 * N * np.pi * (r_o + r_i) * resistivity # R_coil is x2
615     dm = 0.1
        R_load = R_coil + k * k / dm

617
        de = k * k / (R_coil + R_load)
619     density = 7600.0
        m = h_mag * np.pi * r_mag * r_mag * density
621 #     print "de = %.2f, m = %.2f g" % (de, m*1000)

623     omega = 2 * np.pi * f
        Z = m * a / ((de + dm) * omega)
625     speed = Z * omega

627     V = k * speed
        V_load = V * R_load / (R_coil + R_load)
629     P = V_load * V_load / R_load

631     return P

```

Listing 3: Python code for magnetic flux linkage calculation.